Extension - Upgrading Methane Using Ultra-Fast Thermal Swing Adsorption

Final Report
January 2009

by
Anna Lee Tonkovich

January 2009

DE-FC26-03NT41905

Velocys
7950 Corporate Boulevard
Plain City, Ohio 43064

Subcontractor
Joseph D'Amico
6422 Oak Park Court
Linthicum, MD 21090

Abstract

The need for cost effective technologies for upgrading coal mine methane to pipeline quality natural gas is becoming ever greater. The current work presents and investigates a new approach to reduce the impact of the most costly step in the conventional technology, nitrogen rejection. The proposed approach is based on the Velocys microchannel platform, which is being developed to commercialize compact and cost efficient chemical processing technology. For this separation, ultra fast thermal swing sorption is enabled by the very high rates of heat and mass transfer inherent in microchannel processing.

In a first phase of the project solid adsorbents were explored. Feasibility of ultrafast thermal swing was demonstrated but the available adsorbents had insufficient differential methane capacity to achieve the required commercial economics.

In a second phase, ionic liquids were adopted as absorbents of choice, and experimental work and economic analyses, performed to gauge their potential, showed promise for this novel alternative. Final conclusions suggest that a combination of a required cost target for ionic liquids or a methane capacity increase or a combination of both is required for commercialization.

Table of Contents

List of Graphical Material, Phase 1

List of Graphical Material, Phase 2

Figure 15. Pressure and concentration profiles for various equilibration scenarios involving a collection vessel pre-pressurized to 100 psig with nitrogen and inlet flows of 10 sccm of pure methane gas and 1 ccm of ionic liquid. Henry's constants are assumed to be 20000 and 240 bar/mol fraction for nitrogen and methane, respectively. a) Liquid and vapor flows with no absorption in the contacting device or collection vessel. b) Liquid and vapor flows with instantaneous ideal equilibration in the collection vessel. c) Liquid and vapor flows with ideal absorption in the contacting device and no re-equilibration in the collection vessel. Figures a, b, and c correspond to Runs 1, 2, and 3 in Table 3, respectively.

Figure 16. Schematic of the CHEMCAD process cycle used in a designed experiment to discern the impact of operating parameters on separation costs.

Figure 17. Cost projections made by the CHEMCAD model as a function of the operating parameter settings. The cost per thousand standard cubic feed of pipeline grade natural gas produced assumes $1.50 per thousand standard cubic feet of feed gas, a six to one mole ratio of ionic liquid required per mole of feed, $40 per liter of ionic liquid, and 0.5 million dollars capital cost for the microprocess technology component.

Figure 18. Schematic of the CHEMCAD process cycle used to discern the impact of methane solubility on ionic liquid utilization. Although included in the simulation, the sweep gas stream was assumed to be empty.

Figures 19 a and b. CH4 recovery and product stream purity as a function of ionic liquid utilization for two representative solubility cases. Both cases assumed a 240 bar/mol fraction HCH4 in the desorption unit. Case 1 assumed a 24 bar/mol fraction HCH4 at the absorption unit; Case 2 assumed a 120 bar/mol fraction value. Detailed results are presented in Table 6.

Figure 20. Estimates of yearly potential income from the sale of purified product stream compared against the one-time procurement costs of the ionic liquids considered in the current simulations.

Figure 21. Published temperature dependent methane solubility values for some common ionic liquid alternatives. [hmim][Tf2N] data were taken from Kumelan et al. (2007a), [bmim][PF6] data from Jacquemin et al. (2006a), [bmim][BF4] data from Jacquemin et al. (2006b), [bmim][CH3SO4] data from Kumelan et al. (2007b). Values at 10°C were extrapolated from expressions included in the sources.

Figure 22 a. CH4 recovery and product stream purity as a function of ionic liquid utilization for a representative case assuming the reported methane Henry's constant of [hmim][Tf2N]: 208 bar/mol fraction in the desorption unit and 129 bar/mol fraction at the absorption unit.
b. Estimates of yearly potential income from the sale of purified product stream compared against the one-time procurement costs of the ionic liquids considered in the current simulation.

Table 1. Methane solubility measurements. Ionic liquid batch relates to the time of purchase; this was noted to ensure potential manufacturing differences would not be overlooked.

Table 2. Continuous flow absorption test results.

Table 3. Simulated run conditions for semi-batch absorption testing. All cases assume a 1 ccm ionic liquid flow rate and 20°C operation. Simulation case 1 assumes no absorption. Simulation case 2 assumes instantaneous vapor liquid equilibration in the collection vessel. Simulation case 3 assumes vapor liquid equilibrium at the exit of the contacting unit with no further equilibration in the collection vessel. Ionic liquid density and molecular weight are assumed constant and equal to 612.29 g/mol and 1.56 g/cc, respectively. Figure 16 summarizes results for Runs 1, 2, and 3.

Table 4. Preliminary semi-batch test results and comparative estimates. Feeds were let flow into the collection vessel for 34 min. In all cases, the vapor feed was pure methane and the pre-pressurized collection vessel was filled with pure nitrogen.

Table 5. Energy required as a function of approach temperature to capture 63% of a mixture comprising 80% nitrogen and flowing at 2 million standard cubic feet per day using the [bmim][PF6] ionic liquid and based on highly effective microchannel recuperative heat exchangers.

Table 6. CHEMCAD DOE parameter settings.

Table 7. Ionic liquid properties assumed in simulation Cases 1 and 2.

Table 8. Key flow rates, composition and results of CHEMCAD simulated Cases 1 and 2.

Table 9. Published temperature dependent methane solubility values for some common ionic liquid alternatives. [hmim][Tf2N] data were taken from Kumelan et al. (2007a), [bmim][PF6] data from Jacquemin et al. (2006a), [bmim][BF4] data from Jacquemin et al. (2006b), [bmim][CH3SO4] data from Kumelan et al. (2007b). Values at 10°C were extrapolated from expressions included in the sources.

Introduction

The objective of the project was to identify a technical solution for upgrading subquality methane to pipeline quality using thermal swing adsorption. Many solid adsorbents were evaluated but none was found to obtain suitable differential capacity as required for commercial economics.

The objective of the project extension over 24 months is to further evaluate the microchannel technology under real world processing conditions with a switch from adsorption to absorption. Five main objectives were proposed:

- Identify one or more commercial absorbents that can meet the purity and recovery requirements for pipeline specifications
- Demonstrate that the absorbents can operate with real feed mixtures of coal mine methane streams
- Demonstrate that the bench-scale absorber meets the purity, recovery, and durability requirements
- Confirm manufacturability of absorber units and identify critical development needs
- Show that the technology meets industry's economic targets for capital and operating costs

The scope of the project has encompassed the use of a liquid absorbent to replace solid adsorbents. The use of liquids will ease the scaleup challenges of the technology. Methane will preferentially sorb into the liquid at one temperature and then travel to a second higher temperature stage to desorb.

The status of the revised tasks is listed below:

- Task 1: Evaluate improved and optimized sorbents – *complete*
  - Selected a literature liquid absorbent for an initial proof of principle demonstration in the summer of FY07.
  - Identified an external consultant with expertise in liquid sorbents for chemical separations.
- Task 2: Prepare the experimental test stand for a thermal swing absorption feasibility experiment – *complete*
- Task 3: Demonstrate the bench-scale absorber with a real feed mixture and improved adsorbent – *complete*
- Task 4: Develop preliminary manufacturing plan for full-scale microchannel units and identify critical development needs – *complete*
- Task 5: Update system design and cost based on thermal integration with coal-mine methane upgrading plants – *complete*
- Task 6: Commercialize Technology – *pending breakthrough in ionic liquid cost or capacity*
- Task 7: Project Management – *complete*

Executive Summary

The purpose of this project is to develop a cost effective technology for upgrading coal mine methane to pipeline quality natural gas. Nitrogen rejection is the most costly step with conventional technology and emerging competitive technology. Significant cost reductions to this step will allow for the cost effective capture and utilization of this otherwise potent greenhouse gas. The proposed approach is based on the microchannel technology platform that Velocys is developing to commercialize compact and cost efficient chemical processing technology. For this application, ultra fast thermal swing absorption is enabled by the very high rates of heat transfer enabled by microchannels.

Natural gas upgrading systems have six main unit operations: feed compressor, dehydration unit, nitrogen rejection unit, deoxygenator, carbon dioxide scrubber, and a sales compressor. The NRU is the focus of the development program. The Velocys NRU system targets producing methane with greater than 96% purity and at least 90% recovery for final commercial operation. A preliminary cost analysis of the methane upgrading system, including the Velocys NRU, suggests that costs below $2.00 per million (MM) BTU methane may be achieved. The cost for a conventional methane upgrading system is well above $2.30 per MM BTU, as benchmarked in an EPA study.

Initial performance results for the Velocys TSA technology were promising. Subsequent work to refine the analysis with the selected carbon adsorbents revealed that achieving the purity targets would be challenging with a single stage system. An extensive search was done to find alternate sorbents for methane capture. A very promising class of absorbents were identified and proof of principle demonstrations were begun.

Since the beginning of 2007, the test system was modified to accommodate a liquid sorbent rather than a solid counterpart. Specifically, ionic liquids were identified as materials with affinity for methane and very little, if any, affinity for nitrogen. Samples of ionic liquids with reported or likely affinity for methane were ordered and their absorption performance was evaluated adopting specifically designed batch and microchannel flow through experimental systems.

Economic analyses and experimental testing showed promise for the implementation of tailored ionic liquids for industrial separations. Preliminary experimental flow tests demonstrated potential for approaching maximum absorption capacity adopting microchannel devices that allow enhanced interfacial contacting. Economic analyses evidenced that ionic liquid procurement is the most significant contributor to process cost and that, adopting a readily available, off-the-shelf ionic liquid and a single pass continuous flow process, it is possible to capture 25% of the methane from a 2,000,000 SCFD low quality, 70 mol% CH4 / 30 mol% N2, natural gas stream to obtain a 96% pure methane product stream and recover the one-time ionic liquid procurement cost in 12.4 months. In addition, for only a 72% reduction in the absorption-side Henry's constant for methane relative to this off-the shelf ionic liquid, further analysis revealed potential for a 90% methane recovery from the flue gas stream at a 96.6% purity level

for a 4.6 month break even point, assuming an ionic liquid cost of $10/L, and a 23 month break even point for an ionic liquid cost of $50/L.

Given the ability to tailor ionic liquid properties and modify absorption capacity and specificity of these materials, there is great promise for finding an ionic liquid suited to the current process, making this mode of separation an economically viable alternative for methane recovery from process flue streams.

Phase 1. Technical Results

Task 1.1. Adsorbent Ranking

Objective

The goal of the adsorbent ranking task was to identify at least one adsorbent that is sufficient for demonstrating the ultimate performance and cost advantage of an MPT-based TSA process for upgrading coal mine gob gas to pipeline quality. In particular, the objective was to identify adsorbents for the most challenging separation, nitrogen from methane. Identification of an adsorbent that preferentially adsorbs nitrogen over methane was sought, although preferential adsorption of methane over nitrogen also could be acceptable. The final goal of this task was to identify the adsorbent that could most easily (rather than perfectly or optimally) be used to move forward.

Adsorbent Criteria

Successful adsorbents for deployment in an MPT-based TSA process must possess the following attributes:

- High preferential capacity for either methane or nitrogen
- High differential capacity for either methane or nitrogen over a modest temperature range (5 C to 40 C expected, to be confirmed in Task 2.1)
- High attrition resistance during modest thermal swings
- Stability to constituents found in gob gas and corresponding cyclic regenerability as required, e.g., low levels of water must be reversibly removed periodically to maintain a sufficient working capacity.
- Reasonable cost.

The literature primarily contained information pertaining to preferential and differential capacity of either methane or nitrogen in single feed experiments as a function of temperature. There were fewer references citing results with mixed feed operation. This criterion is deemed the most important to identify an adsorbent candidate for a successful demonstration of MPT-based TSA processing for cost-effective methane upgrading.

Very little information was found regarding adsorbent stability to thermal swings because the vast majority of adsorbents are commercially used in pressure swing absorption (PSA) not TSA application. There was little information on stability to other gob gas constituents (O_2, CO_2, and H_2O). For many adsorbents, including the carbon family, carbon dioxide (CO_2) was more strongly adsorbed than methane. For most adsorbents, water is very strongly adsorbed – but reversibly so, when regenerated at temperatures of a few hundred degrees Celsius. No exotic adsorbents were identified as potential candidates, and thus reasonable costs are expected.

Preferential Methane Adsorption

The vast majority of cited literature describes adsorbents with a preferential affinity for methane over nitrogen. Calculations and reasonable technical assumptions were made as necessary to create a standardized comparison basis for capacity (mg adsorbate per gm adsorbent).

Table 1 ranks journal literature for adsorbents based on methane capacity at low pressure (around 1 atm). Note that all carbon adsorbents are highlighted in blue, the zeolites in orange, and the remaining adsorbents in contrasting colors. These adsorbents at low pressure have the lowest capacity, as expected, and represent a system configuration where minimal feed compression is required for an ultimate system. These adsorbents also reflect options for capturing methane from coal mine ventilation gas. Adsorbent capacity ranges from 10 to 20 mg/gm of methane at low pressure.

Table 2 ranks journal literature for adsorbents based on methane capacity at modest pressure (around 100 psig). These adsorbent options have higher capacity and represent a system that would require modest compression of the feed prior to the TSA process. The resulting feed would then be subsequently compressed to pipeline conditions (around 500 psig). Adsorbent capacity ranges from 50 to 80 mg/gm near 100 psig.

Table 3 ranks journal literature for adsorbents based on methane capacity at higher pressure (around 300 psig). These adsorbent options have the highest capacity, but would also require more feed compression prior to the TSA separation process. Adsorbent capacity for methane near 300 psig has been reported as high as 150 mg/gm.

Table 4 ranks patent literature for adsorbents based on either nitrogen or methane capacity. The primary adsorbent for preferential methane adsorption is carbon. The primary adsorbent for preferential nitrogen adsorption is a zeolite.

The selection of the operating pressure can be made based on performance (purity, recovery rate, and reliability) and cost.

Adsorbent name	Reference	CH4 capacity (mg/gm)	N2 capacity (mg/gm)	T in (C)	P (atm)
Activated carbon (G2X7/12 from Takeda Industries)	M24	27	12	0	1
Activated carbon sheet (carbonized foam)	M42	25			1
Anderson AX-21 (activated carbon)	M27	24	14	25	1
Activated carbon (Mega Carbon Ax-21)	M18	20		25	1
Activated carbon (G2X7/12 from Takeda Industries)	M24	19	10	25	1
Activated carbon	M9	16		26	1
Calgon BPL (carbon)	M27	16	6	25	1
Activated carbon (A35/4)	M43	16		20	1
NaX zeolite	M2	15		0	1
Activated carbon (Calgon Carbon BPL)	M18	15		25	1
H-ZSM-5-30	M35	11	7	40	1
AX-21 (activated carbon)	M8	10		23	1
BPL (activated carbon)	M8	10		23	1
CVD modified Na-A zeolite	M13	10		30	1
5A zeolite	M30	10	10	23	1
K04 (activated carbon)	M6	8		25	1
Zeolite (5A)	M9	8		25	1
Pyrolized polyvinylidene chloride (carbon)	M27	8	6	25	1
Pyrolized furfuraldehyde (carbon)	M27	8	6	25	1
AlPO4-11	M1	6	1.7	23	1
AlPO4-17	M1	5.2	3.5	40	1
NaY zeolite	M2	5		25	1
Aluminum pillared clay	M7	4.8		0	1
AlPO4-11	M1	4.6	1.1	40	1
AlPO4-18	M1	2.7	1.7	40	1
MCM-41	M34	2		30	1
Fe-substituted kaolinite	M10	1.4	1.8	25	1
Vulcan carbon	M41	0.5	0.25	20	1

Table 1. Adsorbents for methane and nitrogen at low pressure – open literature

Adsorbent name	Reference	CH4 capacity (mg/gm)	N2 capacity (mg/gm)	T in (C)	P (atm)
AX-21 (activated carbon)	M39	85	69	25	100
Activated carbon	M36	80	50	25	100
Activated carbon (Mega Carbon Ax-21)	M18	70		25	100
Anderson AX-21	M27	70	60	25	100
Pyrolized polyvinylidene chloride (carbon)	M27	65	55	25	100
AX-21 (activated carbon)	M8	60		23	100
NaX zeolite	M2	50		25	100
Calgon BPL (activated carbon)	M27	50	40	25	100
Activated carbon (A35/4)	M43	50		20	100
Activated carbon	M9	48		26	100
K04 (activated carbon)	M6	40		25	100
BPL (activated carbon)	M8	40		23	100
Activated carbon (Calgon Carbon BPL)	M18	40		25	100
Activated carbon	M22	40	34	45	120
5A zeolite	M30	35	40	23	90
zeolite (5A)	M9	32		25	100
NaY zeolite	M2	30		25	100
Pyrolized furfuraldehyde	M27	30	28	25	100
Carbon molecular sieve 5A (Takeda)	M47	30	28	20	100
13X Molecular Sieve	M21	25		35	100
AS Activated Carbon	M21	25		35	100
MCM-41	M34	12		30	100
Vulcan carbon	M39	2	1	25	100

Table 2. Adsorbents for methane and nitrogen at modest pressure (~ 100 psig) – open literature

Adsorbent name	Reference	CH4 capacity (mg/gm)	N2 capacity (mg/gm)	T in (C)	P (atm)
Activated carbon (Mega Carbon Ax-21)	M18	150		25	300
AX-21 (activated carbon)	M8	140		23	300
Anderson AX-21	M27	140	115	25	300
Pyrolized polyvinylidene chloride	M27	90	100	25	300
AS Activated Carbon	M21	70		35	300
Calgon BPL (activated carbon)	M27	70	70	25	300
Activated carbon (Calgon Carbon BPL)	M18	65		25	300
NaX zeolite	M2	60		25	300
BPL (activated carbon)	M8	60		23	300
NaY zeolite	M2	55		25	300
13X Molecular Sieve	M21	50		35	300
Pyrolized furfuraldehyde	M27	40	50	25	300
MCM-41	M34	24		30	300

Table 3. Adsorbents for methane and nitrogen at high pressure (300 psig) – open literature

Adsorbent name	Reference	CH4 capacity (mg/gm)	N2 capacity (mg/gm)	T in (C)	P (atm)
Li exchanged zeolites	M52		34	23	1
Zeolite-2	M53		30	20	1
Engelhard Ba-ETS-4 (at 30 seconds)	M70	2	11	25	1
Engelhard Ba-ETS-4 (at 10 minutes)	M70	7	11	25	1
Activated carbon (bituminous and subbituminous coal)	M54	8		25	1
Engelhard CTS-1 or Ba-ETS4 (density estimated at 0.5g/cc)	M63	4	10	27	27
Nusorb-A14	M65	178		25	34
Westvaco SN20-A1	M65	196		25	34
Microporous carbon	M66	13		10	1

Table 4. Adsorbents for methane and nitrogen separation – patent literature

Preferential Nitrogen Adsorption

One candidate emerged from the literature review that demonstrated preferential nitrogen adsorption over methane. The Molecular Gate™ technology from Engelhard Corporation is based on specially synthesized barium exchanged titano-silicate molecular sieve that create a pore opening of roughly 3.7 angstroms. This pore opening allows nitrogen (molecular diameter of 3.6 angstroms) to enter and adsorb while excluding methane (molecular diameter of 3.8 angstroms). For this adsorbent, significant co-adsorption of carbon dioxide (molecular diameter of 3.4 angstroms) is also reported. Only one reference (M70, patent 5,989,316) presented capacity data without requiring additional assumptions – roughly 10 mg/gm of nitrogen versus 2 mg/gm of methane at 25 C and 1 atm is reported.

Competitive Adsorption in Mixtures

Much of the reported data were collected as single-component isotherms. Several references discussed multi-component behavior based on fractional mixtures of methane and nitrogen. For all classes of adsorbents (carbons, reference M22; zeolites, reference M30; aluminophosphates, reference M1; and H-ZSM-5, reference M35), the capacity of methane relative to nitrogen increases with increasing concentration of methane. Methane out competes nitrogen for sites. This bodes well for the target application of upgrading gob gas (roughly 80% methane) to pipeline quality (roughly 97% methane).

Recommended Adsorbents from Industrial Partner

Our industrial partner, Joe D'Amico of D'Amico Technologies, has a long and successful history in the industry with developing and deploying systems for upgrading natural gas. He has recommended several adsorbents, including activated carbon from PICA, Barnaby-Sutcliffe, and Westvaco. In addition, he has recommended a zeolite from Davison. At present, Mr. D'Amico has provided samples from Barnaby-Sutcliffe and we have procured samples from PICA. We anticipate samples from Westvaco and Davison to arrive in early February.

Selection of Adsorbents for Experimental Validation

The following adsorbents have been selected for testing in Task 1.2.

- Activated Carbon
  - PICA
  - Barnaby-Sutcliffe
  - AX-21 microporous carbon
  - Carbonized foams
- Zeolites
  - Davison
  - Na-X substituted zeolite (from reference M2)
  - Li-exchanged zeolite (from reference M52)
- Molecular Gate from Engelhard – if available – for preferential nitrogen adsorption

Results and Discussion

The open literature, patent information, and vendor contacts were surveyed to identify adsorbent candidates for experimental validation and subsequent demonstration in a MPT-based ultra-fast TSA separation for methane upgrading. The leading candidates for preferential adsorption of methane over nitrogen are highly microporous carbons. One candidate for preferential adsorption of nitrogen over methane emerged—Molecular Gate™ zeolite from Engelhard Corporation.

Task 1.1 was completed with the selection of eight adsorbents for additional study. The adsorbents include four carbons, three zeolites, and the preferential nitrogen adsorbent from Engelhard, if available.

Task 1.2. Adsorbent Evaluations

Objective

The objective of this task was to identify an adsorbent candidate suitable for initiating a conceptual system design and a subsequent bench-scale demonstration. The testing program evaluated capacity and differential capacity as a function of temperature, pressure, and inlet composition.

Experimental Description

The test system is designed to measure capacity as a function of temperature, pressure, and composition for different solid granulated forms of adsorbents. The system includes an adsorbent bed with heat exchanger to maintain isothermal operation during experiments (as shown in Figure 1).

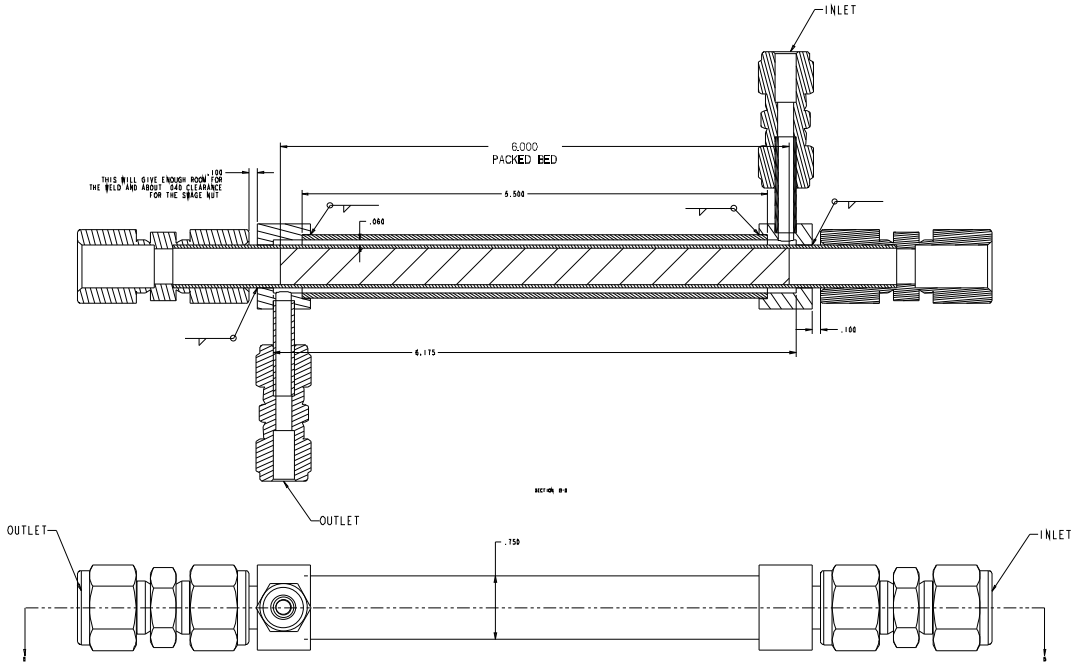

Figure 1. Adsorbent testing apparatus. Process gases flow downward through the (vertically mounted) adsorbent bed in the center tube and heat exchange fluid flows co-currently in an outer annulus to maintain near isothermal operation.

The adsorbent bed consists of an inner tube with 1/2” OD housed within an outer tube of 3/4" OD. The length of the adsorbent bed is 6” inches, for a typical loading of 5-7 grams of adsorbent (based on 0.35-0.5g/mL density). A 50/50 mix of glycol and water heat exchange fluid flows through the annulus at 4 gallons/min. The fluid temperature can be varied from 0 °C to 80 °C, allowing testing with bed temperatures as high as 60 °C.

The system (as shown in Figure 2) also includes a feed line and a purge gas line that can each be electronically turned off and on. The feed line can add a custom mix of methane and nitrogen. The purge line is used to "clean" or desorb the solutes between experiments.

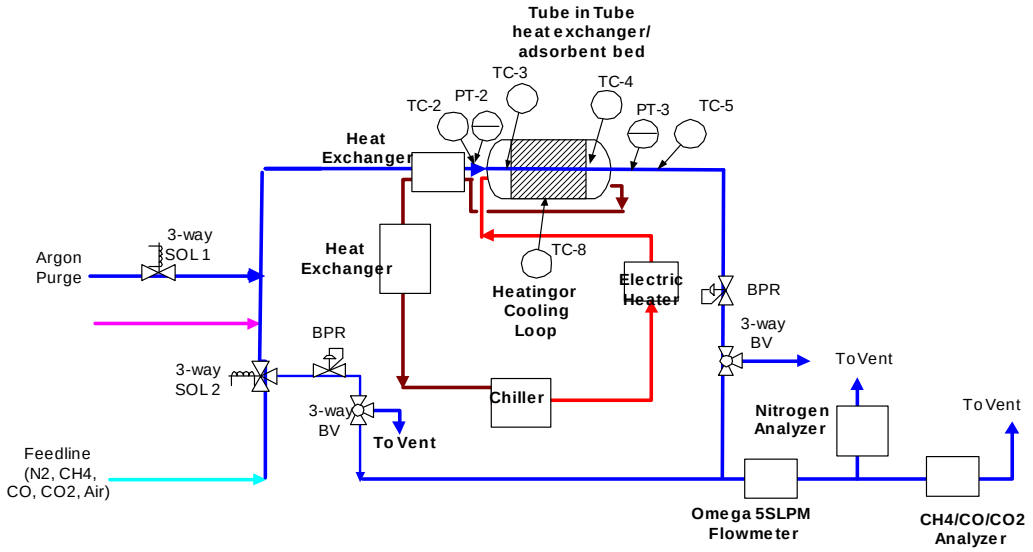

Figure 2. Adsorbent testing system flow diagram.

The feed gases are metered separately through Brooks mass flow controllers, mixed, and can either be fed directly to the sample analysis line or fed through a small preheater and into the adsorption bed. At the start of each test while argon is fed to the adsorption bed, the feed gases are routed via 3-way valves to the analyzer system. The use of a back pressure regulator immediately downstream of the adsorbent bed allowed testing of adsorbents at pressures as high as 400 psig. After leaving the adsorption bed and before passing through the back pressure regulator to drop the pressure to near-ambient, 1 liter of argon was added to the outlet mixture to minimize the delay time between the analyzers and the bed exit (this represents a 50% dilution of the inlet gas flow). The outlet gases are then sent to either the bypass vent line or to the sample analysis line which includes an Omega mass flow meter, a Raytech Nitrogen analyzer and a California Analytical Instruments $CH_4/CO/CO_2$ analyzer. Although not shown explicitly in Figure 2, the flow exiting the flowmeter in the sample analysis line is split to feed the nitrogen and $CH_4/CO_2/CO$ analyzers in parallel.

The procedure for running each experiment follows.

1) Grind adsorbent particles with mortar and pestle or small ball mill.
2) Sieve the particles to recover the 212- to 425-micron particle size fraction (40-70 mesh).
3) Load the test apparatus with a known weight of undesiccated adsorbent (5-7 gms) from the above particle size fraction.
4) Calibrate flow controllers and analyzers against known standards.
5) Purge the bed with argon at expected total feed flow rate until no other gases are seen by the analyzers.

6) Set system pressure with the BPR (either 0 psig or 100 psig).
7) Set system temperatures by adjusting the temperature of the chiller and the pre-heater.
8) Set feed flow rates and bypass the adsorbent bed, sending them to the analyzer to check composition.
9) Send feed flows to vent and purge (argon) flow to the adsorbent bed and sample analysis line until no more methane or nitrogen is detected in outlet stream.
10) Simultaneously start the feed to the adsorbent bed and stop the purge gas (argon) flow at time t0 by opening the valve solenoid-1 and closing solenoid-2.
11) Record the measured outlet flow rates and compositions as a function of time via LabView program.
12) After steady-state is established, stop test by closing solenoid-1 and opening solenoid-2 (flow purge gas over the bed to remove the sorbed solutes).

Once the testing is complete, the data can be recalled at any given time interval (1 second intervals were used for the initial tests with PICA carbon, MGN-101; for enhanced response resolution and improved accuracy, 0.5 second intervals were adopted for subsequent evaluations). The data collection system records the time when the solenoids are switched giving an exact start time to the test. The system dead time (about 1 second at 2 psig and 7 seconds at 100 psig) and the delay between the adsorbent bed exit and the analyzers (typically 1-3 seconds) were taken into account when calculating breakthrough time and capacity.

Calculating Capacity – initial method

Adsorbent capacity was calculated for each test condition as the cumulative milligrams of each component fed to the system less the cumulative milligrams of each component exiting the system per gram of adsorbent.

$$capacity = \frac{\sum_{j=1}^{n} (mg\ i\ in - mg\ i\ out)_j}{grams\ of\ adsorbent}$$

where mg i in or out is the mass of component i entering or exiting the bed at time increment j (with a total of n time increments). Note that the dead time, or the time required for the process flows to first reach the adsorbent bed is not included in the calculation. The mass of each component i (CH_4 and N_2) entering and leaving the adsorbent bed was calculated at each time interval j and summed over all time periods from the end of the dead time to the time when each component ceased adsorbing according to the following equations:

$$mg\ i\ in_j = SLPM\ i\ in_j \cdot \left(\frac{1\ min}{60\ sec}\right) \cdot \left(\frac{1\ mmol\ i / min}{0.0224\ SLPM\ i}\right) \cdot \left(\frac{MW_i\ mg\ i}{mmol\ i}\right) \cdot time\ interval_j$$

$$mg\ i\ out_j = SLPM\ out_j \cdot \left(\frac{1\ min}{60\ sec}\right) \cdot \left(\frac{1\ mmol / min}{0.0224\ SLPM}\right) \cdot y_{i,j} \left(\frac{MW_i\ mg\ i}{mmol\ i}\right) \cdot time\ interval_j$$

where SLPM is the flow rate (total or component i) converted to standard liters per minute (standard conditions being 0 °C and 1 atm), MW_i is the molar mass of component i, $y_{i,j}$ is the mole fraction of component i at time j, and time $interval_j$ is the time increment at time j in seconds. The stream composition ($y_{i,j}$) exiting the bed at time j was assumed to be the mole fraction measured in the sample analysis line analyzers after a delay period had elapsed. This delay period (about 0.5 to 1 second longer for CH_4 than for N_2) was the average time needed for the gas to flow from the bed exit to the analyzer, given the average outlet flow rate during that time. Because of the large proportion of process gases which were adsorbed, variations in the outlet flow rate were very significant and the calculated delay period was substantial (typically 7-13 seconds).

Calculating capacity – refined method

In order to calculate the capacity of each adsorbent for methane and nitrogen, three types of responses were measured in real time and recorded every 0.5 seconds: the mass flow meter reading for total outlet flow, the mole fraction methane in the outlet, and the mole fraction nitrogen in the outlet. The time at which the feed to the adsorbent bed was switched by solenoid valve from argon to the feed mixture was also recorded to the nearest 0.5 seconds. The adsorbent capacity was calculated for each component i (CH_4 or N_2) as in Equation 1:

$$capacity = \frac{n_{i,\,adsorbed} \cdot MW_i}{grams\ adsorbent} \qquad (1)$$

where $n_{i,\,adsorbed}$ is the moles of component i adsorbed and MW_i is the corresponding molecular weight. The moles adsorbed of each component i was calculated by mass balance: moles adsorbed equals the cumulative number of moles entering the adsorbent bed ($n_{i,\,in}$) less the moles exiting the adsorbent bed ($n_{i,\,out}$) less the moles held up in the void space of the adsorbent bed ($n_{i,\,bed}$) as shown in Equation 2. Note that the cumulative moles in and the cumulative moles out do not include the gas flowing during the initial dead time (during which time argon is being purged from the inlet line and replaced with the feed mixture).

$$n_{i,\,adsorbed} = n_{i,\,in} - n_{i,\,out} - n_{i,\,bed} \qquad (2)$$

Given the void volume of the adsorbent bed ($V_{bed\ void}$), the mole fraction of component in the inlet stream (y_i), and the bed temperature (T_{bed}) and pressure (P_{bed}), the moles held up in the adsorbent bed is easily calculated from the ideal gas law (Equation 3).

$$n_{i,\,bed} = \frac{P_{bed} \cdot y_i \cdot V_{bed\ void}}{R_{gas,\,universal} \cdot T_{bed}} \qquad (3)$$

The cumulative moles entering the adsorbent bed is found as shown in Equation 4 below

$$n_{i,\,in} = \sum_{j=1}^{n} SLPM\ \ i\ in_j \cdot \left(\frac{1\,min}{60\,sec}\right) \cdot \left(\frac{1\,mol\ i/min}{22.4\,SLPM\ \ i}\right) \cdot \Delta t_j \qquad (4)$$

where "SLPM i in_j" is the flow rate of component i (CH_4 or N_2) in standard liters per minute (standard conditions being 0 °C and 1 atm) at the bed entrance at time j, and Δt_j is the time increment at time j in seconds. The cumulative moles leaving the adsorbent bed is found as shown in Equation 5 below:

$$n_{i,\,out} = \sum_{j=1}^{n} SLPM\ \ out_j \cdot \left(\frac{1\,min}{60\,sec}\right) \cdot \left(\frac{1\,mol/min}{22.4\,SLPM}\right) \cdot y_{i,j} \cdot \Delta t_j \qquad (5)$$

where "SLPM out_j" is the total flow rate out of the bed in standard liters per minute (standard conditions being 0 °C and 1 atm) at the bed exit at time j, y_{ij} is the mole fraction of component i at the bed exit at time j, and Δt_j is the time increment at time j in seconds. Note that since mole fractions were not measured at the bed exit, but further downstream at the analyzer after addition of additional Ar, the composition at the bed exit was assumed to be offset in time from the composition at the analyzer by the time required for the gas to travel between the two. The reading of the mass flow meter for the total outlet flow was offset from the actual total outlet flow by a factor which showed a linear dependence on gas composition as shown below in Equation 6.

$$F_{total,\,reading} = F_{Ar} \cdot K_{Ar} + F_{N2} \cdot K_{N2} + F_{CH4} \cdot K_{CH4} \qquad (6)$$

In Equation 6, F_i represents the true flow rate in SLPM at the mass flow meter for each component i and the K_i values are correction factors determined from calibration with known mixtures of Ar, CH_4, and N_2 (K_{Ar} = 0.964, K_{CH4} = 1.889, and K_{N2} = 1.431). If ($F_{total,\,actual} - F_{N2} - F_{CH4}$) is substituted for F_{Ar} in Equation 6 and the equation re-arranged, the expression below (Equation 7) is obtained for actual total outlet flow rate.

$$F_{total,\,actual} = \frac{1}{K_{Ar}} \cdot \left[F_{total,\,reading} + F_{N2} \cdot \left(K_{Ar} - K_{N2}\right) + F_{CH4} \cdot \left(K_{Ar} - K_{CH4}\right)\right] \qquad (7)$$

Using the above equation, the actual total flow rate was iteratively calculated from the mass flow meter reading and the known composition of the gas at any given time. Iteration was necessary since only the mole fraction and not the flow rate of each component was known. The mass flow meter reading gave a good first guess for the iteration, which converged to give an actual flow rate after 2 iterations. The argon flow rate exiting the bed was calculated as the total argon flow rate ($F_{total,\,actual} - F_{N2} - F_{CH4}$) corresponding to the iterative solution to Equation 7 less the 1 SLPM downstream of bed purge argon flow.

It should be noted that the composition of the gas was measured at the gas analyzers, so the composition at the mass flow meter was assumed to be offset in time from the composition at the analyzer by the time required for the gas to travel between the two. In addition, a 1.2 second intrinsic methane analyzer delay was assumed as this gave a good match between the outlet flow

readings and the methane analyzer readings under a wide variety of conditions. It was assumed that once the outlet composition reached an asymptotic value (at long run times beyond the point of breakthrough) that the outlet molar flow rates were equivalent to the inlet molar flow rates. The reading from the continuous nitrogen analyzer consistently showed a sharp increase at the time which nitrogen began to be present in the outlet stream being analyzed. This sharp increase, or spike, was used to identify the beginning of the nitrogen peak. Since the analyzer showed a complex dependency on time-on-stream as well as on methane and argon concentration, Equation 8 was used to simulate the nitrogen evolution step-function curve at the analyzer.

$$SLPM_{N2} = \frac{\max SLPM_{N2}}{1 + \exp\left[-\frac{(t - \tau_1)}{\tau_2}\right]} \qquad (8)$$

where "max $SLPM_{N2}$" is the asymptotic N_2 flow rate (based on inlet flows), t is the time in seconds, and τ_1 and τ_2 are fitting parameters which are adjusted to match the N_2 peak start time indicated by the N_2 analyzer and the calculated actual outlet total flow and argon flow as a function of time. The physical sense of τ_1 and τ_2 can be understood as follows: τ_1 is the average of the peak start time (detected by N_2 analyzer) and the peak duration time (in seconds), and τ_2 is the peak duration time in seconds divided by 8.8. Since the adsorbent bed was flushed with Ar before starting the flow of CH_4 and N_2 at the inlet, Ar gas was flushed out the exit of the bed during the time in which CH_4 and N_2 were adsorbed. The N_2 peak duration time was estimated via the response seen in the measured outlet flow (which is composition sensitive), adjusting the estimate until the calculated Ar outlet flow curve and calculated actual total outlet flow curves were smooth and continuous during the transition in composition of the outlet flow. In a few cases, where the N_2 peak was obscured by the CH_4 peak, the N_2 peak duration time for the 90/10 CH_4/N_2 inlet mixture was assumed to be the same as for the 50/50 inlet mixture at the same conditions of temperature and pressure. Although this method of nitrogen evolution estimation introduces some additional error into the nitrogen capacity measurement, the effect seems to be minor (less than 10%) in most cases.

Preliminary Adsorbent Evaluations

The first evaluated adsorbent was activated carbon (MGN-101) from PICA, Inc. The carbon sample demonstratd preferential capacity for methane over nitrogen, as well as a reasonable thermal swing differential capacity (15 mg/gm methane and less than 2 mg/gm nitrogen between 6 C and 40 C at both 2 psig and 100 psig.) for a 90% methane and 10% nitrogen mixture). Surprisingly, a similar methane swing capacity at 2 psig was measured, while the nitrogen swing capacity dropped below 1 mg/gm. The mixture composition was relevant because gob gas contains nearly 85% methane and must be purified to 97% methane for pipeline quality. These initial results showed that high capacity adsorbents are available.

The preliminary results of adsorption capacity testing for the PICA Carbon adsorbent are shown in Tables 5 and 6 and in Figures 3 through 8. The capacity data (Tables 5 and 6) show the expected increase in capacity with increasing mole fraction of a given component. For the most part, the data show the expected trends of increasing capacity with decreasing temperature and increasing pressure. However, a few data points (especially nitrogen) do not show the expected decrease in capacity as temperature is increased. This was attributed to errors in the nitrogen analyzer measurements, and possibly errors in the outlet flow meter readings (as it was calibrated using the inlet composition, while the actual composition varied throughout the testing). Following these tests, experimental changes were implemented to improve the accuracy of the capacity estimation in the subsequent tests.

Temp (C)	Pressure (psig)	CH4 flow (sccm)	N2 Flow (sccm)	CH4 Capacity (mg/g)	N2 Capacity (mg/g)
6	2	100	900	5.8	20.8
6	2	500	500	21.2	9.2
6	2	900	100	32.2	1.3
23	2	100	900	4.1	19.1
23	2	500	500	14.2	10.2
23	2	900	100	21.6	2.6
40	2	100	900	2.7	11.5
40	2	500	500	10.0	5.6
40	2	900	100	16.4	1.8

Table 5. PICA Carbon MGN-101, capacity as a function of temperature and mixture composition near 1 atm

Temp (C)	Pressure (psig)	CH4 flow (sccm)	N2 Flow (sccm)	CH4 Capacity (mg/g)	N2 Capacity (mg/g)
6	100	100	900	16.4	64.8
6	100	500	500	70.1	21.1
6	100	900	100	94.2	5.3
23	100	100	900	12.7	37.8
23	100	500	500	55.4	26.8
23	100	900	100	94.4	18.6
40	100	100	900	9.6	53.6
40	100	500	500	41.9	23.8
40	100	900	100	79.5	2.9

Table 6. PICA Carbon MGN-101 capacity as a function of temperature and mixture composition near 100 psig.

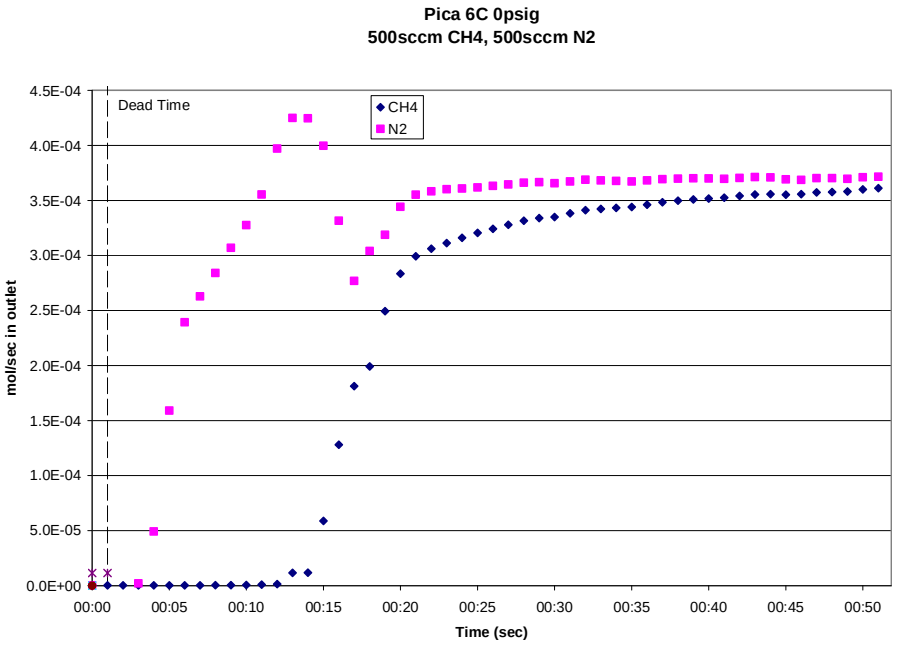

Figure 3. Outlet molar flow rate of nitrogen and methane for equimolar feed mixture, 6 C and 2 psig. Dead time is 1second.

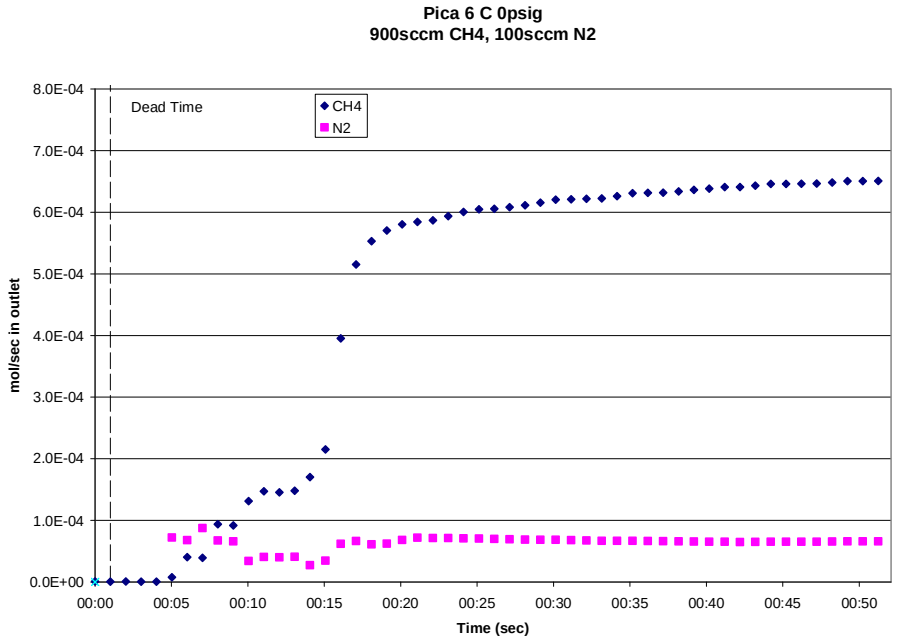

Figure 4. Outlet molar flowrate of nitrogen and methane for 90% methane and 10% nitrogen at 6 C and 2 psig. Dead time is 1 second.

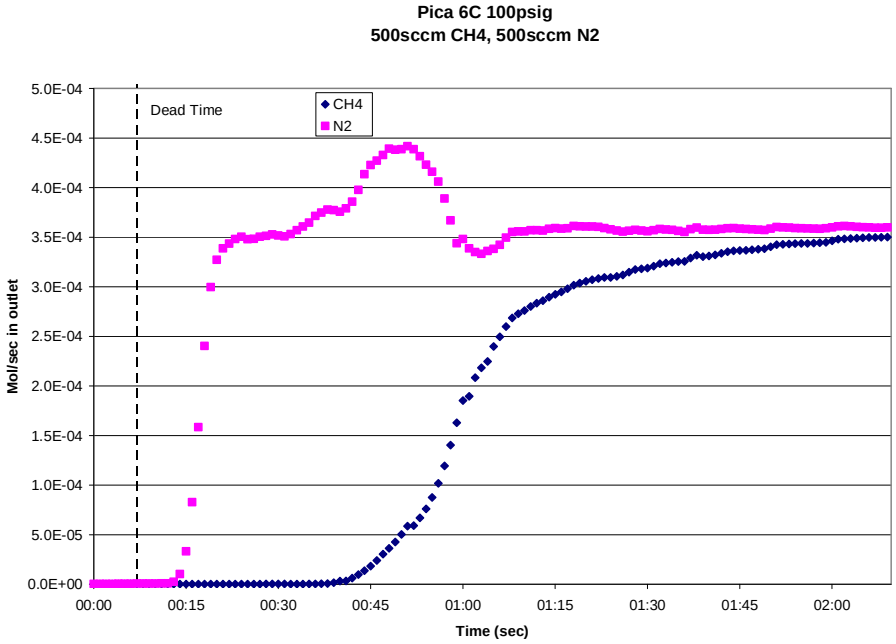

Figure 5. Outlet molar flowrate of nitrogen and methane for equimolar mixture at 6 C and 100 psig. Dead time is 7.3 seconds.

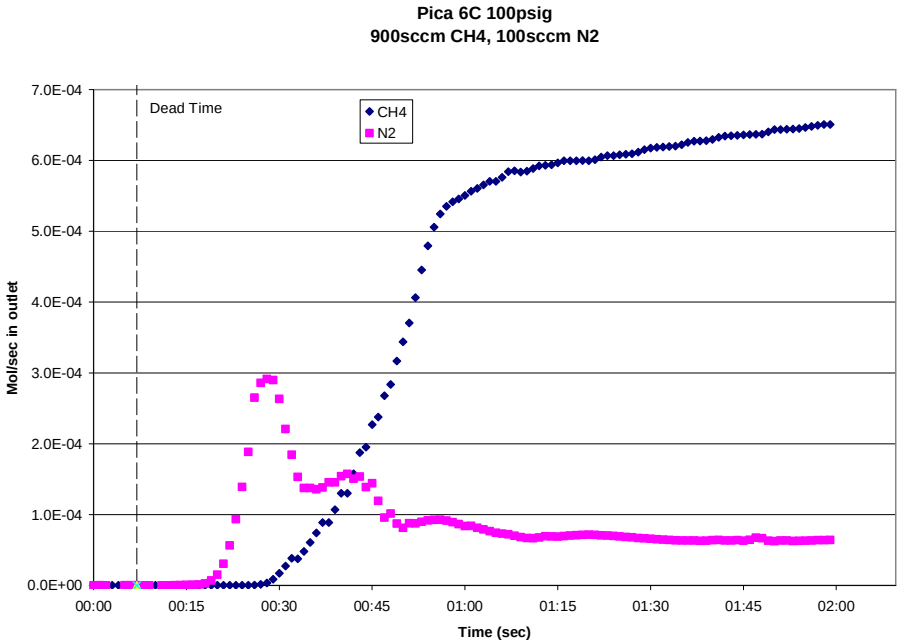

Figure 6. Outlet molar flowrate of nitrogen and methane for 90% methane and 10% nitrogen at 6 C and 100 psig. Dead time is 7.3 seconds.

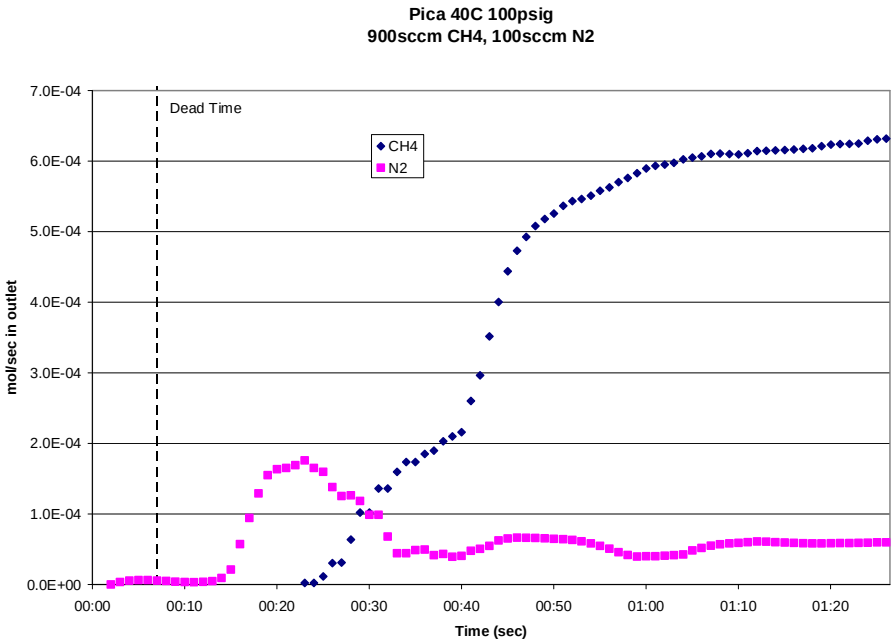

Figure 7. Outlet molar flowrate of nitrogen and methane for 90% methane and 10% nitrogen at 40 C and 100 psig. Dead time is 7.3 seconds.

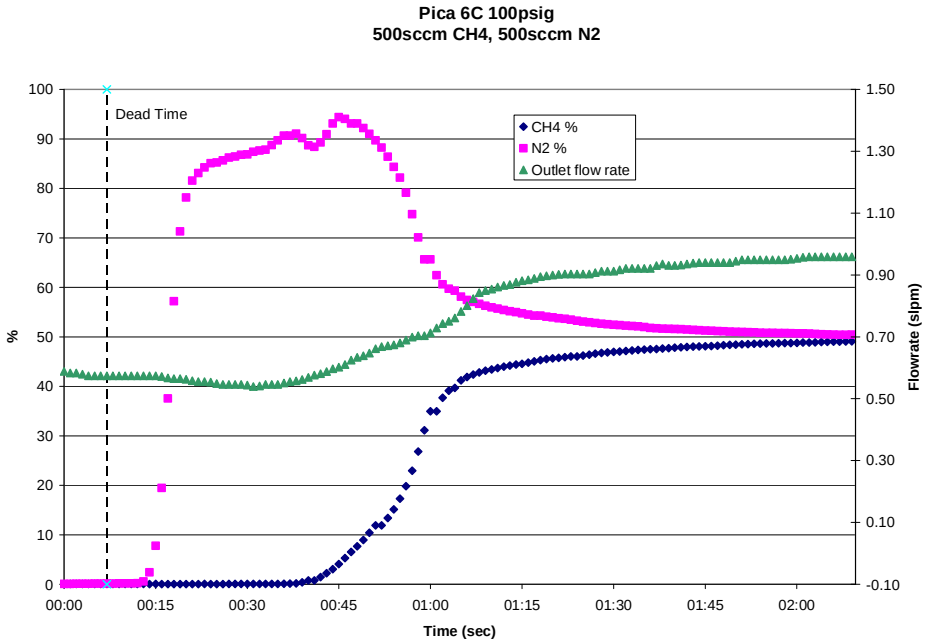

Figure 8. CH_4 and N_2 concentrations at the exit of the adsorbent bed (left axis) and total outlet flow rate (right axis) for equimolar inlet mixture at 6 C and 100 psig. Dead time is 7.3 seconds.

Experimental System Upgrades

During the initial data collection phase, experimental issues were identified for future upgrading. One specific issue raised that may impact the quality of the first data set collected is the response factor of the methane and nitrogen sensors. The cited vendor response times were less than one second. Observed response times and lag was found to be strongly dependent upon the effluent flowrate and increased to tens of seconds to achieve full response for very low flowrates. In the next set of tests, an additional flow line was added upstream of the sensor to boost the total flow and reduce the sensor response lag. Another specific issue identified was the dependence of the mass flow meter calibration on gas composition. A composition dependent calibration curve was developed for the subsequent tests.

Additional Adsorbent Evaluations

Adsorbents tested included three types of carbon and three types of zeolites. Adsorbent capacity was evaluated for all adsorbents at pressures of 2 psig and 100 psig and temperatures of 6, 23, 40, and 60 °C for 50/50 (v/v) and 90/10 (v/v) feed mixtures of methane and nitrogen. This was done so that for a given pressure and gas composition the differential capacity for methane between any two temperatures could be compared to the differential capacity for nitrogen between those same two temperatures. In addition, one of the most promising adsorbents (Calgon carbon) was tested for the above composition and bed temperature combinations at 200, 300, and 400 psig. Extra tests on the Barnaby-Sutcliffe carbon were also included using 10/90 (v/v) methane/nitrogen mixtures.

Following the experimental modifications to improve capacity measurement (adding argon to the outlet flow to reduce the time required for the outlet flow to reach the analyzers), the initial PICA carbon capacity tests reported above were repeated and updated for the following plots.

Typical analyzer and mass flow meter reading curves are shown in Figure 9. Figures 10 and 11 depict outlet flow curves produced from typical tests at 100 psig with mixtures of 50/50 and 90/10 (v/v) methane/nitrogen, respectively. The results of the adsorbent capacity screening tests are shown in Tables 7-11. Tables 7 and 8 summarize the measured *carbon* adsorbent capacities for the 2 psig and 100 psig tests, respectively. Table 9 shows the measured Calgon carbon adsorbent capacities for the 200, 300, and 400 psig tests. Tables 10 and 11 summarize the measured *zeolite* adsorbent capacities for the 2 psig and 100 psig tests, respectively. One of the zeolite adsorbents was obtained from Alpha Aesar. These capacities can then be used to determine differential capacities between any two temperature conditions for a given inlet composition and pressure (the differential capacity for a given component is simply the difference between the two measured capacities for that component at the low and high temperature).

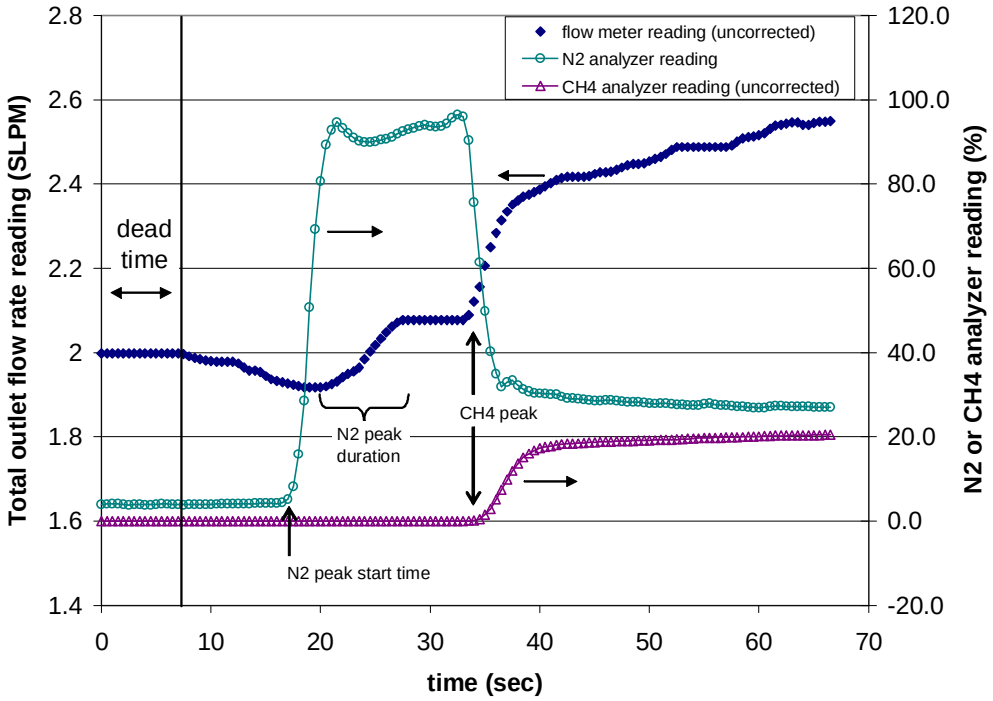

Figure 9. Outlet flow rate reading from mass flow meter (left axis) and nitrogen and methane analyzer readings (right axis, before calibration correction) for adsorption capacity tests on Calgon carbon adsorbent using an equimolar feed mixture at 60 °C and 100 psig. Dead time was 7 seconds.

It is desirable to have a high differential capacity for methane and a low differential capacity for nitrogen over a given temperature range in order to affect separation by thermal swing adsorption. In general, the carbon adsorbents had much higher differential capacities than the

zeolite adsorbents over the range of conditions tested. The 2 psig pressure capacities were always lower than the corresponding 100 psig capacities, so the best adsorbent for a 90/10 mixture over the interval of 40-60 °C was identified from the data at 100 psig. This adsorbent (Calgon) was further tested at 200, 300, and 400 psig, but surprisingly, performance at these higher pressures showed no significant increase in differential capacity as compared to the 100 psig performance. Improvements in system testing following preliminary evaluations have yielded both higher quality data and a self consistent comparisons between all six adsorbents.

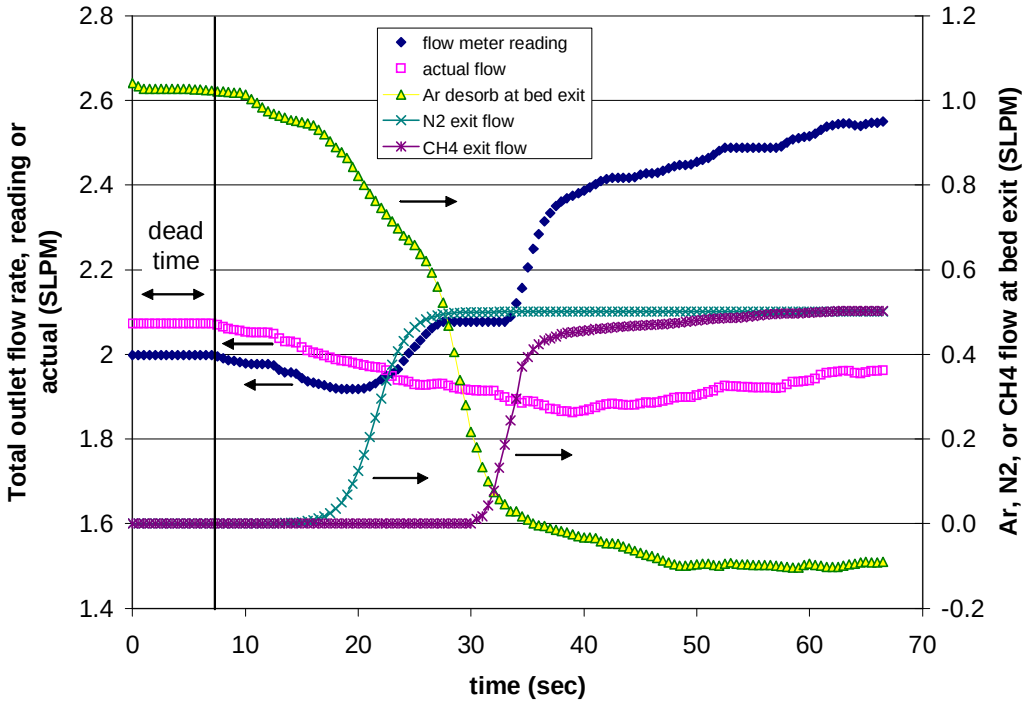

Figure 10. Outlet flow rate reading from mass flow meter and corrected total outlet flow (left axis) and argon, nitrogen, and methane flows at the sorbent bed exit (right axis) for adsorption capacity tests on Calgon carbon adsorbent while feeding 0.5 SLPM CH_4 and 0.5 SLPM N_2 at 60 °C and 100 psig. Dead time was 7 seconds.

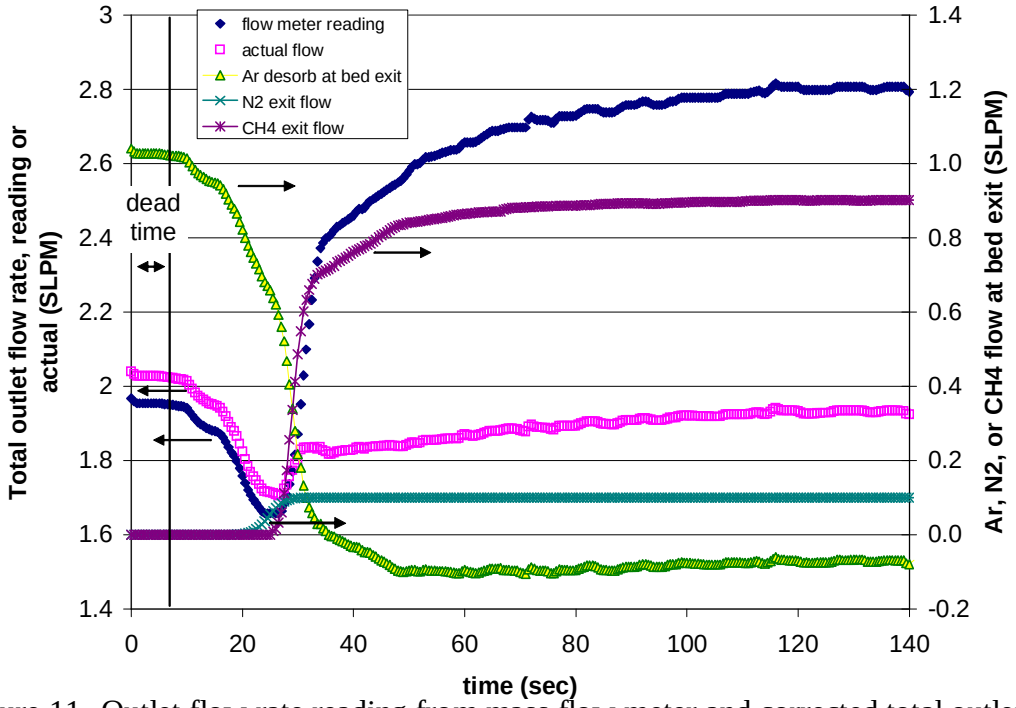

Figure 11. Outlet flow rate reading from mass flow meter and corrected total outlet flow (left axis) and argon, nitrogen, and methane flows at the sorbent bed exit (right axis) for adsorption capacity tests on Calgon carbon adsorbent while feeding 0.9 SLPM CH_4 and 0.1 SLPM N_2 at 60 °C and 100 psig. Dead time was 7 seconds.

Carbon sorbents- 2 psig			Barnaby-Sutcliffe		Calgon		PICA	
Temp (C)	CH4 flow (sccm)	N2 Flow (sccm)	CH4 Capacity (mg/g)	N2 Capacity (mg/g)	CH4 Capacity (mg/g)	N2 Capacity (mg/g)	CH4 Capacity (mg/g)	N2 Capacity (mg/g)
6	100	900	6.5	10.1	-	-	-	-
6	500	500	19.7	7.7	16.4	6.4	18.2	7.6
6	900	100	26.7	2.5	23.6	1.9	24.6	2.1
23	100	900	3.8	5.7	-	-	-	-
23	500	500	12.3	4.8	11.4	4.2	13.3	6.3
23	900	100	18.2	1.4	16.1	1.3	16.9	1.6
40	100	900	2.3	3.2	-	-	-	-
40	500	500	9.4	2.8	7.8	4.3	8.4	5.0
40	900	100	12.3	0.9	9.5	1.0	10.9	1.3
60	100	900	1.7	4.3	-	-	-	-
60	500	500	5.1	2.4	4.8	2.9	4.9	2.9
60	900	100	8.3	0.5	7.1	0.8	5.7	0.9

Table 7. Carbon sorbent capacities measured over a range of temperature and feed mixture compositions at near ambient pressure.

Carbon sorbents- 100 psig			Barnaby-Sutcliffe		Calgon		PICA	
Temp (C)	CH4 flow (sccm)	N2 Flow (sccm)	CH4 Capacity (mg/g)	N2 Capacity (mg/g)	CH4 Capacity (mg/g)	N2 Capacity (mg/g)	CH4 Capacity (mg/g)	N2 Capacity (mg/g)
6	100	900	16.5	40.7	-	-	-	-
6	500	500	55.5	27.1	44.4	22.5	54.9	28.6
6	900	100	75.7	6.1	63.0	5.0	75.0	5.9
23	100	900	12.4	32.1	-	-	-	-
23	500	500	44.2	25.6	36.0	18.7	40.0	18.9
23	900	100	57.8	5.1	54.6	4.1	59.6	4.3
40	100	900	8.6	24.9	-	-	-	-
40	500	500	36.9	22.8	31.7	17.6	28.9	13.3
40	900	100	48.1	4.4	41.6	3.5	42.9	2.6
60	100	900	7.5	22.2	-	-	-	-
60	500	500	28.0	18.4	23.4	10.7	25.3	11.1
60	900	100	39.6	3.8	31.8	2.5	35.3	2.6

Table 8. Carbon adsorbent capacities measured at 100 psig

Calgon carbon- high P			200 psig		300 psig		400 psig	
Temp (C)	CH4 flow (sccm)	N2 Flow (sccm)	CH4 Capacity (mg/g)	N2 Capacity (mg/g)	CH4 Capacity (mg/g)	N2 Capacity (mg/g)	CH4 Capacity (mg/g)	N2 Capacity (mg/g)
6	500	500	52.1	29.8	66.5	40.0	76.1	45.1
6	900	100	66.2	6.3	91.4	8.5	112.7	10.2
23	500	500	41.8	23.8	51.2	34.2	65.5	39.5
23	900	100	63.1	5.4	81.3	7.5	95.2	8.4
40	500	500	35.3	22.0	43.2	26.7	50.5	31.7
40	900	100	51.5	4.6	70.2	6.3	87.5	8.3
60	500	500	33.2	18.4	39.4	25.8	54.6	32.9
60	900	100	45.4	3.8	63.3	5.3	84.6	7.4

Table 9. Measured Calgon carbon sorbent capacities as a function of temperature and mixture composition for 200, 300, and 400 psig bed pressures.

Zeolites, 2 psig			Z-10-02		Z-10-06		Alpha Aesar	
Temp (C)	CH4 flow (sccm)	N2 Flow (sccm)	CH4 Capacity (mg/g)	N2 Capacity (mg/g)	CH4 Capacity (mg/g)	N2 Capacity (mg/g)	CH4 Capacity (mg/g)	N2 Capacity (mg/g)
6	500	500	5.5	3.3	5.7	5.5	4.7	4.2
6	900	100	7.5	1.2	8.2	1.4	6.9	0.9
23	500	500			3.6	2.6	3.1	2.2
23	900	100			6.4	0.8	4.7	0.4
40	500	500	1.8	1.4	3.2	2.0	2.4	1.8
40	900	100	2.1	1.3	4.1	1.0	2.5	0.3
60	500	500			1.5	1.6	1.0	0.9
60	900	100			2.5	0.6	1.2	0.2

Table 10. Zeolite adsorbent capacities measured over a range of temperature and feed mixture compositions at near ambient pressure.

Zeolites, 100 psig			Z-10-02		Z-10-06		Alpha Aesar	
Temp (C)	CH4 flow (sccm)	N2 Flow (sccm)	CH4 Capacity (mg/g)	N2 Capacity (mg/g)	CH4 Capacity (mg/g)	N2 Capacity (mg/g)	CH4 Capacity (mg/g)	N2 Capacity (mg/g)
6	500	500	24.5	14.2	24.7	14.7	21.7	13.7
6	900	100	36.0	4.4	39.1	4.5	34.0	3.4
23	500	500			18.6	13.9	16.8	9.2
23	900	100			28.0	3.2	28.2	2.4
40	500	500	15.5	9.3	15.8	8.9	12.4	7.1
40	900	100	23.7	2.1	24.3	2.1	20.9	1.7
60	500	500			13.4	8.7	-	-
60	900	100			22.5	2.0	-	-

Table 11. Zeolite adsorbent capacities measured at 100 psig

Conclusions

Measured adsorption and differential capacities between 40 and 60 °C were highest for microporous carbon. Both the Calgon AX-21 carbon and the Barnaby-Sutcliffe carbon gave similar performance at 100 psig. Surprisingly, the performance at 100 psig was better than either low pressure (2 psig) or higher pressure (>200 psig) for the Calgon carbon. An operating pressure of 100 psig was selected for the system study.

Task 2.1. Conceptual System Process Design

Objective

The goals of the Conceptual System Process Design involve defining:

- The critical unit operations, including order
- Mass and energy balance of the required unit operations
- Capacity (duty) and performance assumptions of each identified unit operation
- Temperature, pressure, flow rate, and composition of each process stream
- Metrics of product recovery and thermal efficiency

System Design Basis

To provide a basis for the system study, several variables were fixed and conventions adopted.

- The methane upgrading system was sized for 3 million standard cubic feet per day (MMSCFD) of sub-quality natural gas entering from a gob gas well or wells
- Composition of the gas from the well is: 70% CH_4, 4% O_2, 22% N_2, 4% CO_2 and saturated with water at ambient conditions
- Composition required for the pipeline: 96% CH_4, <4% N_2 or CO_2, 10 ppm O_2 and dry to -40°C at 600 psi
- Inlet temperature and pressure from the well: 20°C and 1 psig
- Outlet temperature and pressure to pipeline: <200°C and 600 psig

Methane Upgrading System

The system study evaluated the complete process for upgrading coal-bed methane to pipeline quality. This process, as shown in Figure 12, consists of six steps: process compression, dehydration, nitrogen rejection, oxygen removal, carbon dioxide rejection and sales compression. Below is a simplified diagram showing the basic processing steps.

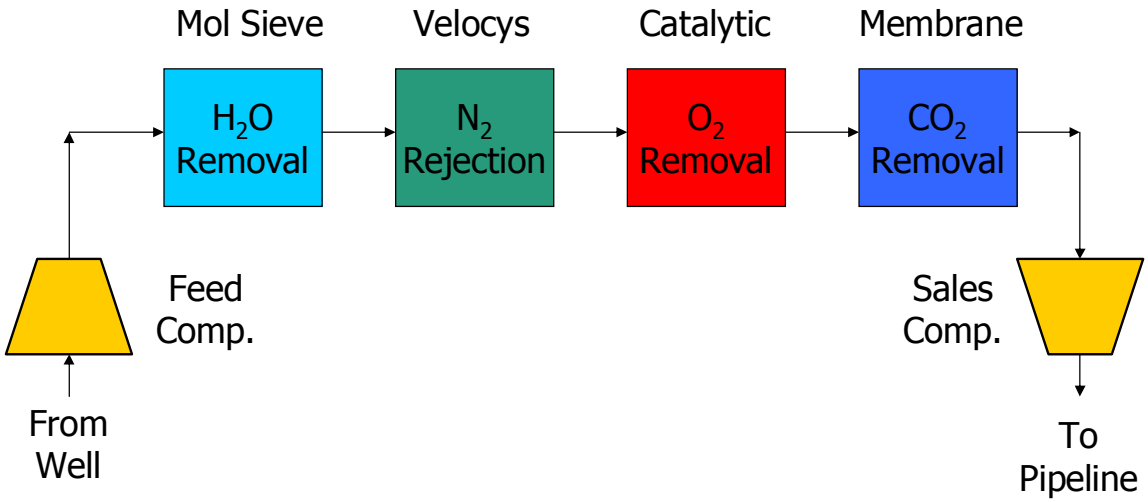

Figure 12. Methane upgrading process system configuration

The complete process was modeled in detail using ChemCAD, a process simulation software package. The case displayed assumes that the Velocys Technology NRU can achieve 90% recovery, the target recovery and system design point.

The requirements and equipment needed to perform the major processing step are discussed. Background information for the technology and economics was obtained from an EPA Coalbed Methane Outreach Program study titled, *Technical and Economic Assessment of Potential to Upgrade Gob Gas to Pipeline Quality*, and published in 1997.

Compression

The methane upgrading system requires two separate gas compression operations. To enter the process the gob gas stream must be pressurized from 1 to approximately 120 psig. Then after the final upgrading processing step (CO_2 removal), the product gas must again be compressed to 600 psig to enter the sales natural gas pipeline.

The feed compressor requires two stages and approximately 250 horsepower to compress the entire 3 MMSCFD of sub-quality gas. The estimated cost of this unit, including inter and after coolers, vapor-liquid separators and associated auxiliary equipment is $477,000.

Sales compression is less costly (estimated at $190,000) for two reasons. First, only one stage is required to raise the pressure of a gas stream from 100 psig (after a 20 psi loss through the upgrading system) to 600 psig. Second, the quantity of gas remaining after the processing steps is less than 2 MMSCFD. The large volume reduction is due to the removal of sub-quality components, such as nitrogen and carbon dioxide, and the loss of some methane.

Dehydration

Compression will reduce the concentration of water vapor to the dew point (saturation) at the inlet to the removal stage; for example the water vapor dew point at 600 psig is 78°C (172°F) and 0.47 mole percent. Therefore addition dehydration is needed to meet the pipeline specification of –40°C dew point (0.00039 mole percent water vapor). Typically molecular sieves are used to remove water vapor from natural gas processes and represent a commercial basis for this unit operation. The dehydration subsystem capital cost is estimated to be $40,000 for a 3 MMSCFD plant; this is consistent with the EPA report.

Nitrogen Recovery Subsystem

As the NRU is the focus of the project, the cost target and macro processing conditions are exclusively discussed in this section. Salient details gleaned from the system study and computational modeling are described in a dedicated section below.

The price target for a 3 MMSCFD Velocys Technology NRU is $1.35 million, which is a 20 percent capital cost reduction compared to conventional technology. The benchmark pricing for a pressure swing adsorption (PSA) system with a similar capacity is from the EPA report.

The Ultra-Fast TSA system will cycle between 40 and 60°C every two seconds, one second per phase, and achieve a methane recovery rate of 90 percent. The tail gas, containing the remaining 10 percent of the methane will be used to provide the energy needed to swing the adsorber temperature. The operating pressure will be 120 psig and the predicted system pressure drop will be approximately 10 psig.

Catalytic Oxygen Removal

A significant fraction of the oxygen may be removed with the nitrogen in the NRU. However, a separate Oxygen Removal unit operation is included in this preliminary evaluation. Catalytic combustion of methane and oxygen is expected to reduce the oxygen concentration below the specified concentration of 10 parts per million (ppm) for pipeline natural gas. The scaled subsystem capital cost for this unit operation is estimated to be $280,000 for approximately 2 MMSCFD gas in the product stream after the NRU.

Carbon Dioxide Removal

An amine carbon dioxide (CO_2) removal system is typically used for natural gas and petrochemical processing. This represents a commercial basis for this unit operation. The scaled subsystem capital cost for this unit operation is estimated to be $150,000 for the remaining 2 MMSCFD of product gas. Membranes or Engelhard's Molecular Gate (a specialized PSA adsorbent) offer alternative techniques but the installed costs are comparable to amine systems.

Cost Comparison

Based upon the Velocys Technology NRU achieving the operational and cost targets, the resulting methane upgrading system should have a distinct cost advantage. The graph in Figure 13 shows the results of a preliminary system cost study and compares the results with a case from the EPA study (benchmark).

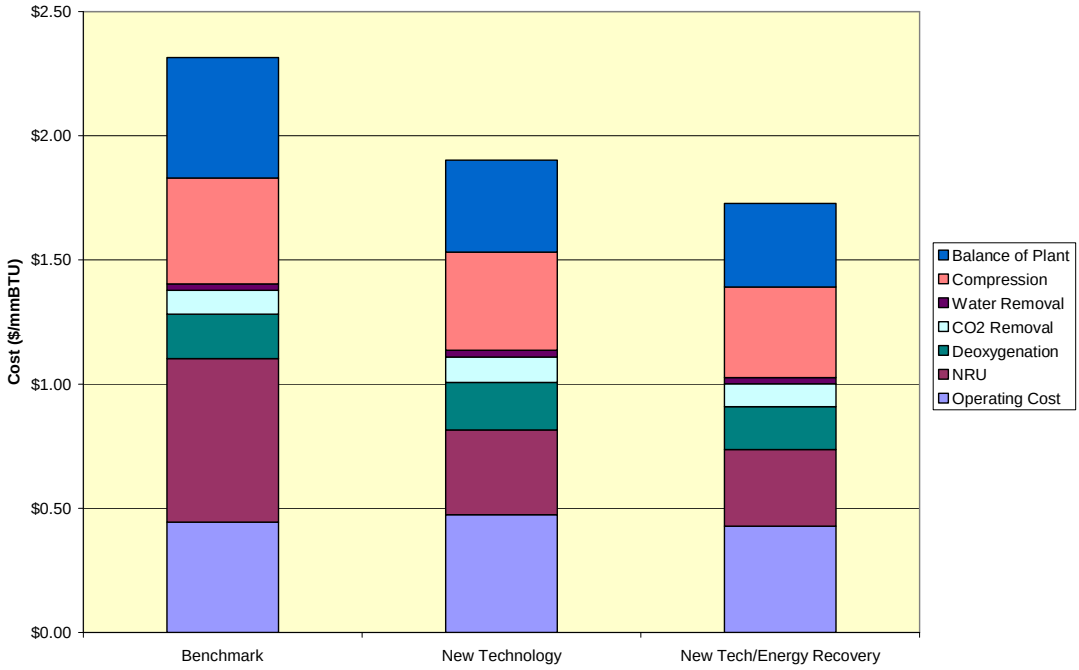

Figure 13. Preliminary system cost comparison (3 MMSCFD basis).

Nitrogen Rejection Unit

This section of the system study focuses on the final stated objective: summary metrics of product recovery and thermal efficiency. To determine these key parameters a mathematical model was developed to simulate a multi-stage nitrogen recovery unit (NRU). A series of runs were performed on the model with the following objectives:

- To determine key parameters governing energy requirements for a Nitrogen Removal Unit (NRU).
- To design system to deliver required energy to NRU.

Figure 14 shows the schematic of the model NRU system. The theoretical NRU has channels housing adsorbent material adjacent to heat exchange channels. The heat exchange channels are used to swing the bed temperature between the adsorbing and desorbing temperature state. The feed gas enters the low temperature adsorbent section of the NRU to preferentially adsorb methane. A nitrogen rich exhaust stream, labeled 'tail gas', is rejected out of the unit prior to breakthrough of the product methane. After the adsorber unit is filled to capacity with methane, the device is heated to desorb methane. In order to flush removed methane out of the box, a small quantity of "flush gas" may be flowed, but this may not be necessary. The methane released from the desorption cycle may become the feed for the next stage or collected as product if sufficient purity is attained.

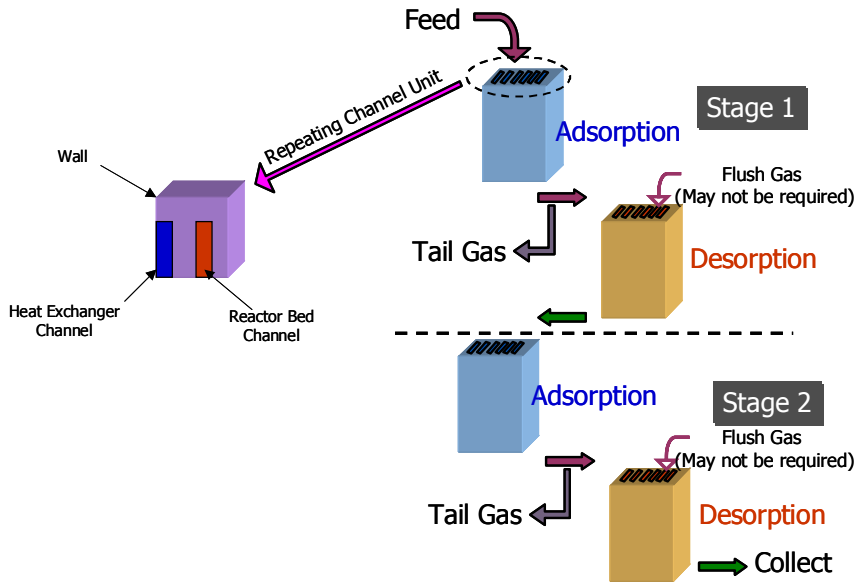

Figure 14. Nitrogen Rejection Unit schematic.

The inputs to the computational NRU model are:

- Channel dimensions
- Adsorbent Characteristics
- Inlet Feed gas composition and outlet methane flow rate
- Adsorption/desorption temperature and cycle time
- Construction material of box

By varying the following inputs, two potential NRU design concepts were developed. The first, called 'early entry,' requires more energy to swing the temperature of the adsorbent bed but is expected to be a more straight-forward development effort. The second, which uses an engineered form of the adsorbent material, is expected to have a longer development effort, but will result in improved methane recovery and reduced energy consumption. The specifics of each concept are presented in Table 12.

	Early Entry	**Engineered Form**
Material of Construction	Stainless Steel	Porous Carbon Engineered Form/Stainless Steel Composite
Adsorbent Form	Powdered	
Cycle Time	1 to 5 seconds	1 to 3 seconds
Energy Requirement	~1.65 megawatts (MW)	~400 kilowatts
Methane Recovery	>80%	>95%

Table 12. NRU process performance targets and anticipated performance

Heating and Cooling System for NRU

Integral pieces of the NRU are the heating and cooling systems that permit the rapid temperature swings. A schematic of these systems is shown below in Figure 15.

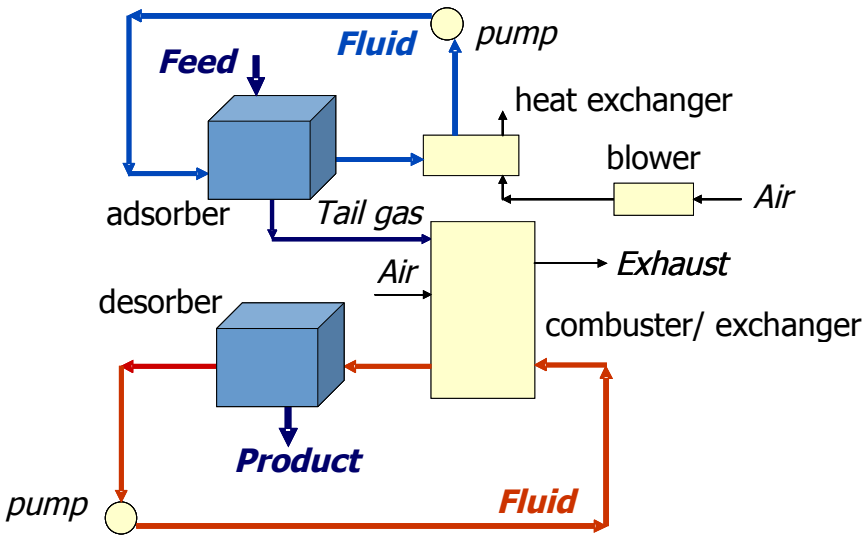

Figure 15. NRU Heating and Cooling Systems.

The system is fueled by methane in the tail gas, which is combusted with air to provide heat to desorb the bed. An efficiency of 70% was assumed for heat transfer from combusted gas to the nitrogen rejection unit. Achieving this energy efficiency may require the use of efficient microchannel exchangers. The heat from the combusted gases is transferred to a circulating fluid which flows through the NRU system to provide heat to the desorption cycle.

Other sources of heat, such as inter-stage and/or after coolers on the compression equipment, may also be used to affect the thermal swing. If these other sources can be tapped, then a further reduction in the amount of tail gas methane required for the desorption cycle is possible.

For the adsorption cycle, heat is removed from the NRU system by a cooling circuit. A cooling fluid removes heat from the NRU system. In a closed-loop process, heat is rejected to ambient from the cooling fluid prior to returning into the adsorber unit.

Conclusions

A system design was completed for upgrading sub-quality methane to natural gas pipeline quality. The Velocys NRU is anticipated to generate at least 96% methane purity and recover at least 80% of the methane. A next generation design is also being investigated to increase the methane recovery to 95%.

Task 2.2. Conceptual Component Design

The adsorber and the desorber units were designed for a total capacity of 3 MMSCFD of gas fed to the NRU system. Below are the assumptions used for designing the adsorber and desorber unit:

Adsorbent characteristics for the selected granular carbon:

1. Differential capacity of CH_4 = 0.01 gram (gm)/gm
2. Differential capacity of N_2 = 0.0003 gm/gm
3. Particle size = 315 micrometers
4. Heat Capacity = 1,260 Joule/kilogram/°C
5. Bed Density = 540 kg/cubic meter
6. Void fraction = 0.4

Feed gas design basis:

1. Molar composition: 70% CH_4, 30% N_2 at inlet
2. Adsorber temperature = 40°C
3. Desorber temperature = 60°C
4. Process pressure = 100 psig
5. The desorbed gas is removed from the channels by pressure differential

The adsorber and the desorber were designed to withstand a total absolute pressure of 150 psig and differential pressure of 70 psi. The material of construction is Stainless Steel 304L. Figure 16 shows a representative picture of the adsorber and desorber unit.

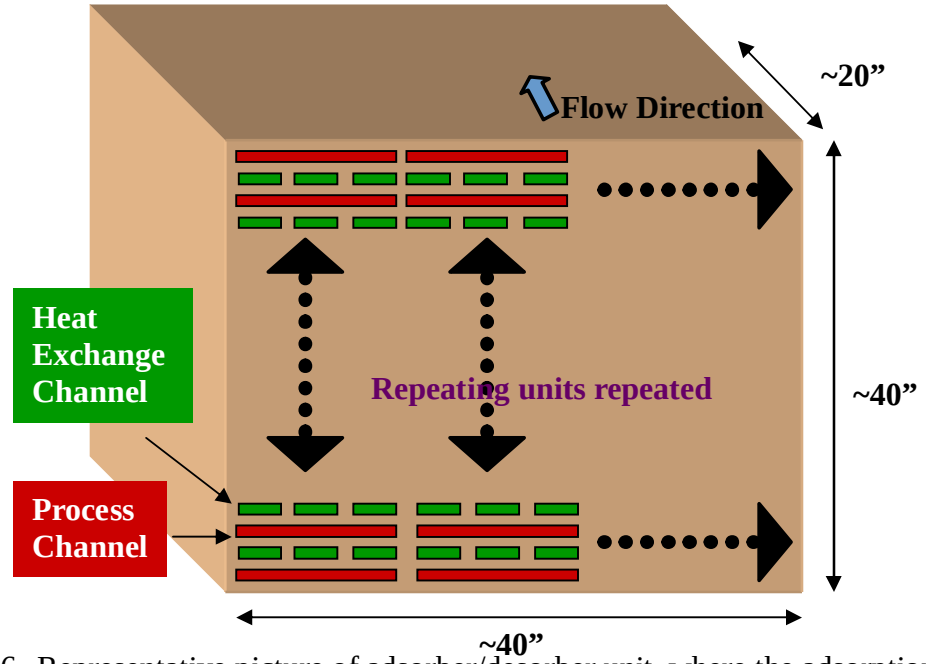

Figure 16. Representative picture of adsorber/desorber unit, where the adsorption channels are the longer slots interleaved between heat exchange microchannels.

The picture shown in Figure 16 is illustrative and is not to scale. The overall dimension of the unit is ~40" (width) x ~40" (height) x ~20" (flow length). The unit has parallel process and heat exchange channels. Both the process and heat exchange channels have a microchannel gap on the order of 1000 microns. The process channel contains an adsorbent bed to adsorb methane from the process gas. The heat exchange channels heats and cools on adjacent sides of the adsorbent channel to adsorb and desorb methane.

The design basis feed gas is a mixture of 70% methane and 30% nitrogen. The adsorber operating temperature is approximately 40°C, while the desorber operating temperature is approximately 60°C.

The design performance of the adorber/desorber unit is

1. Purity of the product = 96%
2. Recovery of methane = 90%
3. Cycle time = 4 seconds
4. Number of stages required = 1
5. Energy required to swing the temperature of the unit = 1.65 megawatts (MW)

The energy requirement of the box to swing temperature is obtained by combustion of the tail gas (assuming 70% energy transfer efficiency).

Water is used as coolant for heat exchange channels to provide and remove heat from the box for desorption and adsorption, respectively. The total flow rate of water required is roughly 20 kg/second. A schematic of heating and cooling system is shown in Figure 15.

Task 3. Cost and Feasibility Assessment

Objective

The goals of the Cost and Feasibility Assessment task were as follows

- Estimate capital and operating costs of an ultra-fast TSA NRU
- Assess the reduction of greenhouse gas emissions

Feasibility Study Variables

To provide a basis for the system study, variables were fixed and conventions adopted for the following

- Adsorbent
- Valves
- Component
- System

The basis for this study was the same used in conceptual component design (Task 2.2). The capital cost estimate was based on the design derived in Task 2 of the project. The microchannel component of the ultra-fast TSA system was determined using in-house models in conjunction with Velocys expertise in the field. Accompanying equipment costs were based on information from vendors and factored estimates. Operating costs included the mineral value of the fuel consumed in the system, maintenance, and other personnel costs.

Potential Impact on Greenhouse Gas Abatement

The possible greenhouse gas (GHG) emission reduction was measured by installing an ultra-fast TSA NRU system using the global warming potential (GWP) methodology. This technique evaluates the relative atmospheric warming potential of a variety of greenhouse gases relative to the potential of carbon dioxide, the most abundant GHG. The time horizon used for these calculations was 100 years, which gives methane a GWP factor of 21.

The same basis used for the design and cost study was used to calculate the GWP advantage for a coal-mine methane project using the Velocys NRU. The results of these calculations are shown in Table 13 below. Assuming that 600 MMSCFD of gas upgrading facilities are built each year in the five years following the development program, which is projected to be complete by 2007, approximately 3 billion SCFD will be on-line in 2012. The resulting greenhouse gas abatement would be equivalent to decreasing carbon dioxide emissions by 148 million metric tons per year, or approximately 2% of the U.S. total.

Scenario	Vented Gas	Gas Utilization
Inlet gas flow rate	3 MMSCFD	3 MMSCFD
CH_4 Released to Environment (kg/year)	1.42×10^7	0
CO_2 Released to Environment (kg/year)	2.24×10^6	6.55×10^6
Global Warming Potential (equivalent kg CO_2/year)	3.01×10^8	6.55×10^6
Savings(equivalent kg CO_2/yr and metric tons/year)		2.95×10^8 (148,000)

Table 13. Greenhouse gas emission comparison

Adsorbent Feasibility

A dynamic numerical model was developed to study the impact of design variables on the time required to thermally swing the adsorbent unit. For the selected adsorbent and channel geometry, the predicted cyclic thermal profile in the adsorbent bed is shown as a function of the heating and cooling medium flow rate. The selected system cycle time of 4 seconds requires a water flow rate of 0.5 meters per second in adjacent microchannels.

Measured capacity, as previously reported (10 milligram [mg]/gm methane and < 1 mg/gm N2), appears feasible for obtaining the projected process performance.

Adsorbent kinetics or time for equilibration within the granular carbon also appears feasible. The selected particle size is on average 315 microns in diameter. The time for gas-phase diffusion from the surface to the interior active sites is calculated to be on the order of 1 millisecond, while the gas spends more than a second in the adsorbent channel. The resulting time difference of two or three orders of magnitude suggests the adsorbate molecules should have sufficient time for equilibration within the adsorbent particle.

Diffusion time is estimated as the square of the longest diffusion distance divided by the diffusivity. The diffusivity for this mixture at temperature and pressure is estimated to be roughly 0.23 square centimeters per second using the Wilke equation. The longest transport distance is the particle radius, or 0.0158 centimeter. The resulting effective time for diffusion within a particle is estimated to be 1.1 milliseconds.

Valve Selection

To optimize the benefits of the microchannel-based TSA NRU, it is desirable for the various process valves to fully stroke in milliseconds, every few seconds. An extensive effort was made to identify valves that 1) are capable of rapidly opening and closing, 2) have high number of cycles between failures, and 3) are inexpensive. Many styles of valves were examined and many potential vendors contacted. Table 14 contains a summary of pertinent data from a number of manufacturers. Unquestionably, the proposed application is a severe service for any valve, and this was validated by many manufacturers during the search.

High-performance butterfly valves (HPBVs) appear to be best suited for the application, based on a composite assessment of actuation speed, longevity, and cost. HPBVs are made by a host of manufacturers. Specific recommendations for optimizing the TSA NRU design were based on the DuZurik HPVB with its PowerRac® actuator. DuZurik has placed valves in severe cyclic applications and was able to provide more performance and life-cycle information for its HPBV and actuator than other vendors. There are valves that can cycle faster, but these are generally very expensive specialty valves and/or they are not made to cycle every few seconds.

The typical failure sequence for the HPBV is the seat, packing, and then actuator seals (rebuild). Except for tightening the packing gland, the valve must be removed from service for repair. None of these expected repairs is particularly expensive. The downtime associated with the repair is the more significant cost.

Valve Type	Valve Provider	Actuator Type	Actuator Provider	Cost X 1000	Stoke Time	Anticipated Life Cycle
Solenoid	Snap-Tite	Solenoid	Snap-Tite	3"-$1.7	200-500 ms	20,000
Pinch	RF Valve	Solenoid	Unknown	Recmend. 2"-for Appl. 2"-$1.3 4"-$1.3 6"-$1.6	< 1 sec	> 500,000
HPVB	Fisher	Rack & Pinion	Bettis	4"-$1.4 6"-$1.8	~ 1 sec	not published
HPVB	DuZurik	Piston actuated Rack & Pinion	DuZurik	4"-$2.5 6"-$3.0	320 ms	>1,000,000 valve seat > 5,000,000 actuator Rep has experience with high-cycle apps.
Fuel Shut off in Gas Turbine	Whittaker Controls	Assume Solenoid	Unknown	2" $9.0 in quantities> 100	100 ms (C) 200-330 (O)	Same as Woodward
GSOV - Spool	Woodward	Solenoid	Unknown	2"-$12.0	85 ms @ 600 psi (C) 300ms @ 100 psi (O)	20,000
Fuel - Spool	Woodward	Solenoid	Unknown	No Quote	90 ms (C) 1 sec (O)	not published
Globe	Valtek	Linear	Valtek	6"-$10.0	300ms	>1,000,000
¼ Turn		Rotary	Schafer	No Quote	250 ms	2,000

Table 14. Summary of fast cycling valve data

For the microchannel-based TSA NRU, a seat failure (minor leakage) should not be a major issue since a small leakage through the seat would have a small effect on unit performance. Secondary shutdown valves for emergency isolation on the feed and product streams may be required to operate the system safely. Assuming that tight shutoff cannot be guaranteed, seat seal life, relatively speaking, will be short. An actuator failure, on the other hand, could very easily force the system to shut down for maintenance. Consequently, the mean time between actuator failures becomes the basis for a preventative maintenance schedule. To minimize system downtime, valve seats and packing should be replaced during the actuator's planned maintenance schedule.

It is reasonable to assume that the actuators could be rebuilt on a biannual preventive maintenance schedule to ensure reliable operation. This is the recommended basis for design of the Velocys microchannel-based TSA NRU

Component Cost and Manufacturability

For the NRU design concept, the manufacturing assessment indicates a cost to produce of between $30,000 and $55,000. These estimates assume the material of construction will be 304L stainless steel. Also assumed is a production capacity of 500 units per year, which would be sufficient to process approximately 600 MMSCFD.

At the production level of 500 units per year, much of the manufacturing is performed by subcontractors, and the associated costs included in the processing line item will be further reduced. As the production level increases, subcontract costs could be further reduced – thus reducing the overall the cost to produce the microchannel adsorber units.

In regard to manufacturability of the NRU design, the proposed design conforms to Velocys standards for feature size formation, tolerance allowances for subsystems and assembly, and metal joining requirements for either diffusion bonding or metal brazing. Loading and refurbishment of the granular adsorbent also conforms to Velocys standards for granular catalyst systems, and no further challenge is identified at this time.

System Design and Cost Estimate

Two NRU sub-systems were evaluated: a stand-alone case and an integrated case that shares chilled water with the upstream dehydration sub-system and heating with an adjacent power cogeneration plant. Significant cost, energy, and environmental advantages may result from an integrated system.

A process flow diagram for the stand-alone NRU subsystem is presented in Appendix III and was the basis for the heat and mass balance calculations and cost estimating. The feed stream was compressed and dehydrated before entering the NRU subsystem. The NRU cycles between adsorbing and desorbing the methane (CH_4). The process design and cost estimate treats the NRU sub-system as a continuous-flow, steady-state device although it cycles between adsorbing and desorbing two reactors/vessels.

Cooling fluid reduces the process temperature to 40°C during the adsorption cycle. Unrecovered CH_4, CO_2, N_2 and O_2 exit as rejected tail gas during this cycle. The valve sequence stops cooling fluid flow and feed to the first box and starts heating fluid flow for the desorption cycle to produce NRU product at 60°C. Table 15 lists the valve positions. For simplicity sake, the cooling and heating fluids were assumed to be water.

Stream	Valve #	Adsorber (Desorber) #1	Desorber (Adsorber) #2
Feed	1	Open	Closed
Product	2	Closed	Open
Tail Gas	3	Open	Closed
Cooling Fluid	4	Open	Closed
Heating Fluid	5	Closed	Open

Table 15. Valve positions

Surge tanks provide buffer capacity to stabilize flows during the valve cycling. NRU product proceeds to the O_2 and CO_2 removal sub-systems for further processing and purification.

Methane recovery is 90% for the NRU. Other constituents, such as CO_2, N_2 and O_2, are separated at specific separation factors that require experimental validation. The tail gas is used as fuel to a conventional packaged boiler (hot water heater) for the heating fluid and heat recovery/integration with the overall system. The specific combustor design will establish the quantity of excess air that may be needed and the resulting combustion exhaust temperature.

Table 16 summarizes the equipment list, cost, and duty specifications for the stand-alone NRU sub-system. The costs of purchased equipment were estimated from quotes in project files for similar sizes and types of equipment. The sub-total, Purchased Equipment Cost, was used as the basis for a factored estimate of the shop-assembled sub-system that could be shipped to the site for field installation. The Shop Fabrication Cost Estimate subtotal may be compared to the NRU costs reported in the 1997 EPA report described under Experimental, Task 2.1.

After a 275% factor is applied to the raw equipment costs, the resulting NRU system cost is $911,000, approximately 50% higher than the target of $600,000. These cost factors, which include allowances for piping, instrumentation, engineering, and others, have been reviewed by out industry consultant, Joe D'Amico. He felt that, overall, the factors may be conservative, but are appropriate for this level of cost study.

Mr. D'Amico also provided guidance on ways to reduce the cost of the NRU. His suggestions centered around integrating the NRU with the other process equipment available at a gas upgrading project site. The result of these discussions was the integrated NRU sub-system shown in Appendix V. The feed stream was compressed and dehydrated before entering the NRU subsystem. NRU product continues to the O_2 and CO_2 removal subsystems, as in the stand-alone case.

In the integrated plant, the cooling fluid for the NRU adsorption cycle is from a chiller that supplies the dehydration subsystem. The cost for incremental capacity of chilled water is advantageous rather than buying two independent chillers. Operating the cooling fluid at 5°C (40°F) is also favorable for TSA performance.

ID#	Description	Capacity	Size	Cost
D-200	Hot Fluid Surge Drum	2000 gal	5-ft dia x 15 ft	11,500
Unit Op #10	Velocys TSA NRU			50,000
Unit Op #13	Velocys TSA NRU			50,000
Valve1, A&B	Feed Inlet to TSA			3600
Valve2, A&B	Product out of TSA			3600
Valve3, A&B	Tail Gas out of TSA			3600
Valve4, A&B	Cold Fluid out of TSA			4000
Valve5, A&B	Hot Fluid out of TSA			4000
P-101	Cold Fluid Pump	1190 gpm		7501
F-103	Cold Fluid Filter			5001
E-107	Cold Fluid Exchanger	5.5 MM Btu/hr		22,001
P-201	Hot Fluid Pump	1190 gpm		7501
F-203	Hot Fluid Filter			5001
E-204	Hot Fluid Heat Exchanger	5.5 MM Btu/hr		
F-301	Inlet Air Filter			
B-302	Combustion Air Blower			
E-303	Air Preheater	1.9 MM Btu/hr		20,001
Comb-310	Combustor			110,001
Subtotal (Purchased Equipment Cost)				330,937
Shop Fabrication Cost Estimate (ex works)				
Cost Element		Factor (x PEC)		Cost, $
Piping		50%		166,000
Instrumentation and Control		20%		67,000
Electrical		10%		34,000
Skid/Support/Assembly		25%		83,000
Insulation/Paint/Freight		10%		34,000
Engineering/Overhead		30%		100,000
Contingency/Profit		30%		100,000
Total		275%		911,000
Target				600,000
EPA Report (Cost range for Commercial NRU Subsytems)			1,030,000	1,390,000

Table 16. Stand-alone NRU equipment list and costs

Tail gas from the NRU has a heating value of approximately 230 Btu/SCF and may be mixed with feed gas (70% CH_4, heating value of 700 Btu/SCF) as fuel to an engine-driven generator. On-site generation of electricity can be cost-effective with low-cost fuels as a site-specific

evaluation. The estimated power requirement for a 3 MMSCFD gob gas upgrade system is estimated to be 1,200 horsepower to operate compressors, chillers, pumps, and auxiliary equipment. The exhaust from an engine-driven generator would heat water to 80°C (176°F) as the NRU heating fluid in exchanger E-204. This integration eliminates the combustor and associated equipment from the stand-alone case.

The NRU capital cost for the integrated case is lowered to $584,000, slightly below the $600,000 target. Coal mines are typically in remote locations with limited available electrical power. Many remote locations justify on-site power generation, especially with low-cost fuel, rather than paying for power distribution and the associated electrical operating costs. Carbon dioxide reduction credits may apply since this represents a more energy efficient and environmentally acceptable solution than venting the tail gas as is practiced for some NRU technologies.

Other advantages of the TSA sub-system include

- Less compressor power is required because the NRU product methane exits at essentially the same pressure as the NRU feed.
- Methane in the tail gas is used as fuel rather than vented to atmosphere.
- Flow is in one direction, which avoids the dynamic stability issues of reverse flow as practiced by some competing technologies.

Conclusions

Results of the cost and feasibility analyses indicate the following:

1. The greenhouse gas abatement potential of this technology is significant, potentially reducing U.S. emissions by up to 2%
2. Heating and cooling cycles were modeled, which validated the design assumption of a 3-second cycle time
3. Appropriate valves to handle fast cycling have been identified
4. Cost targets for a “stand-alone” NRU are likely difficult to reach
5. However, integrating the NRU with the rest of the upgrading process system offers the opportunity to reduce the capital cost below the $600,000 target

Task 4. Bench-Scale Technology Demonstration

Objective

The goal of this task is to demonstrate methane purification in a mixed nitrogen stream at ultra-fast cycle times in MPT-based TSA hardware.

Demonstration Variables

The demonstration evaluated a range of process variables:

- Cycle Times - 4 seconds to 10 seconds
- Degrees of Thermal Swing - 10°C to 40°C
- Methane Feed Compositions – 70% methane with balance nitrogen

Demonstration Hardware

The demonstration was completed using a cylindrical device. A rectangular device was also fabricated but not yet evaluated.

Rectangular Test Device Design

The device consists of a central process microchannel with heat exchange channels on both sides (Figure 17). Thin stainless steel walls separate the process channel from the heat exchange channels to minimize thermal mass and conduction path. Operating pressure in the process channel is higher than the heat exchange channel pressure. The heat exchange channel is divided into several smaller channels to provide ribs to support the wall and reduce stress due to the pressure differential. T-shaped longitudinal supports form the side walls of the process channel and determine the channel height and length. The heat exchange channels are machined into aluminum plates with connecting holes to individual manifolds.

The longitudinal supports, walls, and heat exchange plates are joined. The openings in the T-shaped longitudinal supports and the angled grooves in the heat exchange plates provide sufficient joint area. An additional C-shaped member is joined along the length to provide additional support and reduce joint stresses.

Process manifolds fit over the ends of the bonded plate and C-channel assembly. Heat exchange manifolds are attached to the heat exchange plates. Flow through the heat exchange manifold is in a Z-configuration on both sides. Flow on one side is independent of flow on the other side. Tubing connections are used to the system valves.

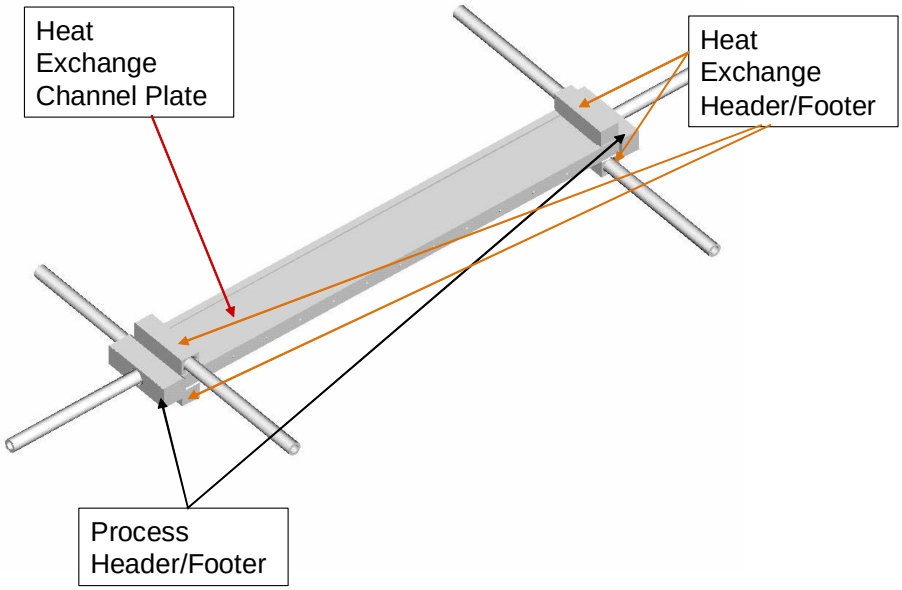

Figure 17. Fully Assembled Bench-scale Device

Cylindrical Single Channel Test Device

A simplified cylindrical single-channel test device (see Figure 18) was designed, fabricated and tested to demonstrate the feasibility of the ultra-fast thermal swing approach. The stainless steel cylindrical test device included several key features, including the capability of including three 0.5 mm diameter thermocouples in the bed along the axis of flow, a 1.4 mm thick (19 cm long) packed bed, a 0.15 mm thick heat transfer wall, and a single heat exchange channel which alternated between heating and cooling fluid during thermal cycling. The cooling fluid flow ran vertically downward during the adsorption portion of the cycle and then the heating fluid was run in the opposite direction (vertically upward) through the same channel during the desorption portion of the cycle. A 150 mesh stainless steel retaining screen was used at the annular packed bed outlet. Vespule-graphite ferrules with appropriately sized drilled holes and stainless-steel swagelock fittings were used to seal the feed-through for the inner heat exchange tube and to seal three 12-18 inch 0.5 mm diameter type K thermocouples fed-through above the top of the bed. Inlet and outlet process lines were reduced to 1.8 mm ID at the inlet and outlet to minimize dead volume.

The adsorbent was reduced to the desired particle size range by crushing and grinding the as-received activated carbon with a mortar and pestle, then hand-sieving between US standard 80 and 100 mesh sieves and regrinding and re-sieving the oversized material after each sieving step.

In one set of tests, the cylindrical test device was tested over a range of cycle times (3-15 seconds), heat exchange fluid flow rates (80-240 ml/min) and heat exchange fluid temperatures (70-90°C hot and 30-10°C cold.) Although most tests were performed at 100 psig process pressure, tests at 80 and 120 psig were also included. Isothermal tests were also performed to compare the measured CH_4 adsorption isothermal capacity with previously measured values. In all, about 2100 full thermal cycles were performed during this phase of testing and no physical degradation of the adsorbent was observed.

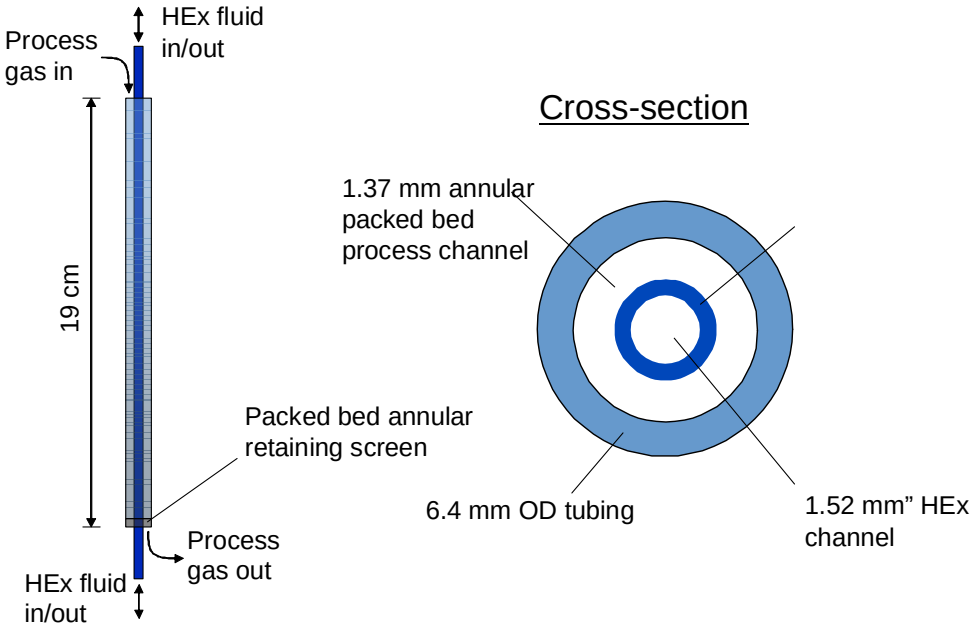

Figure 18. Schematic of the cylindrical ultra-fast thermal swing adsorption single channel nitrogen rejection unit test device.

Experimental Set-up for the Bench-scale Demonstration

A simplified test setup for the ultra-fast thermal swing adsorption single channel nitrogen rejection unit (NRU) test device was used in initial testing to demonstrate the feasibility of ultra-fast thermal swing adsorption and estimate the adsorbent differential methane capacity under ultra-fast thermal swing conditions. To simplify the analysis while accomplishing these purposes, pure methane metered by Brooks mass flow controller was used as the process gas in the simplified setup shown in Figure 19.

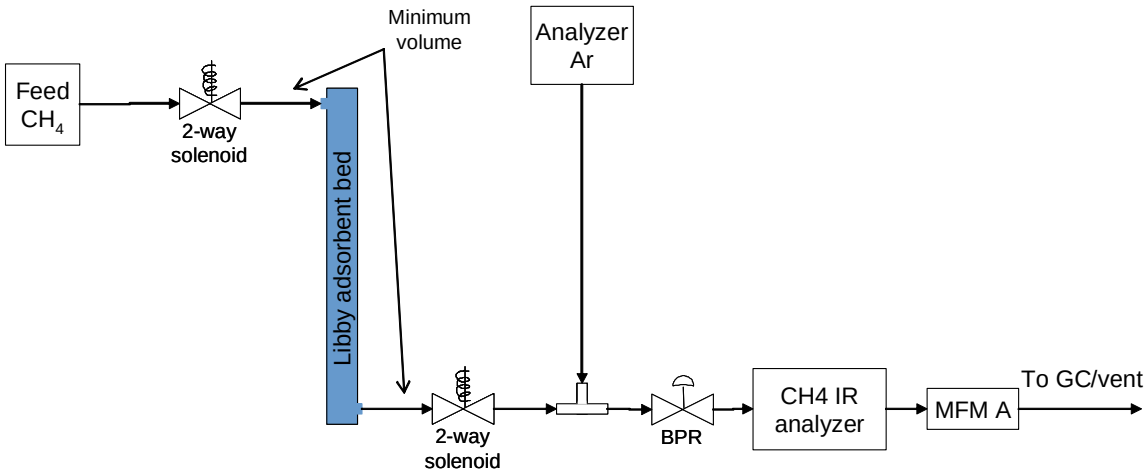

Figure 19. Simplified experimental test setup for the ultra-fast thermal swing adsorption single channel nitrogen rejection unit test device (heat exchange fluid flow not shown.)

A modified testing configuration (see Figure 20) and procedure were used to estimate the purity achieved in the product of the ultra-fast thermal swing adsorption tests, while eliminating the diluting effect of dead volume before and after the adsorbent bed. The test setup in Figure 20 differs from that shown in Figure 19 in that all the gases (adsorption or sweep gases which bypass the bed, product gas, and tail gas) are eventually combined and sent to a common backpressure regulator. This allowed operation with a very steady back-pressure, since the total flow through the back-pressure regulator was constant at any given time. In order to sample the product gas line, the product was withdrawn from a point well-upstream of the point of product/tail gas mixing and a separate Ar gas flow was provided downstream of the sampling point to allow analysis of the entire product stream, diluted with some Ar. The test setup was designed to allow a single pulse of product to be sent to the gas analyzer system, where the capacity and product purity could be analyzed. The procedure for estimating product purity was as follows:

1) The bed and product lines were swept out with Ar gas until no more CH_4 was detected in the product line while swinging the bed between ~40 and 60°C (10 second half-cycle time).
2) Then the bed was then saturated with a mixture of 70% CH_4 / 30% N_2 with the bed still swinging between 40 and 60°C (10 second half-cycle time), sending the bed outlet stream to the tailgas line,
3) Next, the bed thermally cycling was stopped and the bed held at ~40°C (cold heat exchange fluid continued to flow) while flushing the bed with 450 sccm Ar for 4, 5, or 6 seconds (depending on desired flush time), again sending the bed outlet stream to the tailgas line.
4) Finally, while continuing to flush with 450 sccm Ar, the bed outlet stream was sent to the pre-flushed product line and the bed temperature rapidly raised to 60°C (240 ml/min hot fluid continued to flow).

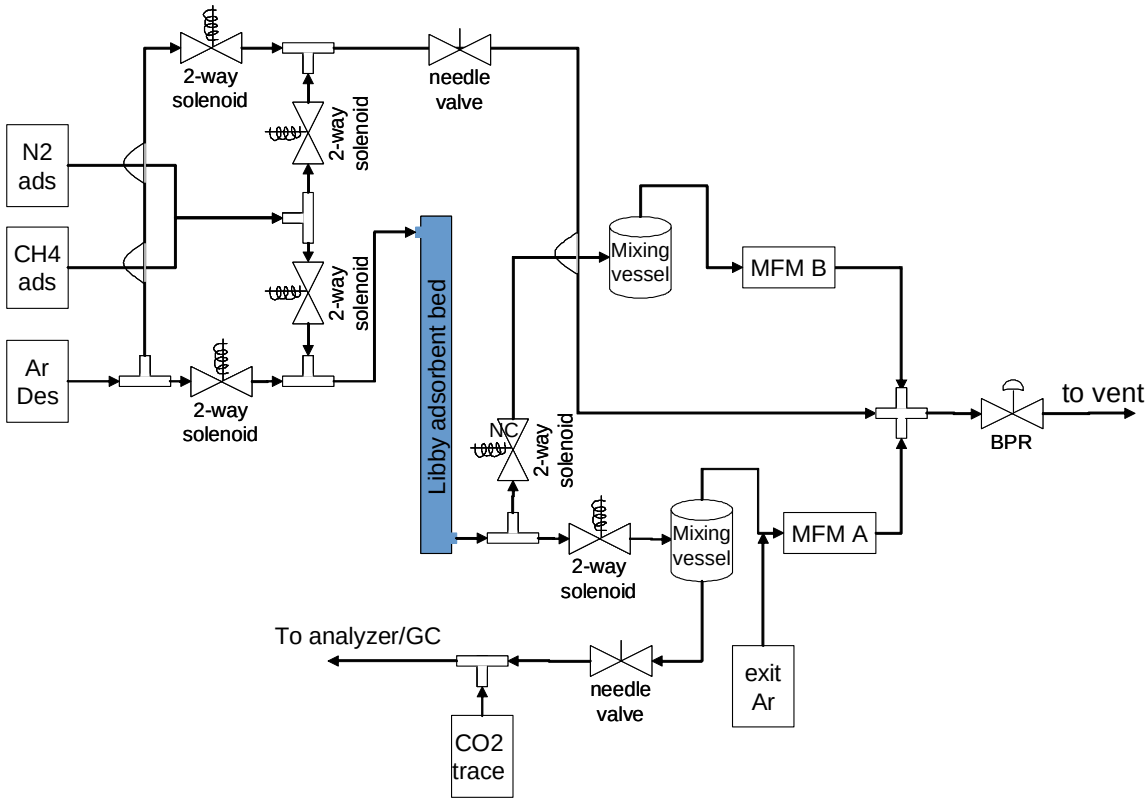

Figure 20. Simplified experimental test setup for the ultra-fast thermal swing adsorption single channel nitrogen rejection unit test device product purity testing (heat exchange fluid flow not shown).

The product stream was then analyzed. By integrating the CH_4 outlet flow over time (CH_4 analyzer), the CH_4 capacity can be estimated. By analyzing the CH_4:N_2 ratio (gas chromatograph), the methane content of the sorbed bed gases was estimated.

For both process gas configurations, the heat exchange configuration shown in Figure 21 was used. In this configuration, fluid (a propylene glycol/water mixture) was first cooled by a chiller, and then either delivered to the device (during the cooling portion of the cycle) or sent to an in-line microchannel electric heater where it was heated to the desired inlet hot temperature before being sent to the device. The change in direction of the heat exchange fluid was accomplished by opening or closing the appropriate combination of valves. For example, in Figure 21, when solenoid valves SOL 3-14 and SOL 3-16 were open and SOL 3-15 and SOL 3-18 were closed, the heat exchange fluid was heated by the in-line heater and flowed upwardly through the device. Then in the cooling portion of the cycle all the valve positions were changed simultaneously and the chilled fluid flowed downwardly through the device. Because the test device temperature changed quickly (on the order of seconds), the hot and cold streams remained nearly isothermal in the tubing of the test setup external to the device during the portion of the cycle in which they remain stagnant.

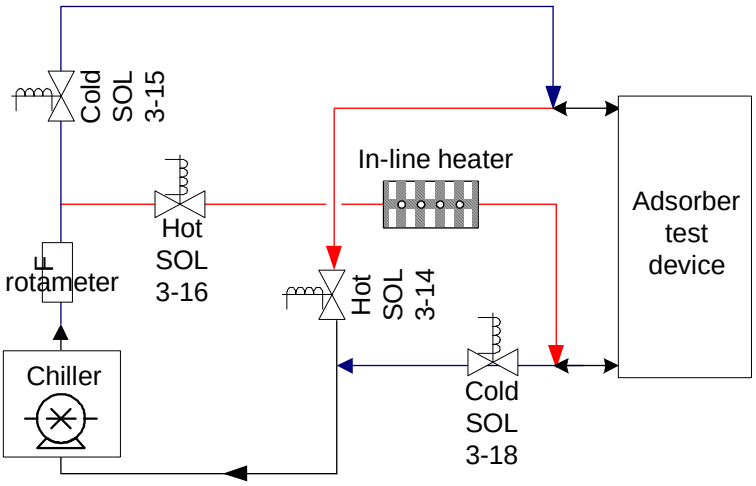

Figure 21. Experimental heat exchange fluid flow diagram for the single heat transfer fluid configuration used with the cylindrical ultra-fast thermal swing adsorption single channel nitrogen rejection unit test device (process flow not shown).

In this embodiment, a single heat transfer fluid is used for both the hot and cold heat exchange stream flows. In this approach, the fluid is either routed through a hot loop or a cold loop, alternately, with the one stream's flow being stagnant whenever the other stream is flowing. This has the advantage of a simplified test setup, since redundant reservoir, pump, and metering systems are not required. This arrangement is particularly desirable when adsorbers are not being operated in pairs, since the fluid does not have to be directed elsewhere during part of the cycle.

Results and Discussion

Preliminary testing revealed that the bed packing was disturbed by a strong backflow, causing some of the bed packing to backflush into the inlet lines. Disassembly after testing showed that 30% of the 2.2 grams initially loaded was recovered from the tubing upstream of the bed and only 60% of the initial bed weight loaded was recovered from inside the test device. This led to low apparent differential methane capacity during testing. A retention screen was welded near the inlet to avoid this issue before continuing with testing.

Continued testing revealed that the setup and cylindrical test device with 25% (v/v) industrial diamond were sufficient to obtain the desired thermal swing between 40 and 60°C for a swing time of about 5 seconds (that is, 5 seconds of heating followed by 5 seconds of cooling) for a properly packed adsorbent bed with 240 ml/min heat exchange fluid flow, with 90°C and 10°C hot and cold heat exchange fluid temperatures, respectively.

A plot of the thermal swing response of a typical bed thermocouple reading to cycle time in seconds (x-axis) and temperature difference between hot and cold heat exchange fluids (y-axis) is shown in Figure 22, for a 240 ml/min. heat exchange fluid flow. In Figure 22, the contours labels show the difference between the average maximum and minimum temperature measured at one axial location in the bed during preliminary thermal swing adsorption tests in the

cylindrical test device. Note that the contours in Figure 22 are interpolated based on a quadratic fit of the data from a designed experiment. It can be seen that 20 °C swing in the packed bed can readily be achieved with heat exchange fluid temperature swings of 70-80°C and heat exchange fluid flow rates of 160-240 ml/min.

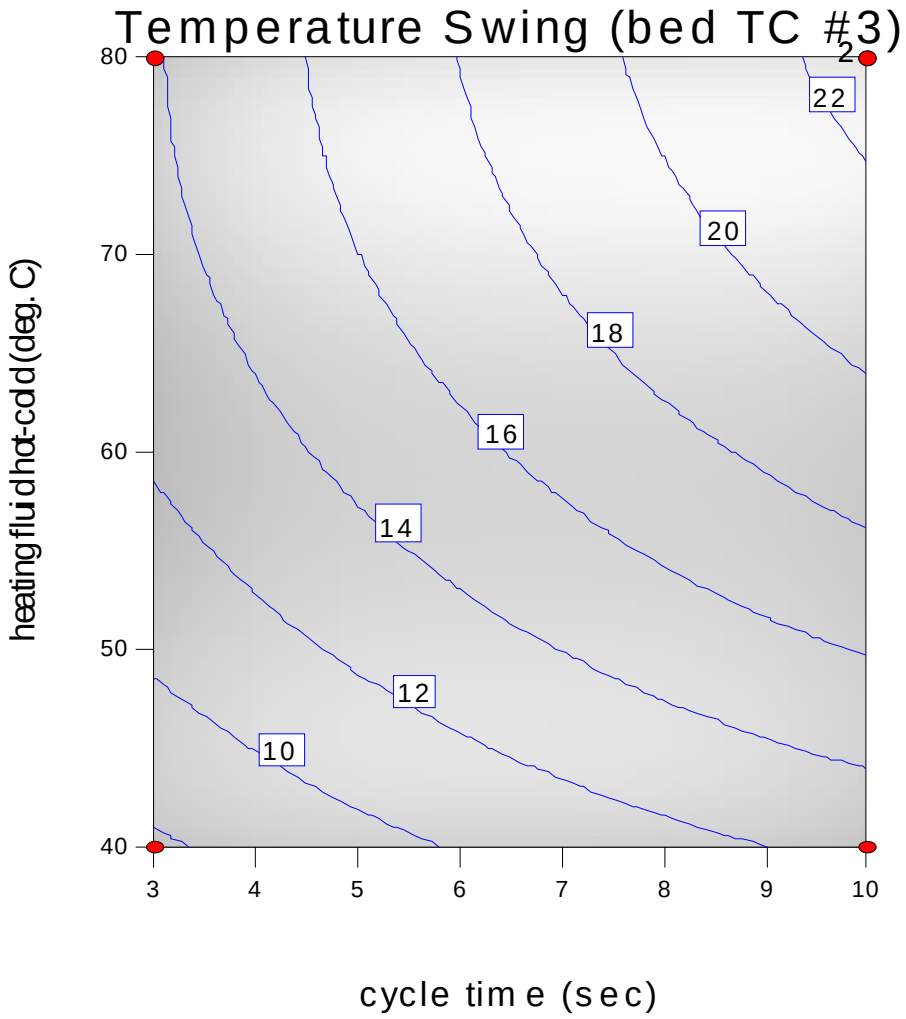

Figure 22. Quadratic fit of bed temperature swing data in cylindrical ultra-fast thermal swing adsorption test device for a heat exchange fluid flow rate of 240 ml/min.

A plot of typical real-time measurements during thermal swing adsorption is shown in Figure 23.

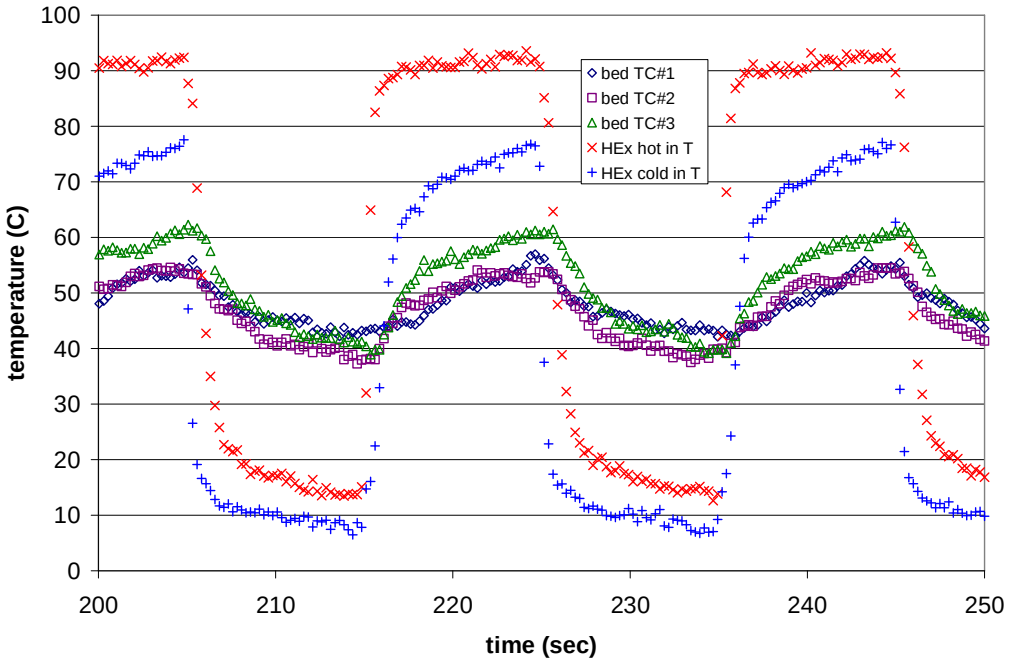

Figure 23. Thermal swing temperature data taken during preliminary ultra-fast thermal swing experiments with pure methane feed, 240 ml/min heat exchange fluid at 90°C hot and 10°C cold with a cycle time of 10 seconds.

The preliminary tests also suggest that the adsorbent bed differential capacity is near the expected value when corrected for lost adsorbent (see Figure 24). Because the bed temperatures in the device take a few seconds to reach a maximum, the differential capacity during thermal swing is less than the full capacity based on isothermal adsorption tests (for example, it appears that for a 5-6 second swing time, about 60% of the isothermal capacity might be expected).

It was found that the isothermal differential capacity at 100 psig between 40 and 60°C (6 mgCH_4/gram adsorbent/20 °C) was about only about 65% of the value measured earlier (9.4 mg CH_4/gram adsorbent). This is in reasonable agreement with the finding upon uninstalling the device, that 30% of the initial bed weight loaded was recovered from the tubing upstream of the bed and only 60% of the initial bed weight loaded was recovered from the test device.

Tests performed at 80 and 120 psig gave thermal swing differential capacities of about 96% and 105% respectively, relative to those measured at 100 psig, all other settings being held constant.

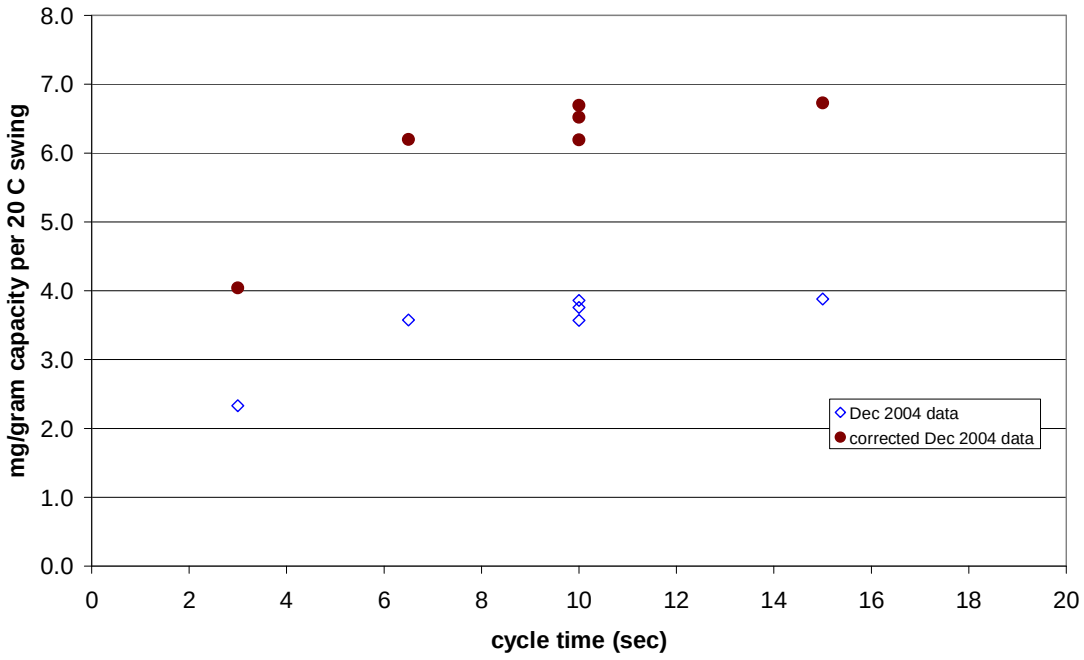

Figure 24. Differential methane capacity (corrected to 20°C temperature swing) from preliminary thermal swing adsorption tests on cylindrical test device. Corrected values assume that only the adsorbent recovered from the device after removal from test setup (60% of initial) was present during testing.

Product purification results:

Flushed dead volume half-cycle tests used to determine product purity for a 10 second half-cycle between 40 and 60°C indicated that the 70% CH_4 feed was enriched to about 92% CH_4 in a single cycle.

Conclusions

The results from the bench-scale demonstration indicate the following:

1. Fast thermal swings (< 10 seconds) can be readily achieved in microchannel hardware
2. No detectable material degradation observed over thousands of cycles
3. Methane purification demonstrated, with purification from 70% to 92% in a single stage

Task 5. Thermal Swing Validation

The project initiated with an investigation into improved adsorbent options for use in the nitrogen rejection application. The evaluation has expanded in breadth to include structured adsorbents, including foams, felts, cloths, and the like.

Important parameters for consideration in evaluating new materials include:

- Thermal conductivity: to swing the bed faster
- Heat capacity: to reduce the amount of energy required to swing the bed
- Capacity: increase the uptake of methane
- Cost: integrate cost competitive and manufacturable structures into microchannel devices

The literature suggested several options for structured carbon adsorbents that may provide an effective thermal conductivity on the order of 1 W/m-K.

A parallel effort was initiated to investigate the impact of a phase change heat transfer fluid on the thermal and adsorption properties versus the use of a convective heat transfer fluid. The modeling study included materials that ranged from 0.18 W/m-K (powder) to a highly effective structured adsorbent (3 W/m-K). The results suggest that a particulate form of the adsorbent could be effective in a thermal swing unit. The next step was to reestablish the baseline performance of capacity and selectivity and understand the impact of feed impurities on performance.

Thermal Model Development with Adsorption Added

Assumptions and References:

Figure 25 illustrates the model domain of the adsorbent bed, for thermal modeling purposes. In order to carry out this preliminary thermal analysis the following assumptions were made:

1. Heat flow was assumed to occur in one spatial dimension (1-D).
2. Material properties for the stainless steel wall as well as adsorbent bed were assumed to be insensitive to temperature variation.
3. Adsorbent bed thermal properties were assumed to be characterized by “effective” properties applied to a uniform homogeneous material.
4. Other heat exchange surfaces within the model were assumed to be adiabatic or perfectly insulated.
5. Methane adsorbed was based on an empirically-derived expression:
   CH_4 / bed mass[mg/g] = $69.34e^{-0.01251T[^\circ c]}$

The derived expression for capacity was based on the data collected in the first part of Phase 1 of the project. This function can be updated after analyzing the new data collected with feed impurities.

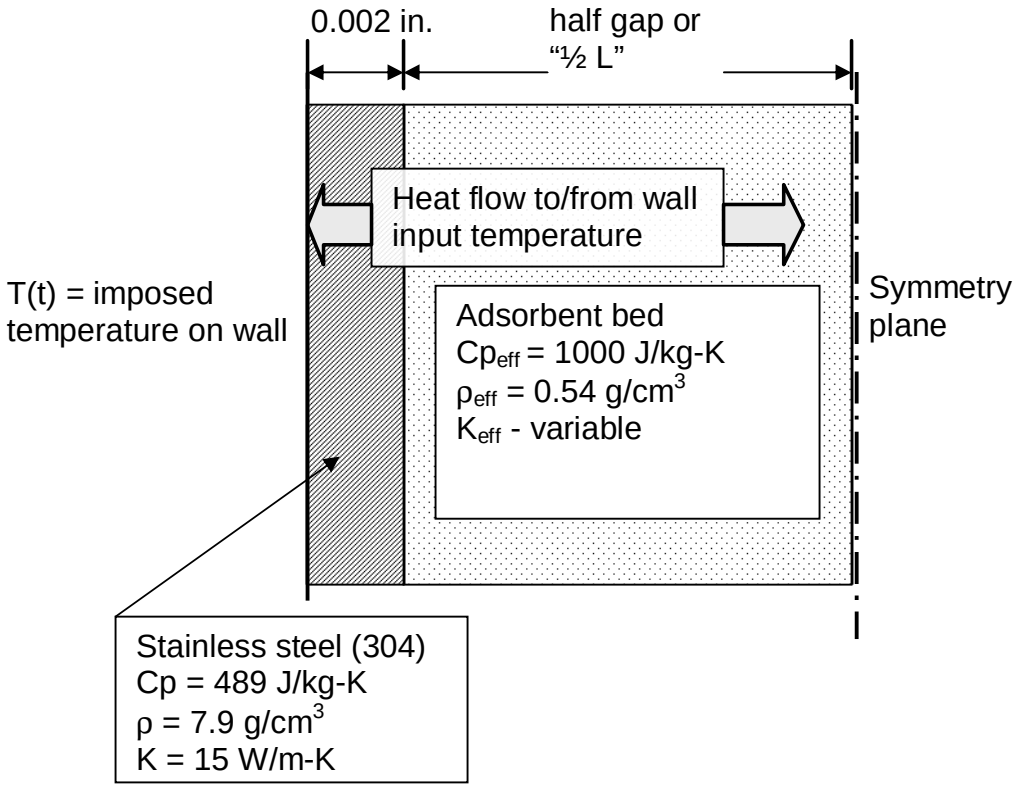

Figure 25. Domain for Adsorbent Model.

Calculation Methodology:

A network analysis model was built using the SINDA/FLUINT simulation tool. Simulation temperatures were coupled to an estimate of methane adsorbed via the following empirical relationship:

$$CH_4 \text{ / bed mass[mg/g]} = 69.34e^{-0.01251T[^\circ c]}$$

For a unity cross-sectional area, bed mass can be expressed as:

$$\text{Bed mass} = \text{gap} \times \text{unit area} \times \rho$$

Therefore the expression for overall CH_4 adsorbed is:

$$CH_4 \text{ adsorbed} = (\text{gap} \times \text{unit area} \times \rho)69.34e^{-0.01251T}$$

The expression for CH_4 adsorbed was incorporated into the SINDA/FLUINT model and used to estimate the methane adsorbed during low temperatures and methane desorbed during high temperatures. The evaluation of this expression was carried out for each computational element within the adsorbent bed. The following numerical expression was solved and summed over the entire adsorbent bed at each time step:

$$CH_4 \text{ adsorbed}(t) = \sum_i [d(gap)_i \cdot Area \cdot \rho \cdot 69.34e^{-0.01251T[c]}]$$

The net methane adsorbed was computed from:

$$\text{Net } CH_4 \text{ adsorbed} = \text{Maximum } CH_4 \text{ adsorbed}(t) - \text{Minimum } CH_4 \text{ adsorbed}(t)$$

Preliminary Evaluations of Thermal Response

For the simulations, the boundary wall temperature was defined on the heat exchange fluid interface. Two transient temperatures (T2 and T3) were calculated within the intervening wall, where T2 was the mid point and T3 and the wall/adsorbent bed interface. Four transient temperatures were calculated within the adsorbent bed at equidistant locations to the bed centerpoint. All calculations were done with a symmetry plane down the center of the adsorbent bed.

Performance Metrics for Thermal Response

Area under the curve ratio or "AUC ratio"

This metric starts with the area under the temperature versus time curve or the integral:

$$\int (T(t)-T_{min})dt \text{ – for one desorption phase, } (\tfrac{1}{2}\tau)$$

evaluated spatially at the adsorbent bed symmetry-plane. The term T_{min} is the minimum temperature or minima for the oscillating adsorbent bed symmetry-plane. This integral is then divided by the corresponding area under the temperature / time curve for the boundary condition square wave, with the T_{min} term equal to the minima for this boundary condition.

Amplitude ratio or "Amp ratio"

This metric is simply a ratio of the temperature extremes delta at the adsorbent symmetry plane divided by the temperature extremes delta for the boundary condition square wave. This relationship can be shown mathematically as:

$$(Tmax - Tmin)_{adsorbent} / (Tmax - Tmin)_{square\ wave}$$

Results and Discussion

The transient thermal model simulated the impact of a phase change heat transfer fluid in the heat transfer channel, where the wall temperature remains constant during each half cycle and only the quality of gas or liquid changes as the adsorbent bed is either cooled or heated.

Variation in thermal conductivity – the adsorbent bed effective thermal conductivity was varied independently from 0.1 W/m-K to 3.0 W/m-K. Results for k_{eff} = 0.1 and k_{eff} = 3.0 can be seen in Figures 26 and 27 for a half channel gap of 0.04" or 1 mm. The half channel gap is defined by the symmetry plane that runs down the center of the adsorbent channel. The black curves correspond to the input temperature boundary condition – the square wave. The colored curves depict material temperatures within the adsorbent bed; location #4 being closest to the wall and location #7 being at the plane of symmetry. Results are shown for a full cycle time of 3 seconds (half cycle for adsorption and half cycle for desorption) between 490 to 500 total elapsed seconds, where the transient thermal behavior had easily reached cyclic steady state.

As the thermal conductivity is increased, the ability for the adsorbent bed to follow the boundary wall temperature is enhanced. At the very lowest thermal conductivity (0.1 W/m-K), the resulting temporal temperature wave within the adsorbent bed exhibited a noticeable phase shift in the maximums and minimums relative to the input wall boundary temperature wave.

Variation in boundary wall temperature amplitude – the boundary wall temperature amplitude was varied such that the wall temperature oscillated from 30° C to 70° C or 20° C to 80° C or 10° C to 90° C. Results for these variations in boundary wall temperatures are shown in Figures 28 and 29. The extent of boundary wall temperature following and the shape of the adsorbent material temperature curves, is similar regardless of temperature amplitude.

Variation in adsorbent bed gap – the adsorbent bed channel gap was varied from 0.04 to 0.1 in. Results for these variations in adsorbent bed gap are shown in Figures 30 and 31. These simulation results demonstrate the expected proportionality between the adsorbent bed width and thermal resistance, i.e. as the gap is reduced, thus having less thermal resistance, the temperature following characteristics increase.

Variation in both adsorbent bed width and adsorbent bed thermal conductivity – a matrix of sensitivity runs were conducted for adsorbent bed gaps of 0.015 in. to 0.08 in. and the thermal conductivity between 0.18 and 1.0 W/m-K. It should be noted that the k value of 0.18 W/m-K is the measured value for a powder carbon adsorbent as reported in the previous quarterly report.

Several simulations produced interesting results that are very promising for the low thermal conductivity powder. See Figures 32 and 33 for typical results. The thermal conductivity was increased from 0.18 to 1.0 – roughly a 5x increase, while the gap was also increased by roughly 5x. Both these changes together did not produce a zero change in thermal conductance, (conductance = $k \cdot A/L$). The thermal behavior of the narrow gap and low thermal conductivity bed this is noticeably different – as a result of the decreased thermal inertia.

Metrics for Thermal Performance of the Adsorbent Bed

Two metrics are defined for comparison of this adsorbent bed temperature following behavior: 1) area under the curve ratio (AUC ratio) and 2) amplitude ratio (Amp ratio). Two variations in adsorbent bed temperature characteristics occur as thermal resistance changes in the bed. The adsorbent bed temperature wave loses the input square-wave appearance, which can be

quantified as a deviation in the area under the curve. Also the temperature amplitude deviates from that input. These two metrics allow for these complex transient characteristics to be quantified as two numbers for comparison purposes. AUC ratio and Amp ratio were computed at the adsorbent bed symmetry plane. Ratios that approach 100% indicate that the adsorbent bed material closely follows the input temperature boundary condition, which is desirable for high adsorbent utilization.

Figure 34 illustrates much of the data, presented as AUC ratio and Amp ratio versus the term: thermal conductivity divided by gap width (k/L). As k/L increases, the AUC ratio and Amp ratio both approach 100%. For designs with k/L values of > 15 [W/m-K / in], the bed temperature amplitude is nearly 100% of that input and the AUC is >80% of the square-wave input. Figure 35 shows the AUC ratio and Amp ratio when only the thermal conductivity is varied. The temperature following behavior correlates well with k/L. Figure 36 shows AUC ratio and Amp ratio for variations in the channel gap width. For this single independent variable change, gap width, thermal response correlates well with k/L. Figure 37 shows thermal performance behavior for changes in both thermal conductivity *and* gap width. This set of data was collected for only low k/L values ($k/L \leq 10$). Notice that no good correlation exists between the k/L values and thermal performance. Figure 37 results illustrate the sometimes-competing influence of both thermal conductance and thermal inertia on adsorbent bed temperature following characteristics, which tend to confound results for $k/L < 10$.

The boundary condition temperature period-of-oscillation (τ) was varied from the baseline 3 sec. to a value of 6 sec. This extended duration of time after the temperature swing caused the adsorbent bed to better follow the boundary condition temperature. Figures 38 and 39 show the AUC and Amp ratios for this variation in period-of-oscillation, τ. Notice that the AUC ratio and Amp ratio tend to approach 100% as the frequency of oscillation is decreased. At this lower oscillation frequency, designs with k/L values of > 10 produced temperature amplitudes of nearly 100% and AUC ratios > 80%.

Figure 2 - S/F prediction of Sorbent Temperatures
Sorbent: keff=0.1, Cpeff=1000, rhoeff=540, 1/2gap=0.04 in.,

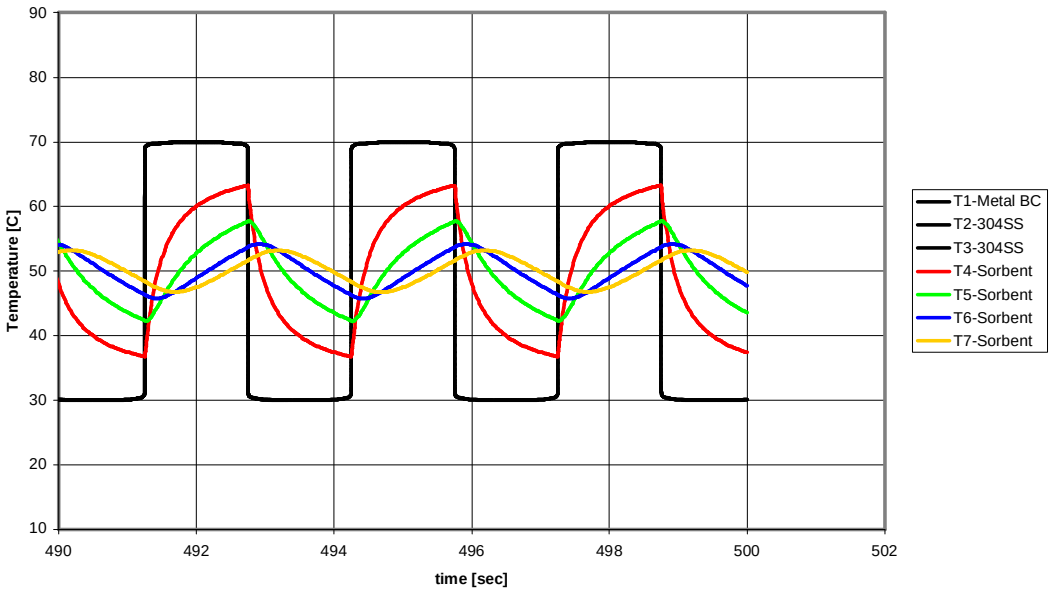

Figure 26. Sorbent temperatures (k=0.1 W/m-K, gap = 0.08 in, 30 to 70 C).

Figure 3 - S/F prediction of Sorbent Temperatures
Sorbent: keff=3.0, Cpeff=1000, rhoeff=540, 1/2gap=0.04 in.,

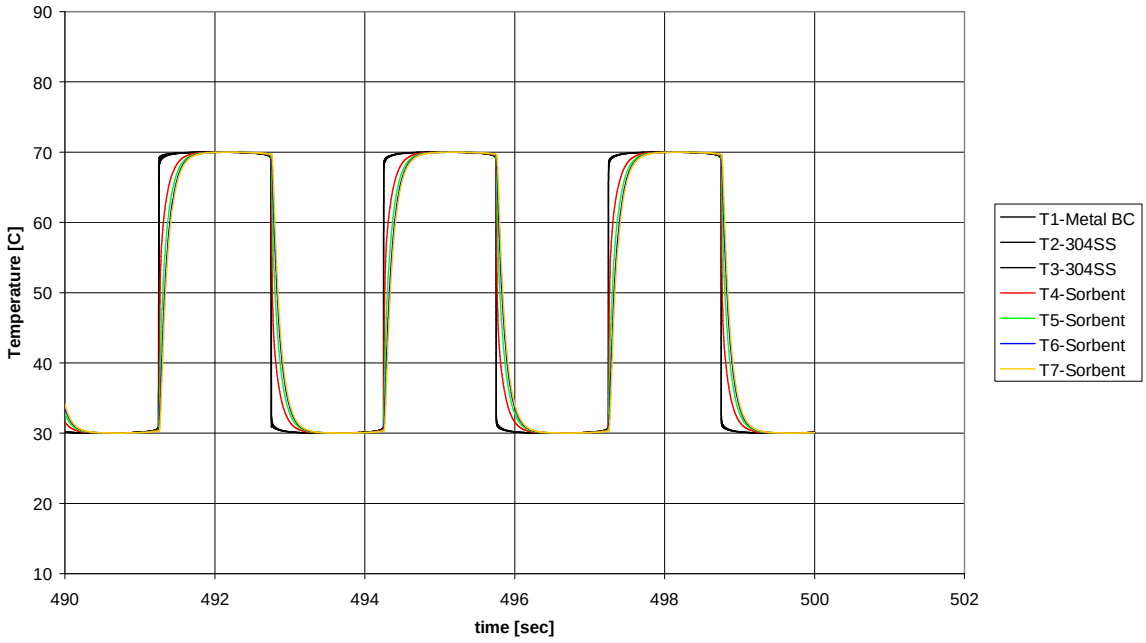

Figure 27. Sorbent temperatures (k=3 W/m-K, gap = 0.08 in, 30 to 70 C)

Figure 4 - S/F prediction of Sorbent Temperatures
Sorbent: keff=1.0, Cpeff=1000, rhoeff=540, 1/2gap=0.04 in.,

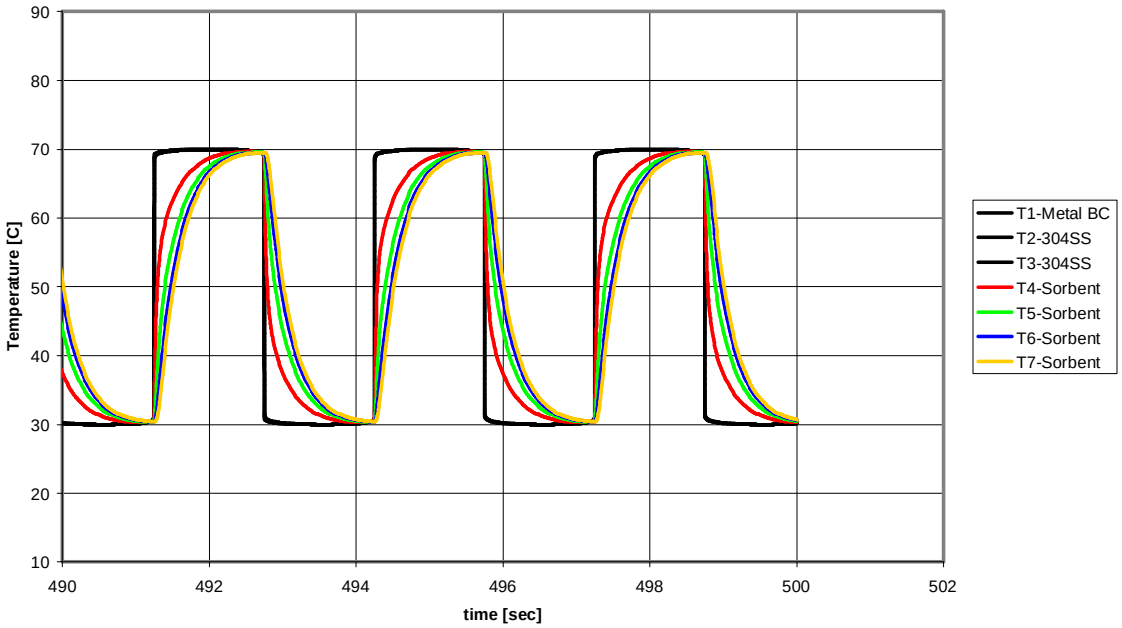

Figure 28. Sorbent temperatures (k=1 W/m-K, gap = 0.08 in, 30 to 70 C).

Figure 5 - S/F prediction of Sorbent Temperatures
Sorbent: keff=1.0, Cpeff=1000, rhoeff=540, 1/2gap=0.04 in.,

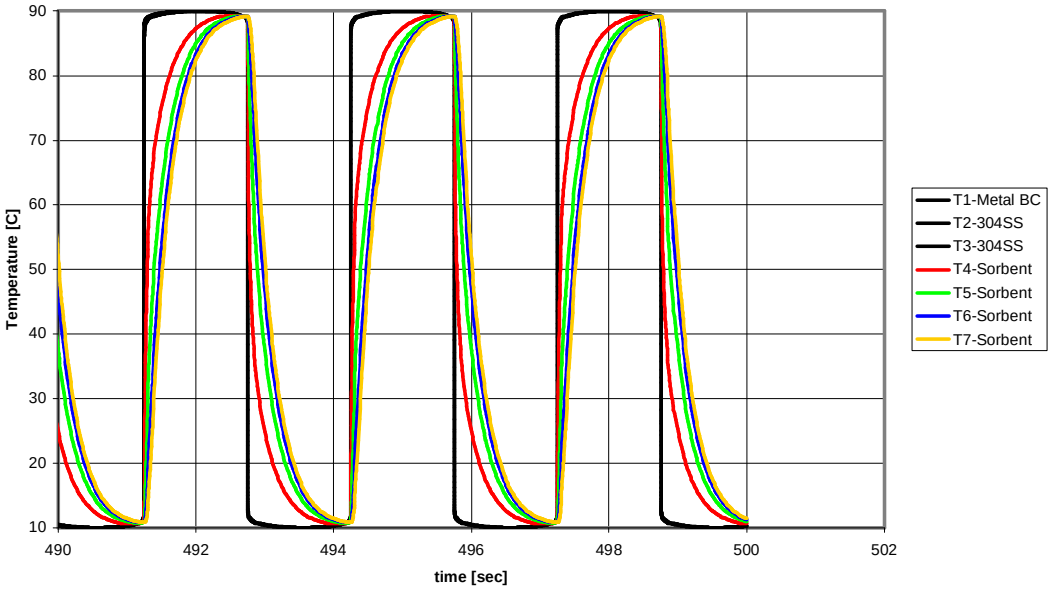

Figure 29. Sorbent temperatures (k=1 W/m-K, gap = 0.08 in, 10 to 90 C).

Figure 6 - S/F prediction of Sorbent Temperatures
Sorbent: keff=1.0, Cpeff=1000, rhoeff=540, 1/2gap=0.02 in.,

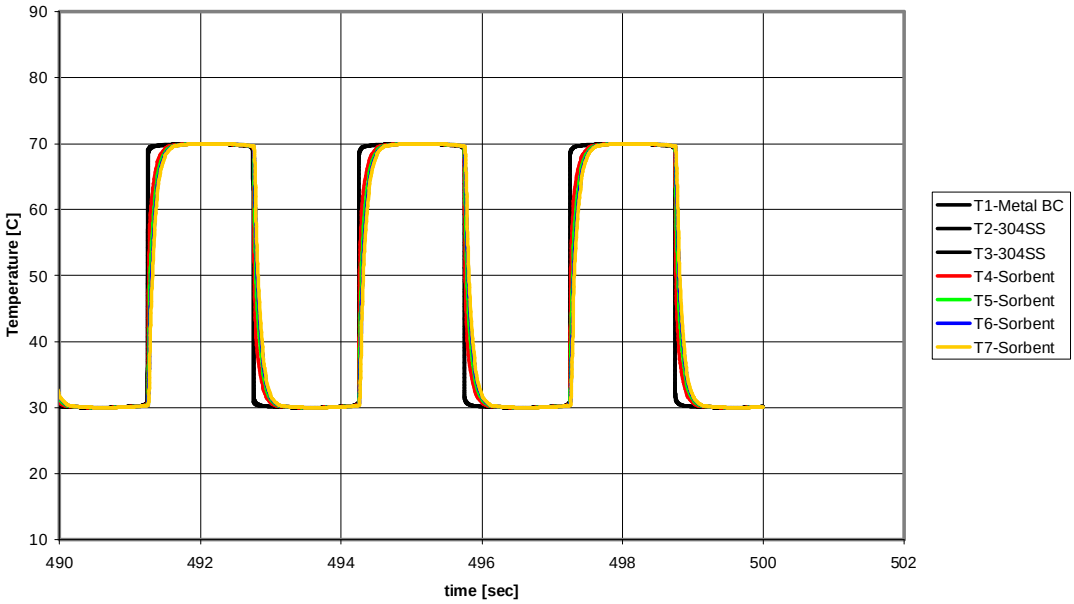

Figure 30. Sorbent temperatures (k=1 W/m-K, gap = 0.04 in, 30 to 70 C).

Figure 7 - S/F prediction of Sorbent Temperatures
Sorbent: keff=1.0, Cpeff=1000, rhoeff=540, 1/2gap=0.05 in.,

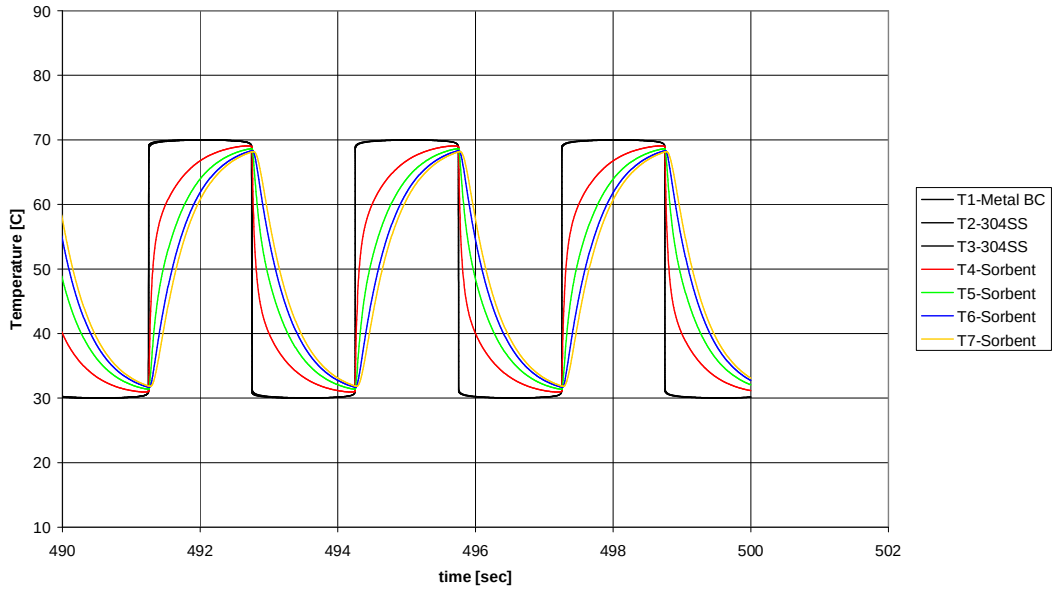

Figure 31. Sorbent temperatures (k=1 W/m-K, gap = 0.1 in, 30 to 70 C).

Figure 8 - S/F prediction of Sorbent Temperatures
Sorbent: keff=0.18, Cpeff=1000, rhoeff=540, 1/2gap=0.015 in.,

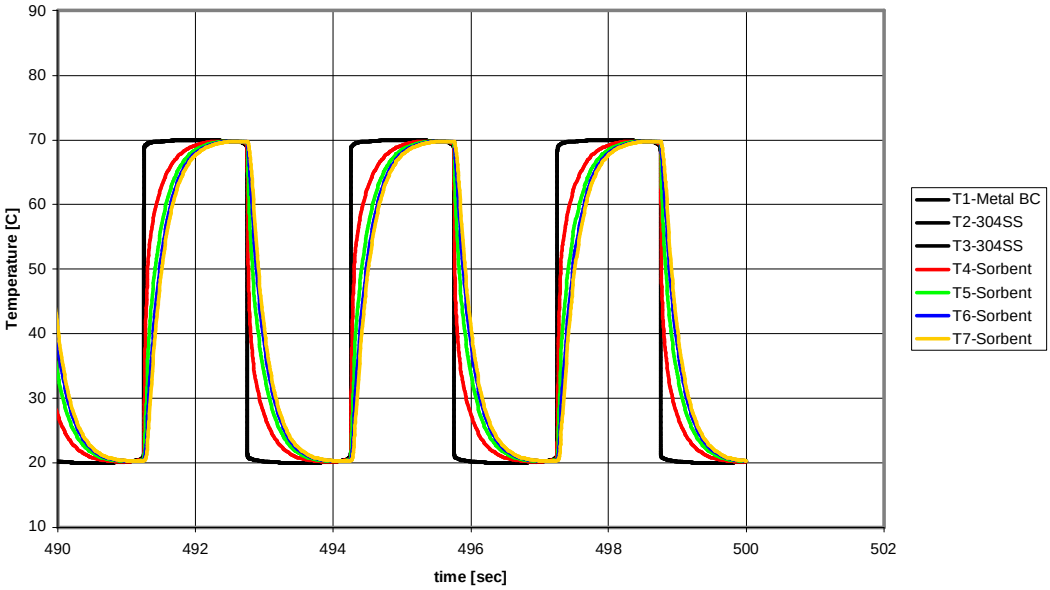

Figure 32. Sorbent temperatures (k=0.18 W/m-K, gap = 0.03 in, 20 to 70 C).

Figure 9 - S/F prediction of Sorbent Temperatures
Sorbent: keff=1.0, Cpeff=1000, rhoeff=540, 1/2gap=0.080 in.,

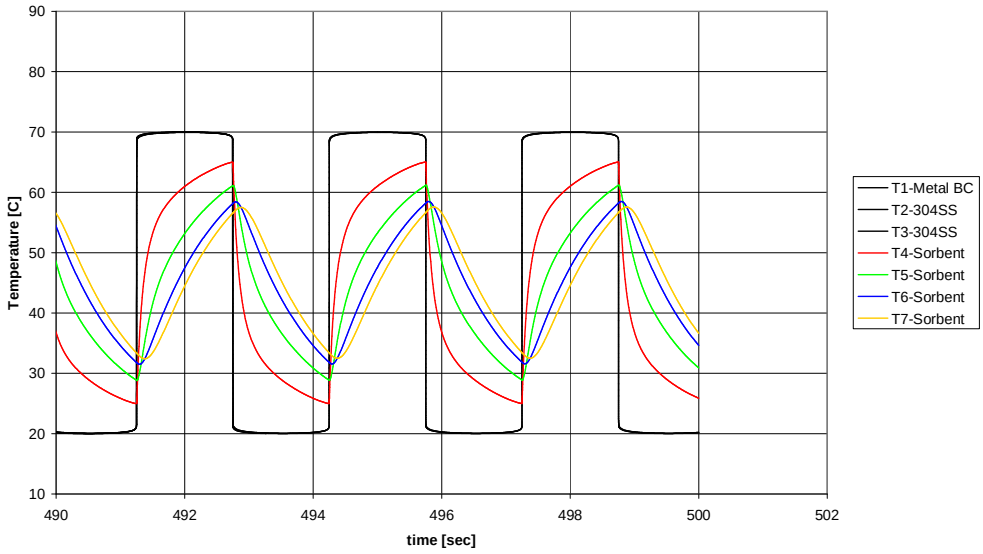

Figure 33. Sorbent temperatures (k=1 W/m-K, gap = 0.16 in, 20 to 70 C).

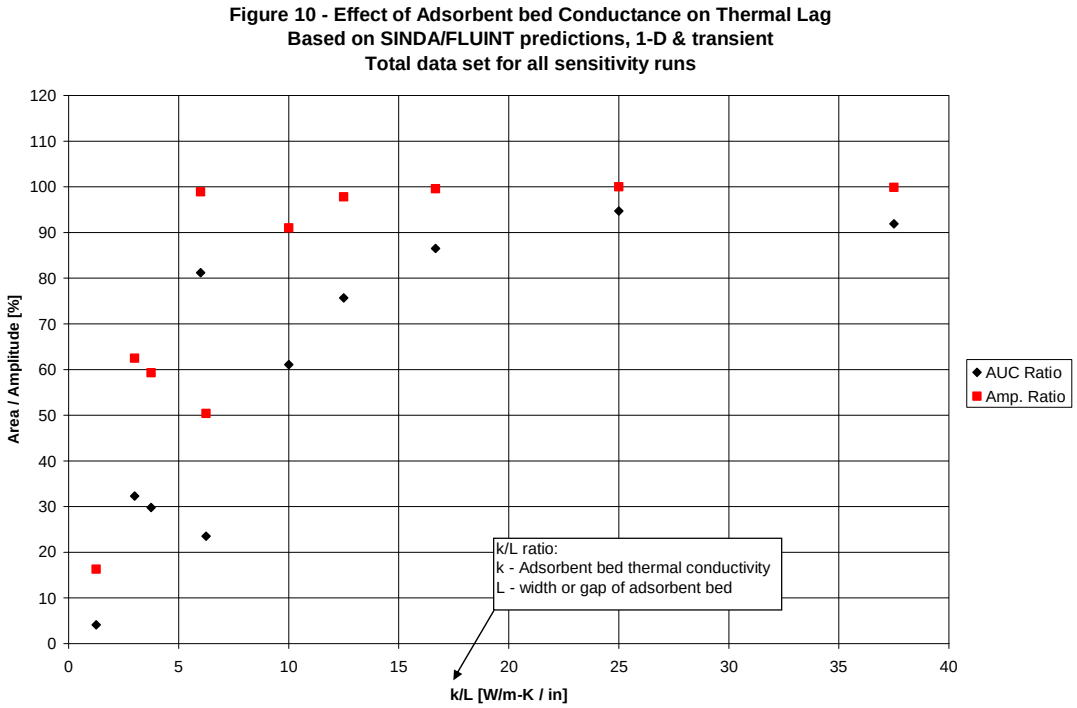

Figure 34. AUC and Amp ratio – all runs.

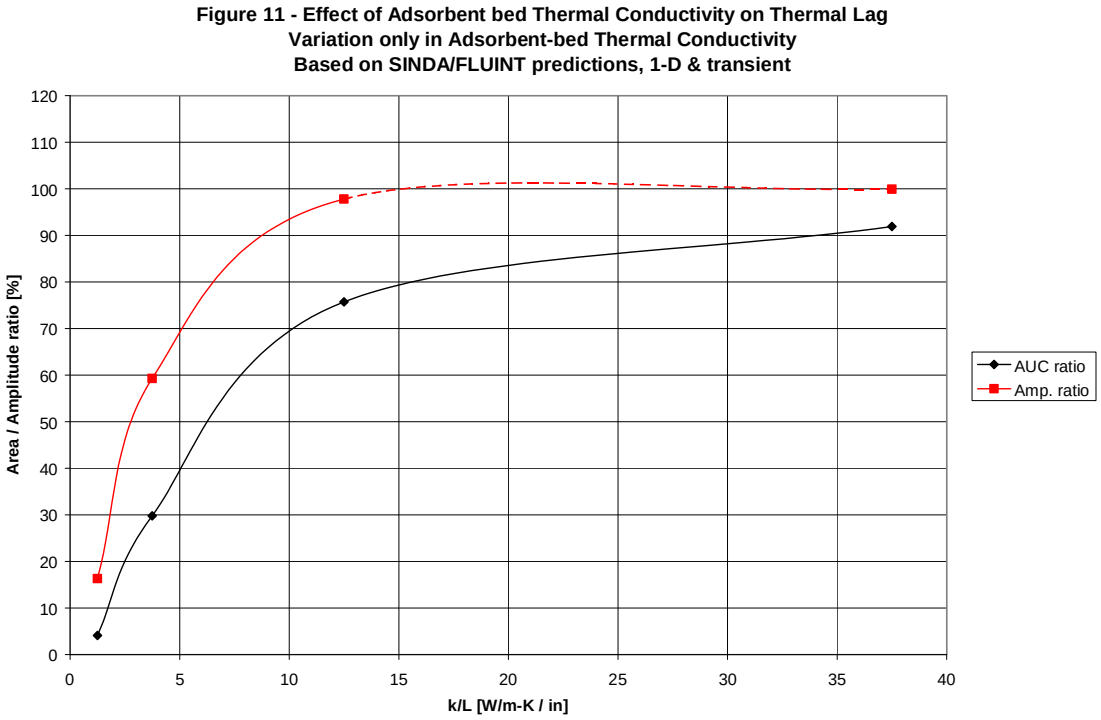

Figure 35. AUC and Amp ratio – effect of thermal conductivity only.

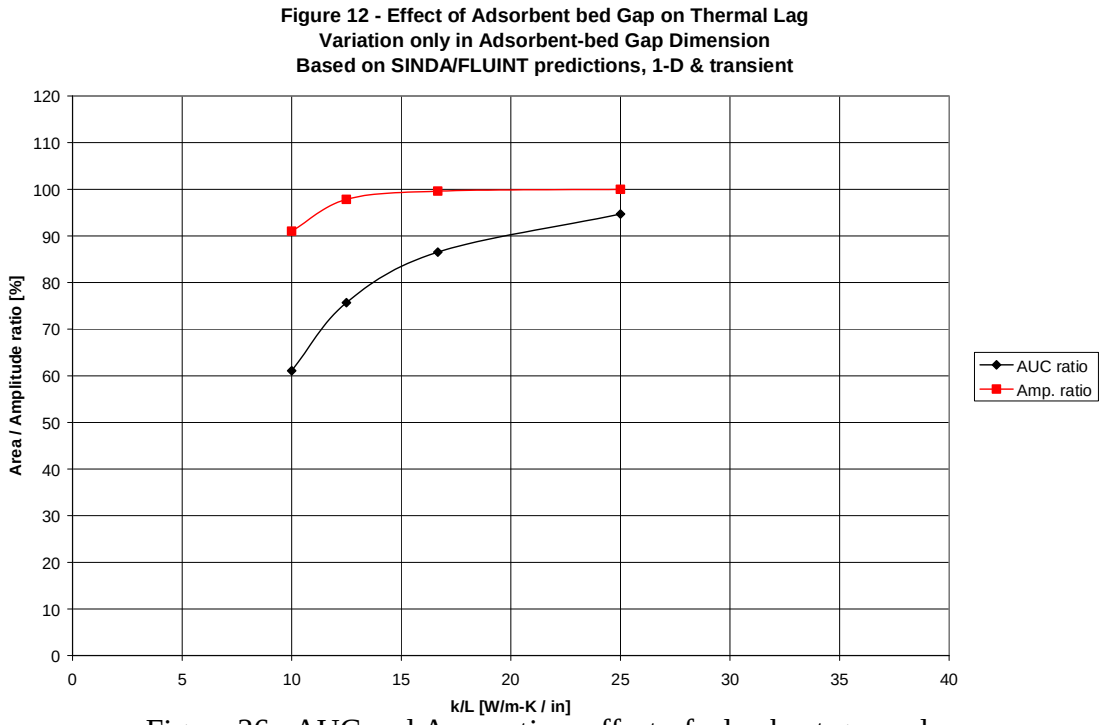

Figure 36. AUC and Amp ratio – effect of adsorbent gap only.

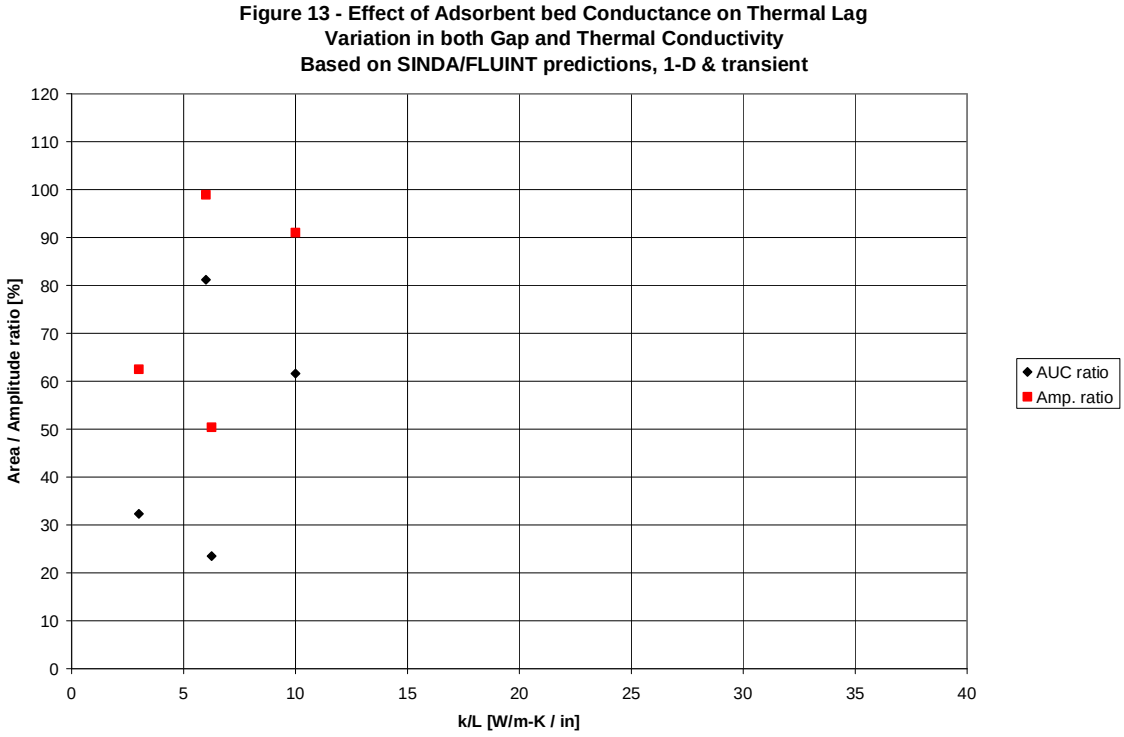

Figure 37. AUC and Amp ratio – combined effect of adsorbent gap and k.

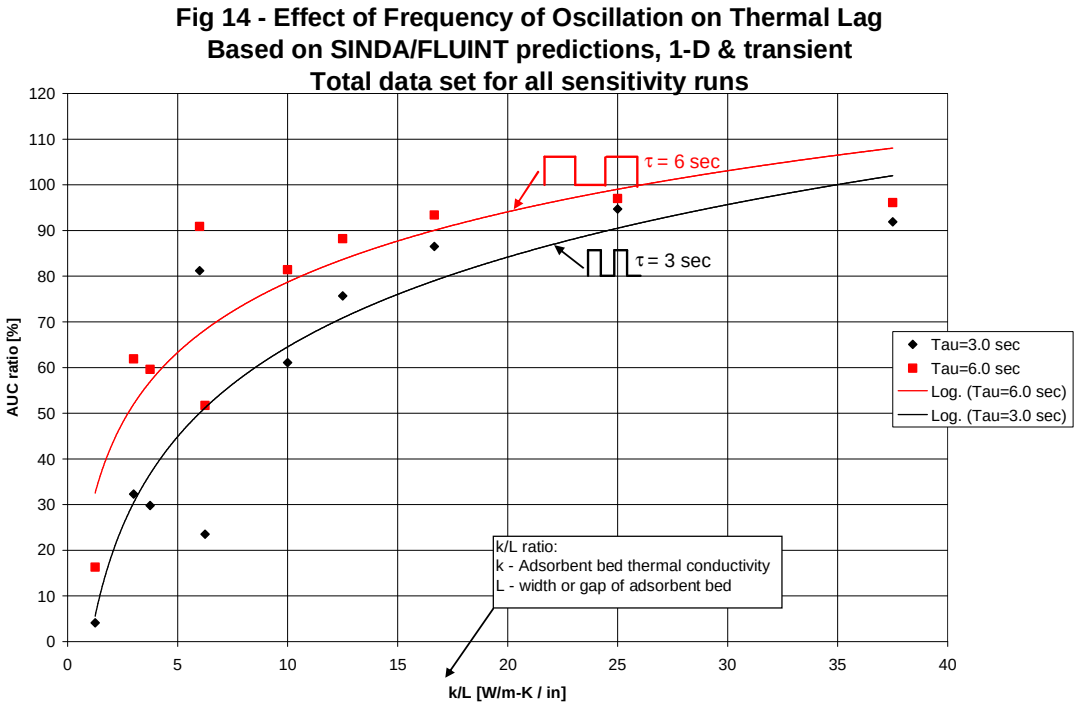

Figure 38. AUC for 3 versus 6 seconds full cycle time.

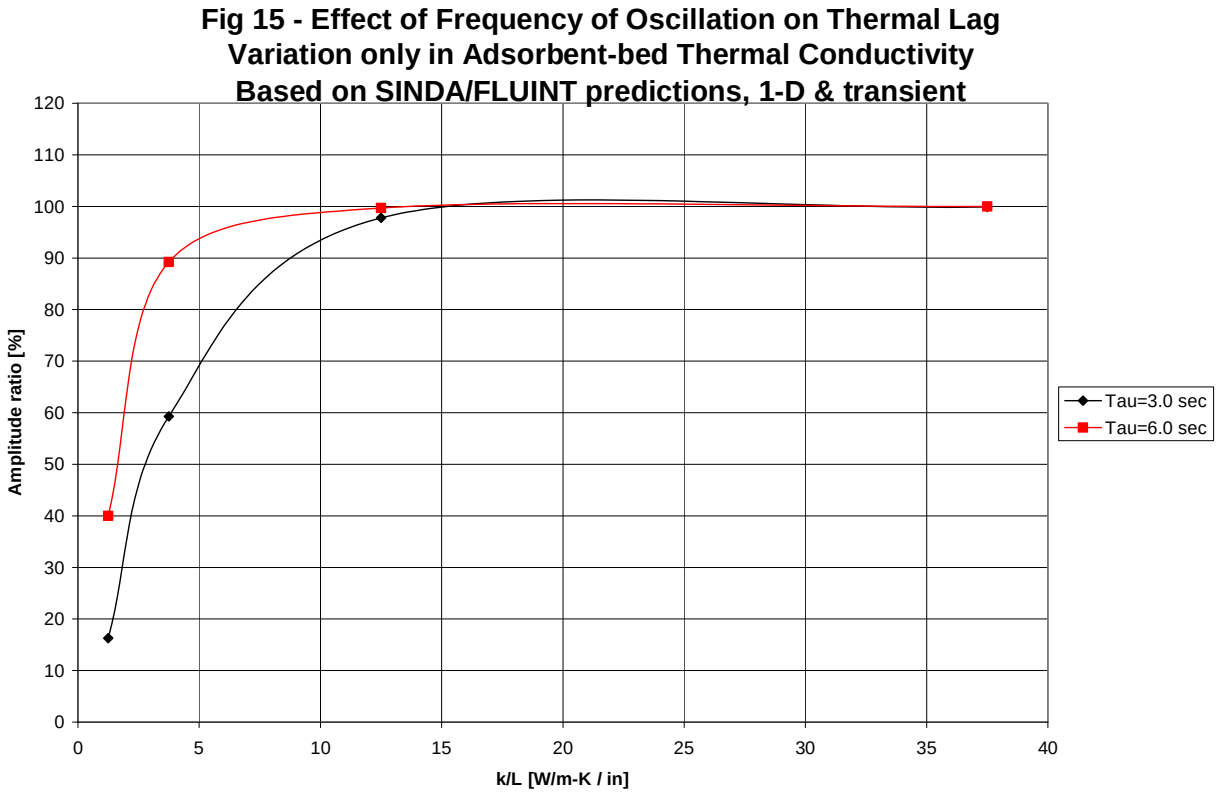

Figure 39. Amplitude ratio for 3 versus 6 seconds full cycle time.

Revised Test Stand and Data Analysis Methodology for Evaluating Effect of Feed Impurities on Adsorbent Capacity

A simple method was devised for measuring the differential capacity of the adsorbent for mixtures of various gas compositions over the temperature range of interest. The adsorbent testing apparatus shown in Figure 40 is used for these tests to provide an approximately isothermal adsorbent bed at a temperature which is controlled via heat exchange fluid.

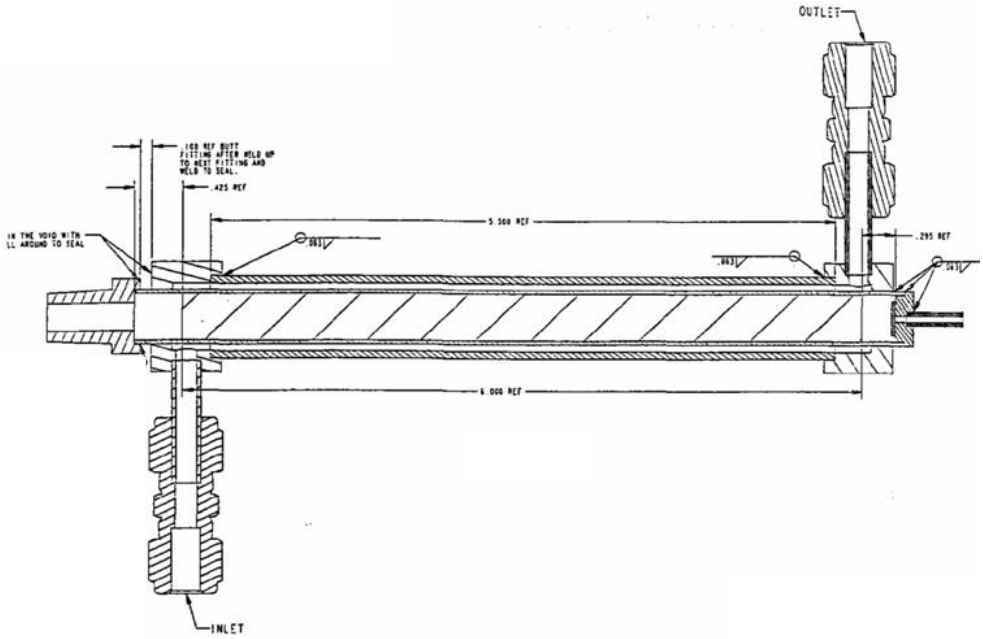

Figure 40. Adsorbent testing apparatus. Process gases flow downward through the (vertically mounted) adsorbent bed in the center tube and heat exchange fluid flows co-currently in an outer annulus to maintain near isothermal operation.

A new approach for measuring capacity, and especially small changes in capacity as a result of feed impurities was developed. The previous method used in the first phase of the program required significant data deconvolution to account for transients mass change induced effects in mass flow meter readings. A more simple and robust method was developed, as shown in Figure 41. In short, the adsorbent bed was purged with a non-adsorbed species (He), flooded with the feed gas at one temperature, and then allowed to re-equilibrate with the feed gas from a well known reservoir at a different temperature. Pressure on the connecting reservoir was measured, as were the gas composition in the bed and the reservoir after the test. The requirement for transient measurement of flows and compositions that were varying with sub-second time constants was eliminated. A direct measurement of differential (not absolute) capacity may be easily calculated.

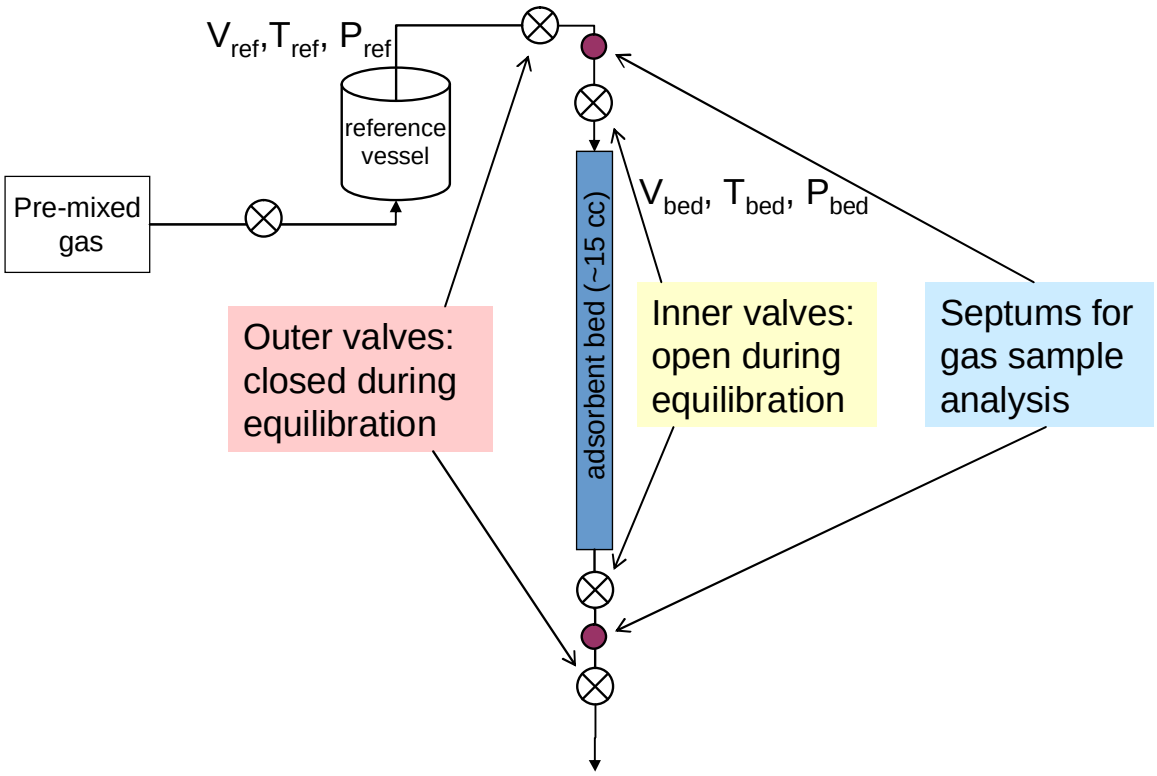

Figure 41. Adsorbent testing setup. Pre-mixed process gas is supplied to the adsorbent bed from an upstream reference vessel of known volume. Separate GC samples are taken from above bed and below bed for comparison.

The valve-to-valve volume of the reference vessel (V_{ref} = 306.1 cc) and the valve to valve volume of the adsorbent bed (V_{bed} = 16.86 cc) were calculated and used in the analysis. For a given void fraction in the packed bed, the differential capacity of each gaseous component in the adsorbent bed between an upper temperature (T_{bed1}) and a lower temperature (T_{bed2}) at a constant pressure were measured. The following procedure was used in the system shown in Figure 41 to measure the differential isothermal capacity of the adsorbent for various mixtures of gases:

1. Set the coolant temperature as needed to bring the adsorbent bed to the desired upper temperature (T_{bed1}).
2. Start gas flow of the desired feed composition to be tested and set the back pressure regulator downstream of the adsorbent bed to maintain the device at the desired pressure (P_{bed1}).
3. Flood the reference vessel and adsorbent bed with feed gas of constant composition (from a pre-mixed tank) at the desired pressure (P_{bed1}) and upper temperature (T_{bed1}). [~30 min]
4. While at the upper temperature (T_{bed1}) and desired pressure P_{bed1}, valve-off the adsorbent bed.
5. Let the upstream reference vessel to rise to a slightly higher pressure (P_{ref1}).
6. Valve off the reference vessel and stop the feed gas flow.
7. Record the bed pressure (P_{bed1}) and temperature (T_{bed1}).

8. Lower the coolant temperature until the bed temperature reaches the desired lower temperature (T_{bed2}).
9. Record system pressures (P_{bed2}, P_{ref1}) and temperatures (T_{bed2}, T_{ref1}).
10. Bleed in feed gas from the reference vessel until the bed pressure slightly exceeds the desired pressure (P_{bed1}). [use experience to anticipate how much P_{bed} will drop during equilibration due to adsorption]
11. Immediately record the new reference vessel pressure (P_{ref2}).
12. Keep both reference vessel and bed isothermal and valved-off and allow each to equilibrate for 16+ hours.
13. Record the new bed pressure ($P_{bed3} \approx P_{bed1}$) and temperature ($T_{bed3}$).
14. Close off inner valves and take a syringe sample of gas from just upstream and just downstream of the adsorbent bed via septum to measure the composition of gas not adsorbed. If the two samples match in composition this is evidence that the system equilibration time was adequate.
15. Infer from the change in reference vessel pressure, the feed gas composition, and the composition of the gas not adsorbed how much of each species was adsorbed.

In this non-reacting system, a species mole balance was used to calculate the moles of each species differentially adsorbed, as shown in Equation 1.

$$n_{i,ads,Tbed2} + n_{i,void,Tbed2} = n_{i,ads,Tbed1} + n_{i,void,Tbed1} + n_{i,\,fed} \qquad \text{(EQ 1)}$$

where $n_{i,\,ads}$ is the number of moles of species *i* adsorbed, and $n_{i,\,void}$ is the number of moles of species *i* in the voids between particles. Since the reference volume and the initial bed void fraction were well flushed at conditions of T_{bed1} and P_{bed1}, it is assumed that the initial composition in the bed voids and reference volume is the same as the feed gas. Substituting into Equation 1 and re-arranging we obtain the differential moles adsorbed of each species i (Equation 2):

$$n_{i,ads,Tbed2} - n_{i,ads,Tbed1} = \left(n_{total,void,Tbed1} + n_{total,\,fed}\right) \cdot x_{i,\,feed} - n_{total,void,Tbed2} \cdot x_{i,void,Tbed2} \qquad \text{(EQ 2)}$$

where:

$n_{i,\,ads}$ is the number of moles of component *i* adsorbed at T_{bed} & P_{bed}
n_{total} is the number of moles of all components (fed or in the bed voids)
$x_{i,\,feed}$ is the mole fraction of component *i* in the feed
$x_{i,\,void}$ is the equilibrated mole fraction of component *i* in the bed voids

In Equation 2, the total moles fed to the adsorbent bed from the reference vessel after lowering the bed temperature was calculated assuming ideal gas behavior, as shown in Equation 3:

$$n_{total,\,fed} = \left(\frac{P_{ref1}}{T_{ref1}} - \frac{P_{ref2}}{T_{ref2}}\right) \cdot \frac{V_{ref}}{R_{gas}} \qquad \text{(EQ 3)}$$

where the *ref* subscript denotes the reference volume, P is total pressure, T is temperature, V is valve to valve volume, and R_{gas} is the universal gas constant. The total moles in the voids of the isothermal bed at a given temperature and pressure in Equation 1 was calculated assuming ideal gas behavior, as in Equation 3:

$$n_{total,void} = \frac{P_{bed} \cdot V_{bed,void}}{R_{gas} \cdot T_{bed}} \qquad \text{(EQ 4)}$$

where $V_{bed,\ void}$ is the valve-to valve void volume of the adsorbent bed section. The adsorbent bed was assumed to have a void fraction of 0.35, although if macro pores within the particles are included as void volume, a much larger void fraction might be assumed. The reason for not including macropores within the particles as void volume is that these pores are not swept out by convection and thus the volume contained therein will retain gas rather than be swept out during the quick (on the order of seconds) sweeping/flushing steps typical of a rapid thermal swing adsorption process.

The mole fraction of each species in the adsorbed gas ($x_{i,\ ads}$) was then calculated as differential moles adsorbed of each species *i* divided by the sum of all differential moles adsorbed.

The methane/nitrogen separation factor was calculated in the same way as is suggested by C.J. King (Separation Processes, p. 29, 1980, McGraw Hill, New York), which is shown in Equation 5 below.

$$\alpha_{CH_4/N_2} = \frac{\left(x_{CH_4,ads} \Big/ x_{N_2,ads} \right)}{\left(x_{CH_4,void} \Big/ x_{N_2,void} \right)} \qquad \text{(EQ 5)}$$

A gas chromatograph (GC) was used to analyze the gas composition in the adsorbent bed voids after allowing the composition to equilibrate for >16 hours. This gas composition was analyzed from a 0.05 ml volume sample taken by syringe through a septum. The syringe was first purged with a 0.05 ml sample which was then discarded. Since the removal of gas volume from the system slightly lowers the pressure of the system, only a two GC sample was analyzed for each data point (i.e. each equilibration cycle), one for CO2, another for all gas species.

Helium, nitrogen, and methane pure gases were tested for reference purposes on each type of adsorbent.

The Baseline and Baseline-with-high-CO_2 mixtures were also tested on the PICA adsorbent. All testing was performed at 100 psig, except for a few tests which were carried out at 50 and 140 psig using the PICA adsorbent to see the effect of pressure on the differential adsorption capacity and selectivity. Pure component gas data were taken at 100 psig and 50 psig.

Each adsorbent bed was baked-out at 105-150°C and 1 atm in a small flow of pure helium for about 4 hours before testing.

Modeling Results and Discussion

The transient thermal model simulated the impact of a phase change heat transfer fluid in the heat transfer channel, where the wall temperature remains constant during each half cycle and only the quality of gas or liquid changes as the adsorbent bed is either cooled or heated.

Refined measurement of effective thermal conductivity

The preliminary model work was based on a single measurement for the effective thermal conductivity for the granular carbon bed. A more statistical analysis of this parameter was conducted by collecting additional samples.

The effective thermal conductivity of Calgon activated carbon powder, ground and sieved to collect 149 to 210 μm size particles (70 to 100 mesh), was measured using the specifically designed and constructed device described in a previous report (41905 FY06Q1).

Based on an evaluation of five powder samples (manually shaken to obtain a consistent tap density of 0.62± 0.011 kg/m^3), the thermal conductivity of the packed powder was measured to be 0.21± 0.035 W/m-K, with a 95% confidence. Because several additional tests are required to significantly enhance the precision of the measurement, the values were deemed to provide an acceptable measure of the effective thermal conductivity of the powder. Table 17 summarizes the raw data.

Sample No.	***Sample Mass (g)***	***Bed Density (kg/m^3)***	***Thermal Conductivity (W/m-K)***
1	2.109	0.62	0.256
2	2.093	0.63	0.196
3	2.098	0.61	0.206
4	2.094	0.61	0.221
5	2.093	0.61	0.182

Table 17. Analysis of multiple granular carbon beds for effective thermal conductivity.

These results confirmed that the initial value used for system modeling (0.18 W/m-K) was well within the 95% confidence interval of 0.175 to 0.245 W/m-K and is a reasonable value for modeling.

Thermal Modeling with Adsorption Added:

25 simulations were conducted to evaluate influences of changes in adsorbent bed thermal conductivity, bed thickness, and temperature amplitude on the net methane adsorbed. The matrix of runs is tabulated in Table 18. The adsorbent bed thickness varied from 0.03 in. to 0.16 in.

The adsorbent bed thermal conductivity varied from 0.18 W/m-K to 1.0 W/m-K. Finally the temperature amplitude varied from 20 °C to 40 °C. This sensitivity study matrix was arrived by use of the software tool Design Expert. Results from these 25 simulations are shown graphically in Figures 42a through 42c. As expected, as the temperature swing is increased the level of adsorption increased. However, in order to realize this temperature amplitude effect on adsorption level, the adsorbent bed thermal conductivity and bed thickness have to be larger in magnitude.

At a given temperature amplitude, say 60 °C (Figure 42b), the highest level of methane adsorption occurs when the bed thickness and bed thermal conductivity are maximized. Notice that changes in both the thermal conductivity and bed thickness have equal effects on methane adsorption. Notice too that at very low levels of thermal conductivity (0.18 W/m-K), changes in bed thickness have relatively little effect on methane adsorption. Likewise, at low levels on bed thickness (0.03 in.), changes in bed thermal conductivity have little effect on adsorption. Therefore these very low levels of bed thermal conductivities and bed thickness are highly limiting in adsorbent bed performance.

Table 18 also includes a ratio of the predicted methane adsorption to the ideal methane adsorption for the given operating condition. Very high ratios or "CH4 ads. efficiencies" do occur for all temperature amplitudes, occur for high levels of thermal conductivity, and occur for low bed thicknesses. Notice that a smaller bed thickness will yield an attractive adsorbent bed efficiency but yield low adsorption levels. On the other hand, high values for thermal conductivity will yield both high efficiencies as well as high methane adsorption levels. Figure 43 illustrates the predicted regions of high adsorbent bed performance, with performance based on methane adsorbed as well as adsorbent bed efficiency. Optimized performance seems to favor very high values of thermal conductivity and somewhat mid-range values of bed thickness. As seen in Figure 43, as the bed thickness approaches the maximum level of 0.16 in., the adsorbent bed efficiency begins to fall off. At lower levels of thermal conductivity and thinner beds, the efficiency is reduced. If the adsorbent cost is modest, however, there is little penalty with using more adsorbent than otherwise might be necessary.

SINDA/FLUINT simulation predictions of methane adsorption were compared to the more or less curve-fitted results from Design Expert. 17 unique designs were considered and compared over a range of bed thicknesses and temperature amplitudes. The median error was found to be 6% and the standard deviation was 6%.

The analysis tool SINDA/FLUINT was used to predict methane adsorption in the adsorbent bed. The coupling between methane adsorbed and bed temperatures was based on an empirical relationship. Analysis results showed that the adsorbent bed adsorbed the highest quantity of methane when bed thickness, bed thermal conductivity, and temperature amplitude were at the highest levels. Results also showed that when *either* thermal conductivity, or bed thickness, or temperature amplitude were at the lowest level, performance of the adsorbent bed was poor regardless of the other two independent variables. Optimum adsorbent bed performance occurred at very high levels of bed thermal conductivity (1.0 W/m-K) and somewhat midrange levels of bed thickness (0.12 in.).

Run #	Bed Thickness [in]	Thermal Cndctvy. [W/m-K]	Temp. Swing [C]	Ambient Tem. [C]	Simulated CH4 Adsorption [mg/in2]	Ideal CH4 Adsorption [mg/in2]	CH4 Adsorption Efficiency [%]
1	0.12	1.00	58	29	29.36	29.22	100
2	0.16	0.18	57	28.5	14.92	38.26	39
3	0.16	1.00	40	20	23.29	26.56	88
4	0.06	0.69	43	21.5	10.71	10.73	100
5	0.06	0.57	59	29.5	14.83	14.87	100
6	0.16	0.77	51	25.5	27.23	34.09	80
7	0.07	1.00	80	40	23.95	23.97	100
8	0.11	0.79	40	20	17.64	18.26	97
9	0.03	0.18	80	40	10.26	10.27	100
10	0.03	0.75	80	40	10.27	10.27	100
11	0.03	0.45	40	20	4.98	4.98	100
12	0.03	0.18	53	26.5	6.64	6.65	100
13	0.06	0.27	67	33.5	16.6	17.00	98
14	0.11	0.18	70	35	18.36	32.65	56
15	0.16	0.40	69	34.5	26.99	46.77	58
16	0.03	1.00	40	20	4.98	4.98	100
17	0.11	0.49	62	31	25.38	28.72	88
18	0.07	0.92	54	27	15.8	15.82	100
19	0.03	1.00	68	34	8.63	8.63	100
20	0.16	0.18	80	40	21.08	54.80	38
21	0.07	0.18	40	20	10.01	11.62	86
22	0.16	0.18	40	20	10.42	26.56	39
23	0.16	1.00	80	40	47.73	54.80	87
24	0.12	0.55	80	40	35.55	41.10	87
25	0.12	0.34	48	24	17.24	24.02	72

Table 18. Simulation test matrix for evaluating thermal swing impact on adsorption

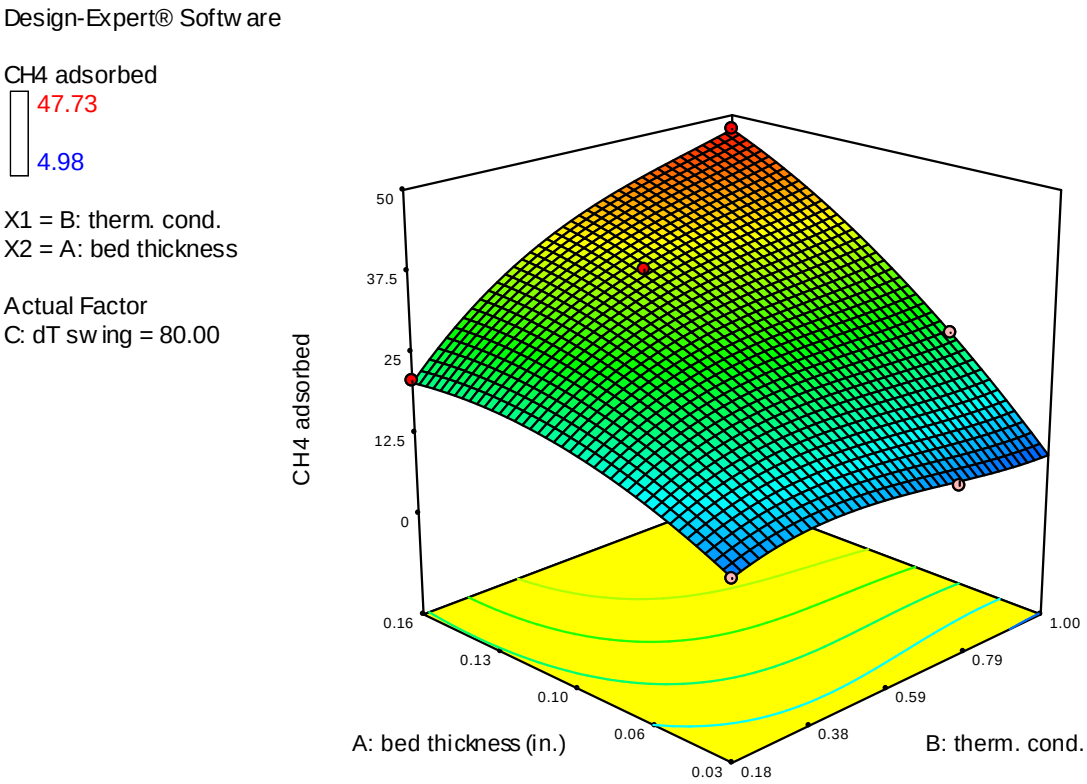

Figure 42a. Methane capacity as a function of bed thickness and thermal conductivity for 80 C differential temperature.

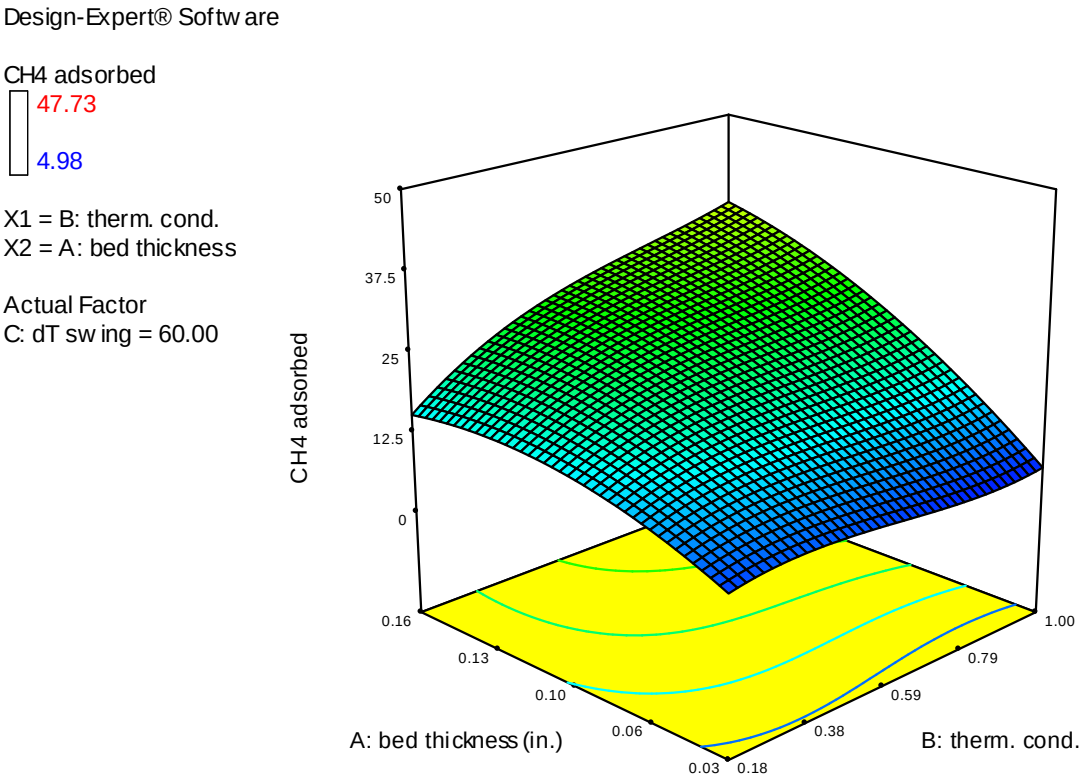

Figure 42b. Methane capacity as a function of bed thickness and thermal conductivity for 60 C differential temperature.

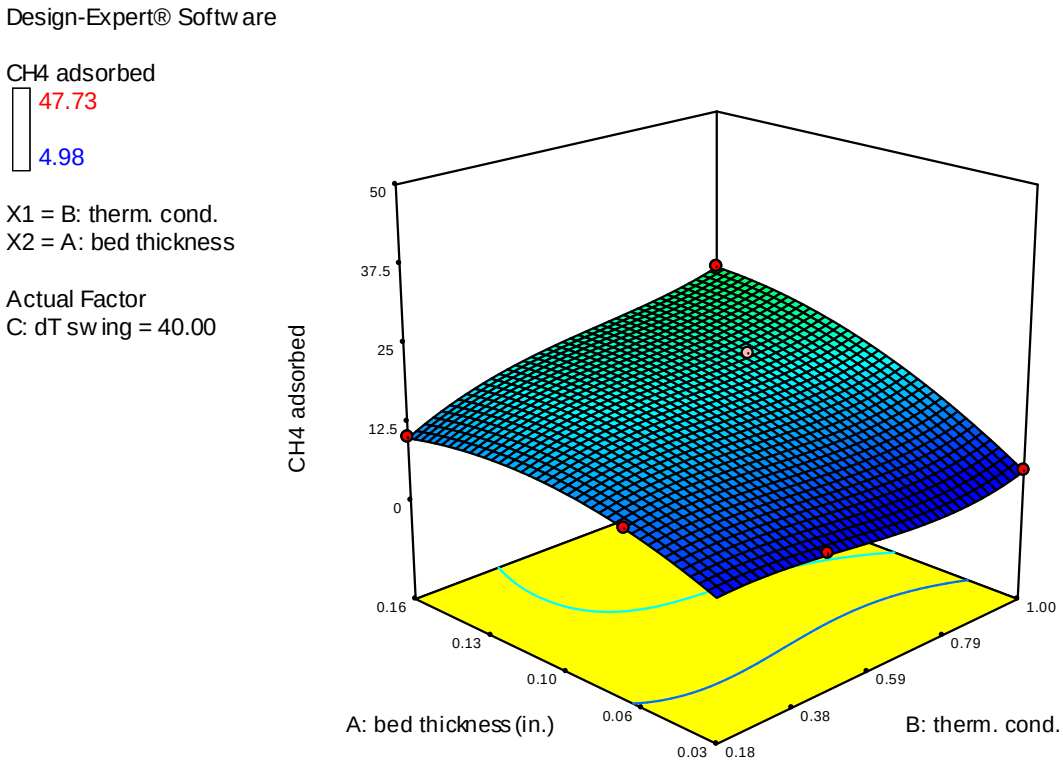

Figure 42c. Methane capacity as a function of bed thickness and thermal conductivity for 40 C differential temperature.

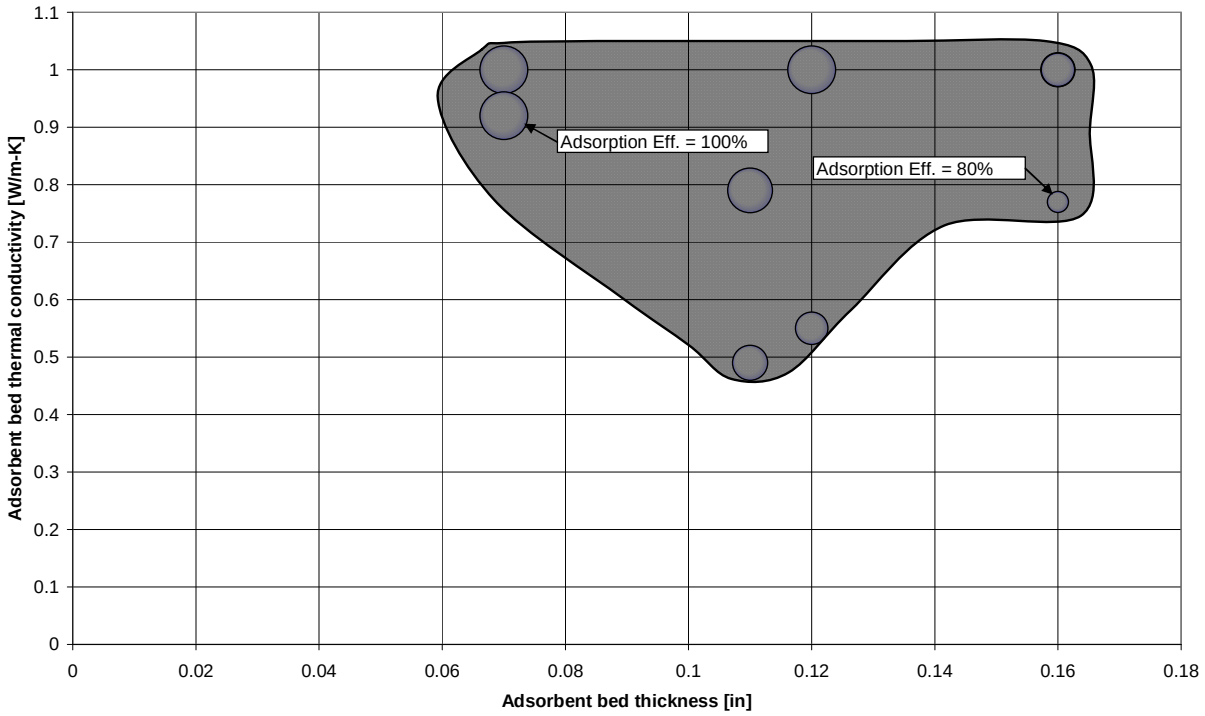

Figure 43. Relationship on adsorption efficiency as a function of effective thermal conductivity and bed thickness.

Experimental Results and Discussion

Two types of adsorbents were tested as a possible candidates for the TSA nitrogen rejection process: Calgon carbon and a new proprietary adsorbent.

Calgon Carbon

The following pre-mixed gas compositions were tested on the Calgon carbon adsorbent:

- Baseline: 80% CH_4, 15.0% N_2, 5% He
- Baseline-with-CO_2: 80% CH_4, 13.0% N_2, 5% He, 2% CO_2
- Baseline-with-high-CO_2: 75% CH_4, 10.0% N_2, 5% He,10% CO_2
- Baseline-with-O_2: 80% CH_4, 14.5% N_2, 5% He, 0.5% O_2

The results from the experiments are shown below in Tables 19-22. Table 19 shows the results on Calgon carbon using pure gases (the differential moles adsorbed are shown in bold). Note in Table 19 that the ratio of moles of pure CH_4 adsorbed per gram of adsorbent to moles of pure N_2 adsorbed per gram of adsorbent is about 1.6 on average. Note also that the differential adsorption for pure He is not zero, but is a significant fraction (3.7%) of the differential adsorption for pure

CH_4, thus it cannot be used as a tracer as was originally intended. The results show reasonable repeatability for the pure gas measurements.

		pure He	Pure He	pure CH4	Pure CH4	pure N2	Pure N2
Total time equilibrated	hh:mm	0:05	2:11	0:21	0:47	0:04	0:56
adsorbent type		Calgon, 80-100 mesh	Calgon, 80-100 mesh	Calgon, 80-100 mesh	Calgon, 80-100 mesh	Calgon, 80-100 mesh	Calgon, 80-100 mesh
assumed void fraction		0.35	0.35	0.35	0.35	0.35	0.35
target high temperature	°C	70	70	70	70	70	70
target low temperature	°C	20	20	20	20	20	20
adsorbent bed initial P at T hot	(psig)	99.4	100.2	100.4	100.2	100.2	100.7
total differential moles adsorbed/gram adsorbent		**4.42E-05**	**4.57E-05**	**1.23E-03**	**1.23E-03**	**7.56E-04**	**7.71E-04**

Table 19. Differential adsorption results for pure gases on 80-100 mesh Calgon carbon adsorbent at 100 psig between 20 and 70°C.

Table 20 shows similar results for the PICA carbon, showing the effect of pressure on the differential adsorption capacity of each of the pure gases. For each of the pure gases, higher pressure results in higher total adsorption capacity, as would be expected. In comparing the 100 psig results in Table 20 (PICA) with the results in Table 19 (Calgon), it appears that the PICA adsorbent has a higher total adsorption capacity than does the Calgon adsorbent for all three pure gases (higher by ~40% for He, ~30% for methane, and ~20% for nitrogen).

		pure He	pure He	pure He	pure CH4	Pure CH4	Pure CH4	pure N2	Pure N2	Pure N2
TOS	hh:mm	0:32	0:22	1:04	0:32	0:48	1:01	0:19	0:20	16:18
adsorbent type		PICA, G55C 50x100	PICA, G55C 50x100	PICA, G55C 50x100	PICA, G55C 50x100	PICA, G55C 50x102	PICA, G55C 50x100	PICA, G55C 50x100	PICA, G55C 50x101	PICA, G55C 50x100
assumed void fraction		0.35	0.35	0.35	0.35	0.35	0.35	0.35	0.35	0.35
target high temperature	°C	70	70	70	70	70	70	70	70	70
target low temperature	°C	20	20	20	20	20	20	20	20	20
adsorbent bed initial P	(psig)	**50.9**	**100.6**	**140.6**	**50.9**	**100.3**	**140.9**	**50.8**	**100.6**	**140.8**
total differential moles adsorbed/gram adsorbent		**2.91E-05**	**6.29E-05**	**7.90E-05**	**1.40E-03**	**1.59E-03**	**1.64E-03**	**7.00E-04**	**9.33E-04**	**1.02E-03**

Table 20. Differential adsorption results for pure gases on 50-100 mesh PICA carbon adsorbent at 50-140 psig between 20 and 70°C.

Table 21 compares the differential adsorption results with Calgon carbon adsorbent for each of the gas mixtures tested. The results in Table 21 suggest that within the error of the experiment, the presence of impurities significantly affects neither the total moles adsorbed (~1E-3 moles/gram adsorbent) nor the methane/nitrogen separation factor (~1.7).

		baseline premix	baseline premix	Baseline w/CO2	Baseline w/HIGH CO2	Baseline w/HIGH CO2	Baseline w/HIGH CO2	Baseline w/O2
Total time equilibrated	hh:mm	21:56	70:07	68:33	15:17	21:32	186:15	20:40
adsorbent type		Calgon, 80-100 mesh	Calgon, 80-100 mesh	Calgon, 80-100 mesh	Calgon, 80-100 mesh	Calgon, 80-100 mesh	Calgon, 80-100 mesh	Calgon, 80-100 mesh
assumed void fraction		0.35	0.35	0.35	0.35	0.35	0.35	0.35
target high temperature	°C	70	70	70	70	70	70	70
target low temperature	°C	20	20	20	20	20	20	20
adsorbent bed initial P	psig	100.1	100.2	100.5	100.0	100.0	100.0	101.2
Feed gas composition								
mole % CH4		80.0%	80.0%	80.0%	75.0%	75.0%	75.0%	80.0%
mole % N2		15.0%	15.0%	13.0%	10.0%	10.0%	10.0%	14.5%
mole % CO2		0.0%	0.0%	2.0%	10.0%	10.0%	10.0%	0.0%
mole % O2		0.0%	0.0%	0.0%	0.0%	0.0%	0.0%	0.5%
mole % He		5.0%	5.0%	5.0%	5.0%	5.0%	5.0%	5.0%
total differential moles adsorbed/gram adsorbent	mol/g	**9.87E-04**	**1.03E-03**	**9.27E-04**	**1.09E-03**	**1.09E-03**	**1.10E-03**	**1.01E-03**
Adsorbed gas composition								
mole % CH4		84.2%	82.8%	83.5%	77.6%	76.6%	74.9%	83.6%
mole % N2		13.4%	13.5%	11.7%	9.0%	8.7%	8.3%	12.8%
mole % CO2		0.0%	0.0%	2.1%	11.1%	10.7%	10.8%	0.0%
mole % O2		0.0%	0.0%	0.0%	0.0%	0.0%	0.0%	0.5%
mole % He		2.4%	3.0%	2.6%	4.6%	4.4%	4.4%	3.3%
CH_4/N_2 separation factor	(alpha)	**1.75**	**1.66**	**1.61**	**1.64**	**1.68**	**1.73**	**1.77**

Table 21. Differential adsorption results for various gas mixtures on 80-100 mesh Calgon carbon adsorbent at 100 psig between 20 and 70°C.

In Table 22 the differential adsorption results for the baseline gas mixture on PICA carbon are shown. Surprisingly, the results suggest that the adsorbed gas composition ($x_{i,\ ads}$) is not dependent on pressure over the range of 50-140 psig, although the total moles adsorbed increases with increasing pressure, as expected. The PICA methane/nitrogen separation factor decreases with increasing pressure, and at 100 psig is 15% lower than for the Calgon carbon adsorbent at the same pressure.

		baseline premix	baseline premix	baseline premix
Total time equilibrated	hh:mm	17:25	16:52	17:29
adsorbent type		PICA, G55C 50x100	PICA, G55C 50x103	PICA, G55C 50x100
assumed void fraction		0.35	0.35	0.35
target high temperature	°C	70	70	70
target low temperature	°C	20	20	20
adsorbent bed initial P	psig	**50.8**	**100.5**	**140.2**
Feed gas composition				
mole % CH4		80.0%	80.0%	80.0%
mole % N2		15.0%	15.0%	15.0%
mole % CO2		0.0%	0.0%	0.0%
mole % O2		0.0%	0.0%	0.0%
mole % He		5.0%	5.0%	5.0%
total differential moles adsorbed/gram adsorbent	mol/g	**1.02E-03**	**1.25E-03**	**1.36E-03**
Adsorbed gas composition				
mole % CH4		82.6%	82.6%	82.8%
mole % N2		14.4%	14.3%	14.3%
mole % CO2		0.0%	0.0%	0.0%
mole % O2		0.0%	0.0%	0.0%
mole % He		2.9%	2.8%	2.8%
CH_4/N_2 separation factor	(alpha)	**1.63**	**1.43**	**1.34**

Table 22. Differential adsorption results for the baseline mixture on 50-100 mesh PICA carbon adsorbent at 50-140 psig between 20 and 70°C.

The calculated separation factors (<2) suggest that these adsorbents are behaving far differently than originally evaluated. It is not yet know if storage of the materials for more than a year could have created an issue or if the original method of analysis masked this effect.

Proprietary Adsorbent

The differential CH_4 and N_2 adsorption capacity was measured for this adsorbent for mixtures of two different pre-mixed gas compositions over the temperature range of interest:

- Baseline: 80% CH_4, 15.0% N_2, 5% He
- Baseline-with-high-CO_2: 75% CH_4, 10.0% N_2, 5% He,10% CO_2

The average particle size of the adsorbent was much smaller than for previous tests, with particles in a range of 5-60 microns and a mode of about 17 microns, as measured by laser diffraction.

As with previous tests, a gas chromatograph (GC) was used to analyze the gas composition in the adsorbent bed voids after allowing the composition to equilibrate for >16 hours. This gas

composition was analyzed from multiple 0.05 ml volume samples taken by syringe through a septum. The syringe was first purged with a 0.05 ml sample which was then discarded. Eight GC samples were then taken and the results averaged for each data point (i.e. each equilibration cycle) at each location (i.e. top and bottom).

The differential adsorption results on the new proprietary adsorbent for the pure component gases are shown in Table 23. Note that the adsorbent selectively adsorbs methane over nitrogen (ratio of 2.3:1 at 100 psig and 3:1 at 50 psig) and selectively adsorbs methane over helium (ratio of 35:1 at 100 psig and 56:1 at 50 psig).

		pure He	pure He	pure CH4	pure CH4	pure N2	pure N2
Total time equilibrated	hh:mm	0:13	0:05	0:08	0:17	0:10	0:09
adsorbent type		proprietary adsorbent	proprietary adsorbent	proprietary adsorbent	proprietary adsorbent	proprietary adsorbent	proprietary adsorbent
assumed void fraction		0.35	0.35	0.35	0.35	0.35	0.35
target high temperature	°C	70	70	70	70	70	70
target low temperature	°C	20	20	20	20	20	20
adsorbent bed initial P at T hot	(psig)	**50.5**	**100.3**	**50.7**	**100.5**	**50.2**	**100.2**
total differential moles adsorbed/gram adsorbent		**3.36E-05**	**7.62E-05**	**1.89E-03**	**2.66E-03**	**6.32E-04**	**1.14E-03**

Table 23. Differential adsorption capacity of pure gases on new proprietary adsorbent.

The differential adsorption results on the new proprietary adsorbent for the baseline and high CO_2 pre-mixed gases are shown in Table 24. Note the excellent agreement between top and bottom samples, suggesting that the equilibration time was sufficient. Also note that the proprietary adsorbent has a much higher total differential capacity than activated carbon (40-80% higher than PICA and Calgon carbons) at this condition, but the selectivity is low, similar to the activated carbon (~1.6 separation factor).

.

		Baseline premix - top sample	Baseline premix - bottom sample	baseline premix	Baseline w/High CO2 top sample	Baseline w/High CO2 bottom sample	Baseline w/HIGH CO2
Total time equilibrated	hh:mm	17:59	17:59	21:56	16:53	16:53	21:32
adsorbent type		proprietary adsorbent	proprietary adsorbent	Calgon, 80-100 mesh	proprietary adsorbent	proprietary adsorbent	Calgon, 80-100 mesh
assumed void fraction		0.35	0.35	0.35	0.35	0.35	0.35
target high temperature	°C	70	70	70	70	70	70
target low temperature	°C	20	20	20	20	20	20
adsorbent bed initial P	psig	101.1	101.1	100.1	100.4	100.4	100.0
Feed gas composition							
mole % CH4		80.0%	80.0%	80.0%	75.0%	75.0%	75.0%
mole % N2		15.0%	15.0%	15.0%	10.0%	10.0%	10.0%
mole % CO2		0.0%	0.0%	0.0%	10.0%	10.0%	10.0%
mole % O2		0.0%	0.0%	0.0%	0.0%	0.0%	0.0%
mole % He		5.0%	5.0%	5.0%	5.0%	5.0%	5.0%
total differential moles adsorbed/gram adsorbent	mol/g	**1.79E-03**	**1.79E-03**	**9.87E-04**	**1.99E-03**	**1.99E-03**	**1.09E-03**
Adsorbed gas composition							
mole % CH4		83.3%	83.1%	84.2%	76.7%	76.8%	76.6%
mole % N2		14.2%	14.1%	13.4%	9.5%	9.3%	8.7%
mole % CO2		0.0%	0.0%	0.0%	11.1%	11.4%	10.7%
mole % O2		-0.1%	-0.1%	0.0%	-0.1%	-0.1%	0.0%
mole % He		0.8%	1.7%	2.4%	2.6%	2.8%	4.4%
CH_4/N_2 separation factor	(alpha)	**1.59**	**1.62**	**1.75**	**1.45**	**1.62**	**1.68**

Table 24. Differential adsorption capacity of gas mixtures on new proprietary adsorbent.

Conclusions

Thermal models of the microchannel thermal swing adsorption unit based on the use of a phase change heat exchange fluid offers new promise for the use of powder adsorbent beds. The addition of adsorption to the thermal models shows that the sweet spot for thermal conductivity is greater than 0.5 W/m-K, but that lower values are acceptable with the use of additional adsorbent.

For the powder adsorbent bed with a low thermal conductivity, on the order of 0.18 W/m-K, an adsorbent gap in the range of 0.02 inch to 0.06 inch appear feasible for complete thermal cycle times of 3 to 6 seconds or longer.

A new test stand and methodology for evaluating differential capacity for adsorbents with feed impurities has been developed.

The impact of O2 and CO2 had little impact on the differential capacity or selectivity of the tested adsorbents. However, the current measurements of selectivity are considerably lower than originally measured with the adsorbent. The root cause of this deviation is under evaluation.

Based on the PICA carbon results at 50, 100, and 140 psig, the composition of gas adsorbed appears to be independent of the pressure of the system in this range. The total number of moles of gas adsorbed, on the other hand, increases with increasing pressure.

References

Papers

Barton, T, L Bull, W Klemperer, D Loy, B McEnaney, M Misono, P Monson, G Pez, G Scherer, J Vartuli, O Yaghi, 1999, Tailored Porous Materials: Chem. Mater., v. 11, p. 2633-2656.
Ref ID: M14

Braeuer, P, M Salem, P Harting, K Quitzsch, 1997, Calculation of single adsorption isotherms from gravimetrically measured binary gas mixture adsorption isotherms on activated carbon at high pressures: Separation and Purification Technology, v. 12, p. 255-263.
Ref ID: M48

Buczek, B, 2000, Development of texture of carbonaceous sorbent for use in methane recovery from gaseous mixtures: Inzynieria Chemiczna I Procesowa, v. 21, p. 385-392.
Ref ID: M20

Buczek, B, 2000, Development of texture of carbonaceous sorbent for use in methane recovery from gaseous mixtures: Inzynieria Chemiczna I Procesowa, v. 21, p. 385-392.
Ref ID: M40

Chihara, K, K Sugizaki, N Kato, H Miyajima, Y Takeuchi, 1996, Control of adsorption rate on zeolite by chemical vapor deposition: Fundamentals of Adsorption, Kluwer Academic Pualishers, p. 179-185.
Ref ID: M13

Choi, BU, D K Choi, Y W Lee, B K Lee, S H Kim, 2003, Adsorption equilibria of methane, ethane, ethylene, nitrogen, and hydrogen onto activated carbon: Journal of Chemical and Engineering Data, v. 48, p. 603-607.
Ref ID: M23

Clarkson, CR, R M Bustin, 1999, The effect of pore structure and gas pressure upon the transport properties of coal: a laboratory and modeling study. 1. Isotherms and pore volume distributions: Fuel, v. 78, p. 1333-1344.
Ref ID: M45

Cracknell, R, D Nicholson, S Tennison, S Chopra, 1996, Adsorption and selectivity of carbon dioxide with methane and nitrogen in slit-shaped carbonaceous micropores: simulation and experiment: Adsorption, v. 2, p. 193-203.
Ref ID: M5

Davies, GM, N A Seaton, 1999, Development and validation of pore structure models for adsorption in activated carbons: Langmuir, v. 15, p. 6263-6276.
Ref ID: M44

Dong, F, H M Lou, A Kodama, M Goto, T Hirose, 1999, A new concept in the design of pressure-swing adsorption processes for multicomponent gas mixtures: Industrial & Engineering Chemistry Research, v. 38, p. 233-239.
Ref ID: M46

Fatehi, A, K Loughlin, M Hassan, 1995, Separation of Methane-nitrogen mixtures by pressure swing adsorption using a carbon molecular sieve: Adsorption Science and Technology, v. 9, p. 199-204.
Ref ID: M3

Fuertes, A, 2001, Preparation and characterization of adsorption-selective carbon membranes for gas separation: Adsorption, v. 7, p. 117-129.
Ref ID: M11

Gomes, VG, M M Hassan, 2001, Coalseam methane recovery by vacuum swing adsorption: Separation and Purification Technology, v. 24, p. 189-196.
Ref ID: M37

Harlick, PJE, F H Tezel, 2002, Adsorption of carbon dioxide, methane, and nitrogen: Pure and binary mixture adsorption by ZSM-5 with SiO2/Al2O3 ratio of 30: Separation Science and Technology, v. 37, p. 33-60.
Ref ID: M35

Heuchel, M, G M Davies, E Buss, N A Seaton, 1999, Adsorption of carbon dioxide and methane and their mixtures on an activated carbon: Simulation and experiment: Langmuir, v. 15, p. 8695-8705.
Ref ID: M43

Hoover, RP, P C Wankat, 2002, Gas compression using temperature swing adsorption: Separation Science and Technology, v. 37, p. 3187-3199.
Ref ID: M28

Huang, QL, S M Sundaram, S Farooq, 2003, Revisiting transport of gases in the micropores of carbon molecular sieves: Langmuir, v. 19, p. 393-405.
Ref ID: M26

Huang, QL, S Farooq, I A Karimi, 2003, Binary and ternary adsorption kinetics of gases in carbon molecular sieves: Langmuir, v. 19, p. 5722-5734.
Ref ID: M51

Jacquinot, P, B Muller, B Wehrli, P C Hauser, 2001, Determination of methane and other small hydrocarbons with a platinum-Nafion electrode by stripping voltammetry: Analytica Chimica Acta, v. 432, p. 1-10.
Ref ID: M38

Jayaraman, A, A S Chiao, J Padin, R T Yang, C L Munson, 2002, Kinetic separation of methane/carbon dioxide by molecular sieve carbons: Separation Science and Technology, v. 37, p. 2505-2528.
Ref ID: M32

Kluson, P, S Scaife, N Quirke, 2000, The design of microporous graphitic adsorbents for selective separation of gases: Separation and Purification Technology, v. 20, p. 15-24.
Ref ID: M41

Kulkarni, M, C Sardesai, 2002, Enrichment of methane concentration via separation of gases using vortex tubes: Journal of Energy Engineering, p. 1-12.
Ref ID: M15

Melnitchenko, A, J Thompson, C Volzone, J Ortiga, 2000, Selective gas adsorption by metal exchanged amorphous kaolinite derivatives: Applied Clay Science, v. 17, p. 35-53.
Ref ID: M10

Mentasty, L, A Woestyn, E Basaldella, A Kikot, G Zgrablich, 1994, High-Pressure Methane adsorption on NaX and NaY zeolites wiht different Si/Al ratios: Adsorption Science and Technology, v. 11, p. 209-216.
Ref ID: M2

Mogri, Z, D Paul, 2001, Gas sorption and transport in side-chain crystalline and molten poly(octadecyl acrylate): Polymer, v. 42, p. 2531-2542.
Ref ID: M17

Molina-Sabio, A, C Almansa, F Rodriguez-Reinoso, 2003, Phosphoric acid activated carbon discs for methane adsorption: Carbon, v. 41, p. 2113-2119.
Ref ID: M50

Olajossy, A, A Gawdzik, Z Budner, J Dula, 2003, Methane separation from coal mine methane gas by vacuum pressure swing adsorption: Chemical Engineering Research & Design, v. 81, p. 474-482.
Ref ID: M24

Park, J, J-N Kim, S Cho, J-D Kim, R Yang, 1998, Adsorber dynamics and optimal design of layered beds for multicomponent gas adsorption: Chemical Engineering Science, v. 53, p. 3951-3963.
Ref ID: M9

Park, JH, H T Beum, J N Kim, S H Cho, 2002, Numerical analysis on the power consumption of the PSA process for recovering CO2 from flue gas: Industrial & Engineering Chemistry Research, v. 41, p. 4122-4131.
Ref ID: M31

Pires, J, 2001, Textural and surface chemistry characterization of zeolites via adsorption phenomena: Handbook of Surfaces and Interfaces of Materials, ed HS Nalwa, p. 481-507.
Ref ID: M7

Predescu, L, F H Tezel, S Chopra, 1996, Adsorption of Nitrogen, Methane, Carbon Monoxide, and their binary mixtures on aluminophospahe molecular sieves: Adsorption, v. 3, p. 7-25.
Ref ID: M1

Puziy, AM, O I Poddubnaya, B Gawdzik, M Sobiesiak, D Dziadko, 2002, Heterogeneity of synthetic carbons obtained from polyimides: Applied Surface Science, v. 196, p. 89-97.
Ref ID: M29

Puziy, AM, A Herbst, O I Poddubnaya, J Germanus, P Harting, 2003, Modeling of high-pressure adsorption using the bender equation of state: Langmuir, v. 19, p. 314-320.
Ref ID: M25

Qinglin, H, S Sundraram, S Farooq, 2003, Revisiting Transport of Gases in the Micropores of Carbon Molecular Sieves: Langmuir, v. 19, p. 393-405.
Ref ID: M49

Quinn, DF, 2002, Supercritical adsorption of “permanent” gases under corresponding states on various carbons: Carbon, v. 40, p. 2767-2773.
Ref ID: M27

Rittig, F, D J Aurentz, C G Coe, R J Kitzhoffer, J M Zielinski, 2002, Pure- and mixed-gas sorption measurements on zeolitic adsorbents via gas-phase nuclear magnetic resonance: Industrial & Engineering Chemistry Research, v. 41, p. 4430-4434.
Ref ID: M30

Roualdes, S, J Sanchez, J Durand, 2002, Gas diffusion and sorption properties of polysiloxane membranes prepared by PECVD: Journal of Membrane Science, v. 198, p. 299-310.
Ref ID: M12

Sakoda, A, N Oka, F H Tezel, 1996, Adsorption of methane onto activated carbon by a graphite crystal aggregate model: Adsorption Science and Technology, p. 781-788.
Ref ID: M4

Salem, MMK, P Braeuer, M von Szombathely, M Heuchel, P Harting, K Quitzsch, M Jaroniec, 1998, Thermodynamics of high-pressure adsorption of argon, nitrogen, and methane on microporous adsorbents: Langmuir, v. 14, p. 3376-3389.
Ref ID: M21

Sudibandriyo, M, Z J Pan, J E Fitzgerald, R L Robinson, E A M Gasem, 2003, Adsorption of methane, nitrogen, carbon dioxide, and their binary mixtures on dry activated carbon at 318.2 K and pressures up to 13.6 MPa: Langmuir, v. 19, p. 5323-5331.
Ref ID: M22

Sun, J, S Chen, M Rood, M Rostam-Abadi, 1998, Correlating N2 and CH4 adsorption on microporous carbon using a new analytical method: Energy and Fuels, v. 12, p. 1071-1078.
Ref ID: M8

Sun, J, S Chen, M Rostam-Abadi, M Rood, 1998, Predicting CH4 adsorption capacity of microporous carbon using N2 isotherm and a new analytical model: American Chemical Society, Division of Fuel Chemistry, v. 43, p. 596-600.
Ref ID: M18

Sweatman, MB, N Quirke, 2001, Characterization of porous materials by gas adsorption at ambient temperatures and high pressure: Journal of Physical Chemistry B, v. 105, p. 1403-1411.
Ref ID: M39

Takeuchi, Y, Y Suzuki, M Shimoyama, 1993, Production of tasty drinking water by activated carbon adsorption followed by contact with some natural ores: 6th conference Asia Pac.Confed.Chem.Eng.21st Autralas, Chem Eng Conf, p. 527-532.
Ref ID: M19

Uraki, Y, R Taniwatashi, S Kubo, Y Sano, 2000, Activated carbon sheet prepared from softwood acetic acid lignin: Journal of Wood Science, v. 46, p. 52-58.
Ref ID: M42

Ustinov, EA, D D Do, A Herbst, R Staudt, P Harting, 2002, Modeling of gas adsorption equilibrium over a wide range of pressure: A thermodynamic approach based on equation of state: Journal of Colloid and Interface Science, v. 250, p. 49-62.
Ref ID: M33

Wang, H, B Mattes, 1999, Gas transport and sorption in polyaniline thin films: Synthetic Metals, v. 102, p. 1333-1334.
Ref ID: M16

Warmuzinski, K, W Sodzawiczny, 1999, Effect of adsorption pressure on methane purity during PSA separations of CH4/N-2 mixtures: Chemical Engineering and Processing, v. 38, p. 55-60.
Ref ID: M47

Yun, JH, T Duren, F J Keil, N A Sexton, 2002, Adsorption of methane, ethane, and their binary mixtures on MCM-41: Experimental evaluation of methods for the prediction of adsorption equilibrium: Langmuir, v. 18, p. 2693-2701.
Ref ID: M34

Zhou, L, M Hassan, Y Zhou, 2002, A feasibility study of separating CH4/N2 by adsorption: Chinese Journal of Chemical Engineering, v. 10, p. 558-561.
Ref ID: M6

Zhou, YP, S P Bai, L Zhou, B Yang, 2001, Studies on the physical adsorption equilibria of gases on porous solids over a wide temperature range spanning the critical region-adsorption on microporous activated carbon: Chinese Journal of Chemistry, v. 19, p. 943-948.
Ref ID: M36

Patents

Butwell, K, W Dolan, S Kuznicki. Selective removal of nitrogen from natural gas by pressure swing adsorption. Engelhard. [6,197,092]. 2001.
Ref ID: M63

Butwell, K, W Dolan, S Kuznicki. Pressure Swing Adsorption Processes. Engelhard. [6,497,750]. 2002.
Ref ID: M64

Davis, M, R Gray, K Patel. Process for the purification of natural gas. UOP. [5,174,796]. 1992.
Ref ID: M58

Dolan, W, K Butwell. Selective removal of nitrogen from natural gas by pressure swing adsorption. Engelhard. [6,444,012]. 2002.
Ref ID: M62

Golden, T, A Schwarz, T Hsiung, F Taylor. Purification of gases. Air Products. [6,093,379]. 2000.
Ref ID: M69

Ivey, D, T Hoffman. Activated carbon for separation of fluids by adsorption and method for its preparation. Norit Americas, Inc. [5,726,118]. 1998.
Ref ID: M54

Kirner, J. Nitrogen adsorption wiht highly Li exchanged x-zeolites with low Si/Al ratio. Air Products. [5,268,023]. 1993.
Ref ID: M52

Kuznicki, S, V Bell, I Petrovic, P Blosser. Separation of nitrogen from mixtures thereof with methane utilizing barium exchanged ETS-4. Engelhard. [5,989,316]. 1999.
Ref ID: M70

Moreau, S, B Sardan. Process for separating nitrogen from less polar compounds. Air Liquide. [6,336,956]. 2002.
Ref ID: M53

Nelson, W. Adsorption process for natural gas purification. Al E.& C.Ltd. [3,710,547]. 1973.
Ref ID: M55

Putyera, K, C Contescu, K Amankwah, W Amato. Post-carbonization treatment of microporous carbons for enhancement of methane and natural gas storage properties. Niagara Mohawk Power Corporation. [6,225,257]. 2001.
Ref ID: M65

Raatz, F, L Petit, C Marcilly, J Bournonville, C Travers, P Dufresne. Decationized, dealuminated, and stabilized L zeolite and use thereof. Institut Francais du Petrole. [4,909,924]. 1990.
Ref ID: M61

Reinhold, H, K Knaebel, M Huber, D King. Separation of gases by pressure swing adsorption. Nitrotec Corporation. [5,792,239]. 1998.
Ref ID: M57

Schimp, C. Method and apparatus for recovering and transporting methane mine gas. Schimp. [6,205,793]. 2001.
Ref ID: M60

Schwarz, J, J Noh, R Agarwal. Selection and preparation of activated carbon for fuel gas storage. Syracuse University. [4,960,450]. 1990.
Ref ID: M59

Schwarz, J, K Putyera, J Jagiello, T Bandosz. Activated carbons molecularly engineered. Syracuse University. [5,385,876]. 1995.
Ref ID: M68

Schwarz, J, K Putyera, T Bandosz, J Jagiello. Microporous carbons for fuel gas storage. Syracuse University. [5,614,460]. 1997.
Ref ID: M66

Schwarz, J, K Putyera, T Bandosz, J Jagiello, K Amankwah. Composite microporous carbons for fuel gas storage. Syracuse University. [5,837,741]. 1998.
Ref ID: M67

Other

EPA, Coalbed Methane Outreach Program Study, *Technical and Economic Assessment of Potential to Upgrade Gob Gas to Pipeline Quality*, 1997.

King, C.J., Separation Processes, McGraw Hill, New York, p. 29, 1980.

Phase 2. Technical Results

Experiments

Several experimental test stands were designed, assembled and adopted to validate the use of absorption for the separation of methane from a mixed species vapor stream. A batch test stand allowed direct measurement of methane solubility in a small quantity of ionic liquid. The same stand was successfully and repeatedly used for ionic liquid regeneration. A continuous flow, microchannel stand was adopted to absorb methane into a co-currently flowing ionic liquid stream, a single channel process directly scalable to eventual industrial application. A second, specifically designed flow through absorption unit, with a stacked foam assembly, was used for semi-batch testing, allowing flow through and enhanced interfacial contacting with limited ionic liquid consumption.

Batch Device and Test Stand

A batch device and test stand were designed and assembled to allow direct and fast measurement of the absorption capacity of available absorbing fluids. This information provides feedback that is key to the development of a platform to maximize absorption performance in an absorption-desorption cycle.

The Piping and instrumentation diagram for the batch stand assembly is shown in Figure 1.

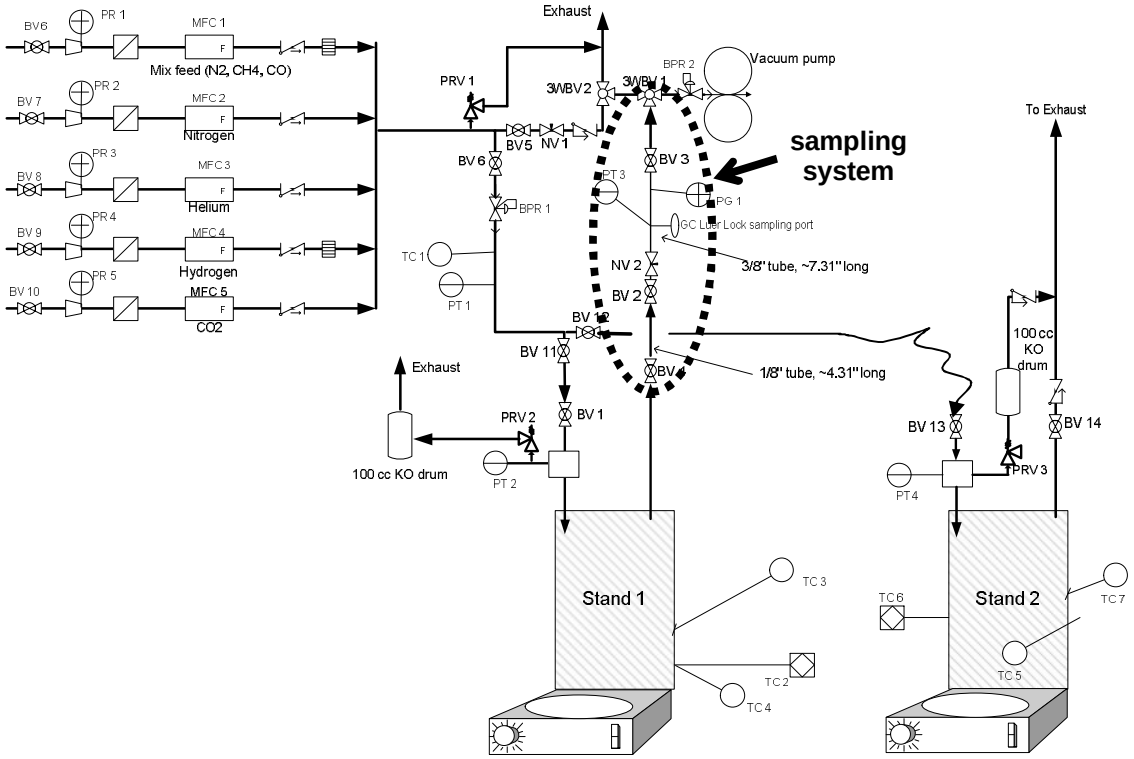

Figure 1. Piping and Instrumentation Diagrams for the batch test stand.

Currently, the batch test stand allows two simultaneous absorption measurements using two separate devices. Two mixing/heating plate stations are dedicated to the test stand. One station serves as the main gas feed and headspace test station. The secondary station allows a second device to be simultaneous purged and filled with a common gas feed stream. If two devices are tested simultaneously with different gas feed streams, they are independently filled and sealed at the main station. In all cases, because headspace measurement requires tight volume controls, all devices have to be directly attached to the main station during headspace testing.

Figure 2. Batch device.

Figure 2 shows a picture of the device and Figure 3 the assembly and exploded schematics that detail port locations and functions. The batch device has an overall internal volume of 140 cc. A magnetic stir bar and the test liquid are added and removed through the liquid port. In the loading process, care is taken to ensure that the liquid level does not contact the bottom of the gas inlet port tube, which extends 12.7 mm below the top of the chamber. Free access of gas through the offset gas ports ensures thorough headspace purging, loading and testing during operation. A thermowell extends 12.5 mm into the center of the device, allowing direct measurement of the liquid bath temperature without disrupting the motion of the stir bar as it rotates on the bottom surface of the device. Bath temperature measurement feeds directly back to the mixer/heating plate control to ensure the operating temperature adheres to the required setting. Two ports branch out from the main gas inlet port to allow pressure relief and measurement during operation. Temperature and pressure are constantly monitored; values collected at periodic intervals, using the Labview software, allow complete mapping of operational profiles. The device has been designed to withstand up to 900 psig at 100 °C, up to 850 psig at 200 °C. All components are SS316; the liquid port gasket is made of VITON. If material compatibility requires, the gasket can be made of different materials, as well.

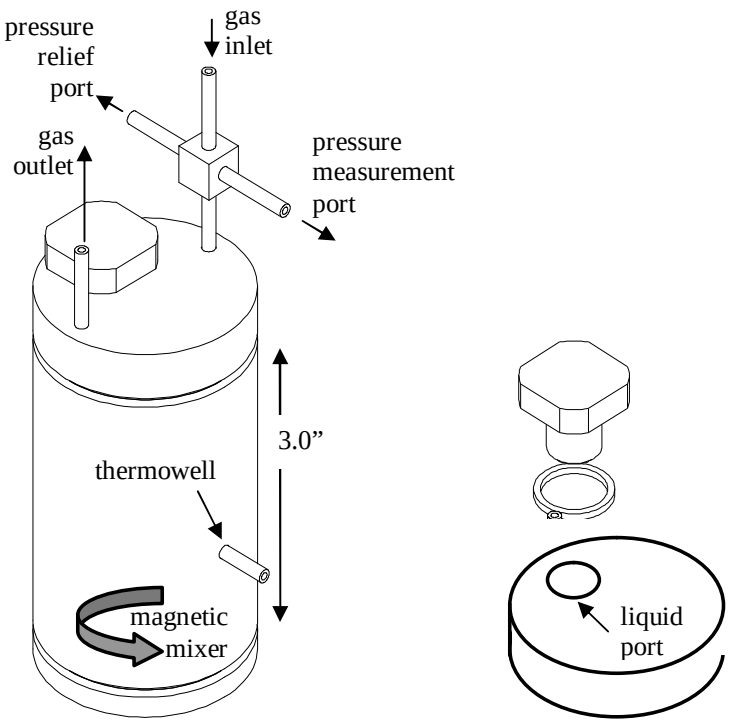

Figure 3. Schematics of the batch testing device: left picture shows the welded device and provides some functional details; right picture shows an exploded view of the liquid port and sealing cap.

All vapor flows are regulated using Brooks thermal mass flow controllers. Temperature and pressure are measured with Omega thermocouples and NoShok pressure transducers, respectively. Two gas chromatographs have been used to date: a Shimadzu and an Agilent gas chromatograph, both well suited to our measurement needs.

Batch Testing Protocol

Mass flow controllers, pressure transducers and gas chromatograph are calibrated before each test to ensure accuracy in the operation range of interest. The gas chromatograph is calibrated using gases from Matheson Tri-Gas. Prior to filling and operation, the complete system is leak checked with hydrogen.

Test feed gas compositions are set and measured before beginning each test. When available, premixed streams are fed through single controllers. Otherwise, multiple mass flow controllers are preset to provide the required species feed ratios.

If unknown, the density of the liquid is measured by weighing the contents of a 10 cc volumetric flask filled with the test liquid. As needed, liquid viscosity is also measured, using a Brookfield viscometer, to clarify expectations relating to ease of species diffusion and mixing effectiveness during testing.

At the onset of testing, the test liquid is poured into the device to a predefined level. The mass of liquid in the chamber is measured and used to define the liquid fill volume more accurately. The

device is sealed and connections are made to begin testing. The specific testing and purging procedures are outlined below.

Batch Testing Procedure

1. Verify mixing system is off in test device.
2. Flush system and test device at ambient pressure with inert gas (preferably, the inert gas should not be in the test gas mixture).
3. Allow enough time to purge the headspace volume eight times, maintaining the gas flow rate low enough so as to not blow liquid through the gas outlet port.
4. Switch feed to the test gas composition.
5. Allow enough time to purge the headspace volume eight times, maintaining the gas flow rate low enough so as to not blow liquid through the gas outlet port.
6. Close device exit valves and allow pressure to build.
7. Once desired pressure is reached, stop flow to device and close inlet valves.
8. Turn on the magnetic mixing system and let the stirring occur at 700rpm. Monitor the test device temperature and pressure.
9. Once the system pressure has stabilized, showing a loss rate approximately equal to the leak rate of the system, turn off the mixing system and take a headspace sample with the sampling system.
10. Operate the sampling system (Figure 2 shows the purge and filling locations):

    Purge the complete sampling system volume to avoid headspace contamination.

    a. Detach the sampling system from the device and let a pure helium stream purge the sampling system. Purge so as to displace the complete sampling system volume at least 8 times.
    b. Reattach the sampling system to the device.
    c. Vacuum the complete sampling system to approximately -30 inHg.

    Remove the stagnant gas layer that is not necessarily representative of the main device headspace volume and purge the complete sampling system once more.

    d. Isolate the upstream and downstream sections of the sampling system from each other.
    e. Open the valve connecting the device to the sampling system, let the pressures equilibrate, and re-close the connecting valve.
    f. Repeat Steps a through d. (Steps d through f remove the stagnant gas layer that may not be representative of the main device headspace.)

    Draw and isolate enough representative headspace volume from the device to perform at least 3 concentration measurements.

    g. Open the valve connecting the device to the sampling system, let the pressures equilibrate, and re-close the connecting valve.
    h. Open the valve connecting upstream and downstream sections of the sampling system, reducing the pressure of the sampling system as the gas expands to fill the larger volume. Re-close the valve connecting the upstream and downstream sections of the sampling system.
    i. Repeat Steps g through h until the sampling system pressure reaches 12 psig.

    Repeatedly measure the concentration of species in the sampling system.

j. Use the septum in the downstream section of the sampling system to withdraw approximately 150 μL of gas and inject into the gas chromatograph.
k. Repeat step j at least 3 times, or until sufficiently similar results are obtained.

11. Continue testing and sampling, as necessary.

Batch Regeneration Procedure

1. The stirring mechanism is shut off.
2. The device pressure is released to the atmosphere (slowly enough to ensure no liquid blow-over).
3. A flow of pure hydrogen gas is let pass through the device for headspace purging, and the stirring mechanism is turned back on to 350 rpm.
4. The heating mechanism is turned on and the temperature of the device is slowly and manually ramped to 45°C.
5. Constant temperature mixing and headspace purging continue for at least 6hrs.
6. The heating mechanism is shut off at the end of the day (while mixing and purging with hydrogen continue).
7. Steps 4 through 6 are repeated.
8. Absorption testing is begun no more than 24 hours after the Step 7.

If Step 8 cannot occur, the regeneration process is restarted before proceeding with the testing.

When available, absorption estimates (from literature or prior testing) are referenced to define headspace species concentration changes expected over the course of the test for the predefined headspace volume. These are used to ensure the likelihood that significantly different concentration measurements will be obtained at the beginning and end of the test. As noted in Steps 10g through 10i in the Batch Testing Procedure, headspace pressure needs to be sufficiently high to provide enough sampling volume for measurements over the course of the test.

The purging and regeneration protocols developed to date have provided significant reproducibility in the results for all liquid-gas combinations tested. Pure helium serves as the purging gas in the sampling system as long as it is not a component in the test gas mixture (avoiding potential for interference with the test response) and because of its inertness and nonflammable nature (allowing use of the vacuum pump). Hydrogen is used as the headspace purging gas because of its relative inertness with the liquids tested to date.

Calculation Methodology for the Batch Experiments

Estimates of Henry's constants are based on experimental measurements of headspace concentrations. Generally the procedure for the calculation involves the following steps:

- identifying the headspace volume, V_{vapor}
- identifying the initial and final pressure, P, temperature, T, and species concentrations, y_i, in the headspace

- calculating the initial and final moles of each species, n_i, in the headspace using the data identified above, assuming ideal gas behavior (R is the ideal gas constant)

$$n_i = \frac{y_i P V_{vapor}}{RT}$$

- calculating the moles of each species absorbed by the liquid, $n_{i\ absorbed}$, by subtracting the final from the initial moles in the headspace

$$n_{i\ absorbed} = n_{i\ initial} - n_{i\ final}$$

- estimating Henry's constant for each species, H_i, using the following equation,

$$H_i = \left.\frac{P y_i}{x_i}\right|_{final}$$, where x_i, the mole fraction of species i in the liquid, is calculated as follows,

$$x_i = \frac{n_{i\ absorbed}}{\left[n_{liquid} + \sum_i n_{i\ absorbed} \right]}.$$

The liquid volume is assumed to be unchanged in the process of absorption.

Continuous Flow Microchannel Device and Test Stand

Experimental results from the batch absorption trials were supplanted by microchannel flow through experiments, adopting the test stand configuration shown in Figure 4.

The continuous flow configuration allows co-current contacting of mixed vapor and liquid streams in a microchannel. The high interfacial area and the short diffusion distances that are inherent to microchannel processing lead to very fast and efficient mass transfer between streams.

The experimental test stand was designed for versatility, allowing handling and processing of a wide range of liquid absorbents and gaseous stream compositions, flow rates, and temperatures. Ports, distributed along the length of the 30.5 cm-long microchannel, allow fast changes in feed location, potential staggering of feed streams and feed compositions, and pressure transducer placement to fit specific run needs. Metal system components are 316 stainless steel; all soft components are compatible with the ionic liquids.

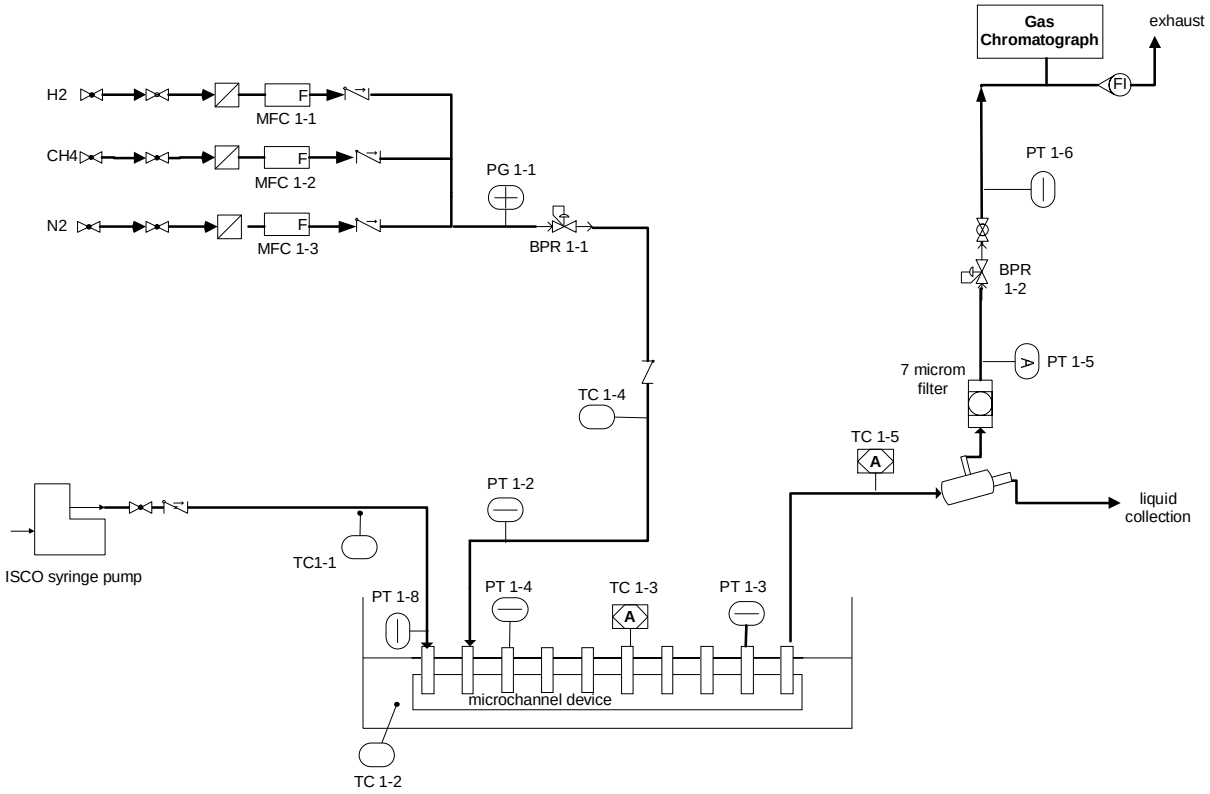

Figure 4. Piping and Instrumentation Diagram of the microchannel test stand.

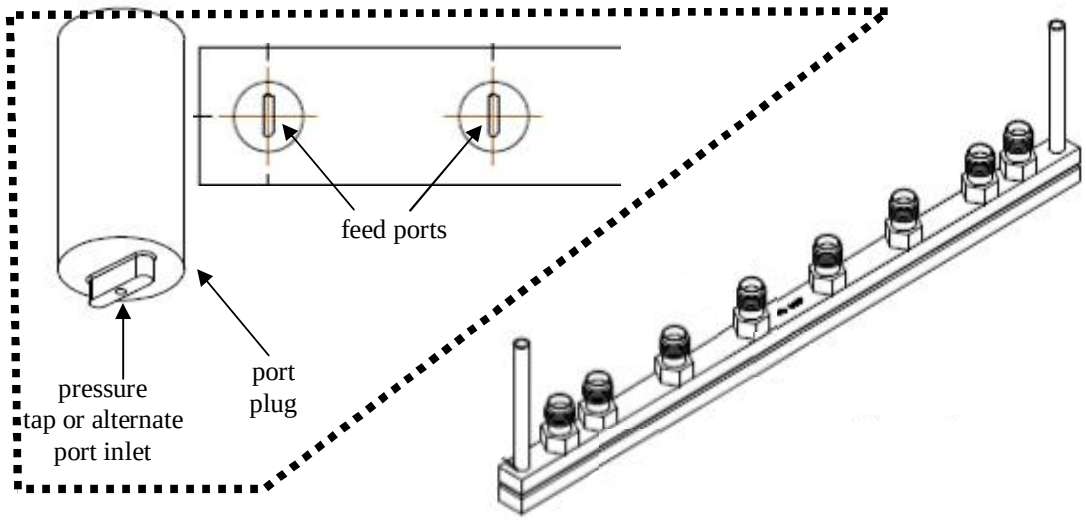

Figure 5. Schematic of the microchannel device. Liquid and vapor streams enter the device through ports along the device axis, flow co-currently, and exit the device through a single outlet port. The internal channel may be flat or incorporate surface features to promote mixing and interaction of the gas and liquid streams.

A schematic of the microchannel device is shown in Figure 5. The feed ports, shown in the inset, are 1.02 mm-wide and span the width of the main channel, rendering the feed and stream merging uniform. The specifically designed plugs fit flush with the internal main channel surface and minimize disruption in the main flow path. A 0.25 mm diameter hole in the center of

each plug allows pressure measurement or serves as an alternate means of introducing the feed. The device can be assembled as a flat channel or to incorporate mixing features embedded in the walls, as shown in Figure 6. Some results with computational fluid dynamics (CFD), shown in Figure 7, suggest enhanced phase mixing resulting from the use of embedded floor mixing features within the microchannel. The improved mixing increases interfacial area and the ease of achieving the targeted dissolution of the methane in the ionic liquid.

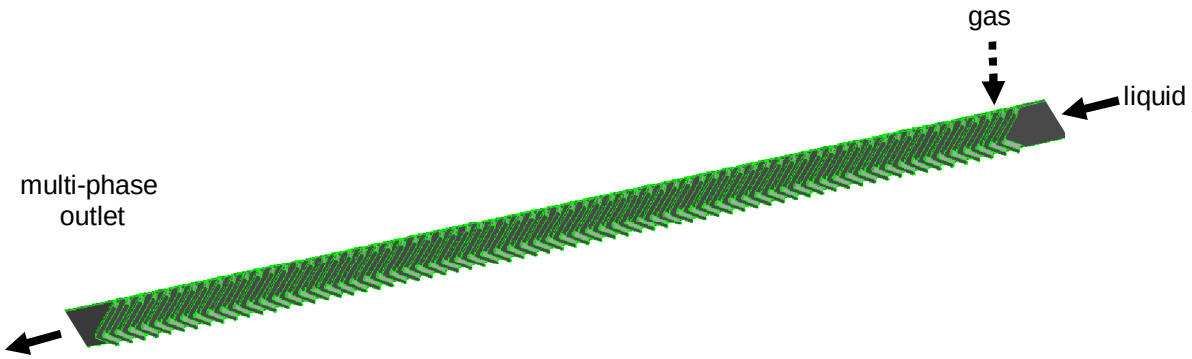

Figure 6. Schematic of the embedded mixing features in the microchannel device to improve interfacial area and increase mass transfer between the phases. The floor of the microchannel contains an array of parallel mixing features that act to push and pull the fluid and create small bubbles with high interfacial area. The multiphase mixture flows in the open channel above the floor features.

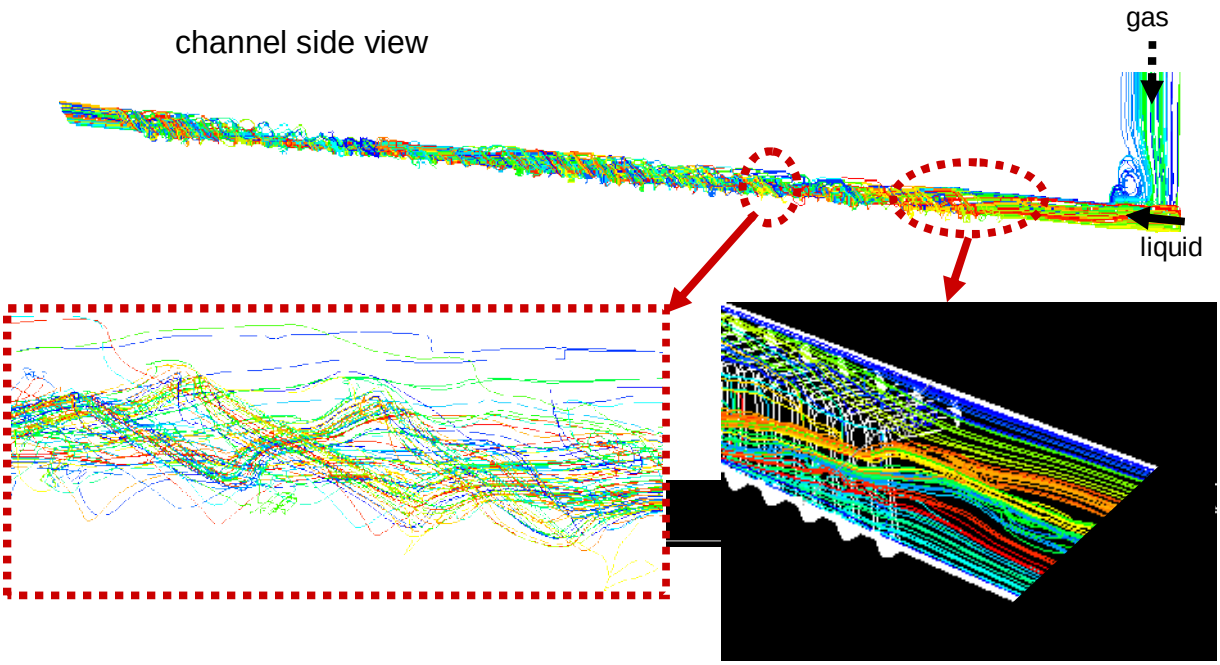

Figure 7. Computational Fluid Dynamics simulation of the flow patterns (as shown by fluid path lines that trace the movement) during the mixing of a gas and liquid in the microchanel contacting device. The otherwise straight laminar flow patterns are broken suggesting enhanced phase mixing.

As is shown in the Piping and Instrumentation Diagram, Figure 4, the microchannel device is mounted horizontally in a temperature regulated water bath. The device is capable of withstanding up to 1800 psig at 150 °C. Omega thermocouples, placed in the inlet and outlet

flow paths, allow measurement of temperature changes during operation. Pressure transducers are used to measure process pressures and pressure drops. Temperatures and pressures are constantly monitored and the values periodically collected using the Labview 7.1 data acquisition software allow complete mapping of operational profiles.

Vapor feed flows are regulated by Brooks Thermal mass flow controllers. The liquid is fed by an ISCO high pressure syringe pump. Testing can be performed with single phases or multiphase mixtures. As currently configured, all streams exit the device through the same exit port. During multiphase operation, the liquid and vapor are separated in a knock-out drum immediately downstream of the exit port. Whether operated as a single or multi-phase system, vapor and liquid are always let flow out of the knockout drum. Liquid is always removed through the lower line in the knock-out pot and let flow into a collection vessel. A needle valve controls the removal of gas from the headspace of the collection vessel to the atmosphere. In a multiphase run, vapor is removed through the upper port in the knock-out pot. The headspace in the liquid collection vessel is connected to the vapor exit line to ensure pressure equilibration and free flow and removal of liquid from the knock-out pot into the collection vessel. A back pressure regulator, downstream of the vapor headspace connection line, controls system pressure.

The back pressure regulator reduces the pressure of the vapor stream from the knock-out pot as it flows towards the GC, prior to being exhausted to the atmosphere. Careful throttling of the needle valve on the collection vessel is required to ensure that the headspace from the collection vessel flows directly to exhaust without being forced back towards the GC line; this is critical to ensuring accurate measurement of the instantaneous composition of the gas stream exiting the microchannel device. Flow meters in the headspace removal line of the collection vessel and at the GC exit port help control the needle valve setting. As long as the vapor flow rate from the collection vessel exceeds the flow rate that results from vapor displacement by the liquid entering the collection vessel, the GC measurement is ensured to reflect the vapor composition in the knock-out pot.

Complete and fast purging of the knock out pot is also important to obtaining response that reflects the instantaneous composition of the vapor stream exiting the channel. A knock-out pot configuration was specifically put in place to help the purging process, as shown in Figure 8. Gas and liquids flow co-currently through the knock-out pot, leading to minimal vapor backflow and most effective headspace purging. The headspace is also held as small as possible to minimize the purge rate. Because increased pressures lead to an increase in the vapor density and a corresponding reduction in vapor flow rate, the headspace purge rate decreases with increased pressure. When conducting the tests, consideration needs to be given to the fact that the system response time decreases as the test pressure increases.

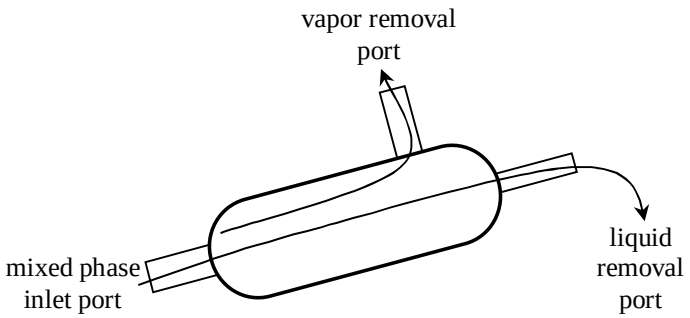

Figure 8. Schematic of the knock-out pot configuration in the microchannel test stand.

The general procedure for continuous multi-phase flow testing involves the steps outlined below. These do not include preliminary calibrations and system and valve setting checks required for safe and appropriate operation of the stand.

Continuous Flow Testing Procedure

1 Fill the ambient water bath and ensure proper placement of the bath thermocouple. Turn on the bath mixer and set the water bath temperature.
2 Synchronize the date and time of the GC and Labview computers and start Labview recording.
3 Pressurize the system to the required downstream pressure using nitrogen gas.
4 Set the feed vapor flow rate to correspond to the sum of the intended gas feed flow rate and the expected vapor compensation flow rate (to compensate for gas displacement by the flowing liquid during operation).
5 Pre-regulate the back-pressure regulator and the needle valve on the knock-out pot to let the required amounts of vapor flow from each valve (this is a rough value that is refined once the test is started).
6 Switch the gas stream to the intended mix and reduce the vapor gas feed flow rate to the required setting for the testing.
7 Start feeding liquid to the stand, beginning with a flow rate that is less than 10% of the intended test value.
8 Gradually ramp the liquid flow rate to the required setting (ensuring that the upstream pressure does not exceed the predefined safe limit).
9 Allow enough time to fill the knockout pot with liquid to the minimum required level to prevent backflow of vapor from the collection vessel to the knockout pot via the liquid exit line. This also leads to a reduction in the headspace volume of the knock-out pot and a faster knock-out pot purge rate.
10 Refine the setting of the back pressure regulator and needle valve to ensure the proper flow distribution through the exit vapor stream lines (ensuring that all of the compensation gas displaced by the flowing liquid during operation is removed through the needle valve on the knock out pot and does not feed back into the GC line).
11 Measure the vapor stream concentrations periodically and frequently throughout the testing, allowing enough time for purging of the knock-out drum headspace and equilibration of the microchannel flow system (i.e., until no more changes in the exit stream concentrations are seen).

12 Re-measure feed compositions before shutting down the stand to double-check consistency and reproducibility of the GC measurements.

Calculation Methodology for the Continuous Flow Experiments

The effectiveness of any given experimental absorption run is gauged by comparing the measured moles of each species absorbed/desorbed with the amount expected to have been absorbed/desorbed if complete saturation, as dictated by vapor-liquid equilibrium, defined with Henry's law, is achieved at the exit of the device.

Hence, the total molar flow rate and the inlet molar flow rates of each species in the system are calculated from the inlet liquid and vapor flow rates and compositions, as follows,

$$\dot{Q} = \dot{L}_{inlet} + \dot{V}_{inlet} \quad (1)$$

$$\left(\dot{m}_i = x_i \dot{L} + y_i \dot{V}\right)_{inlet}, \text{ where} \quad (2)$$

$\dot{L}, \dot{V}$ = total liquid and vapor molar flow rates,
$\dot{m}_i$ = molar flow rate of species i through the system,
$\dot{Q}$ = total molar flow rate through the system,
x_i, y_i = liquid and vapor mole fractions of species i.

The expected molar flow rates and species distributions at the exit point are calculated by simultaneous solution of the following equations:

total mass balance, $\dot{L}_{exit} + \dot{V}_{exit} = \dot{Q}$ (3)

individual species mass balances, $\left(\dot{m}_i = x_i \dot{L} + y_i \dot{V}\right)_{exit}$ (4)

Henry's law for each species in the system, $\left(H_i = \frac{P y_i}{x_i}\right)_{exit}$ (5)

molar balances for all species in the vapor phase, $\left(\sum y_i = 1\right)_{exit}$ (6)

molar balance for all species in the liquid phase, $\left(\sum x_i = 1\right)_{exit}$, where (7)

The ionic liquid is assumed to be non-volatile. All other components can move into and out of each phase.

For easy implementation into a data-logger format, an excel spreadsheet was specifically created for the calculations. Generally, it requires

- input of Henry's constants for each species,
- input of the initial vapor and liquid flow rates (in ccm and sccm, respectively),
- input of ambient and device inlet and outlet pressures and temperatures,
- input of GC measured inlet species concentrations in the vapor phase and appropriately measured inlet species concentrations in the liquid phase,
- input of the vapor flow rate exiting the test stand through both the GC line and the knock-out drum.

This information is used to explicitly calculate the inlet values of $\dot{Q}$ and $\dot{m}_i$, using Equations 1 and 2.

Equations 3 through 7 are solved simultaneously using the excel "goal seek" tool. For this,

- the vapor mole fraction of each species at the exit point is calculated by rearranging Equations 3 through 7 in terms of $\dot{V}_{exit}$ and known variables,

$$\left(y_i = \frac{\dot{m}_i}{\dot{V} + \frac{P\dot{Q}}{H_i} - \frac{P\dot{V}}{H_i}} \right)_{exit} \tag{8}$$

- an initial value for the vapor exit flow rate, $\dot{V}_{exit}$, is selected (the inlet molar vapor flow rate is a good initial estimate) and let vary to satisfy Equation 6 (in the "goal seek" function),
- and the validity of Equation 7 is checked to ensure satisfaction of all conditions.

Finally, the effectiveness of the experimental absorption run for each species, ξ_i, is calculated with the following expression:

$$\xi_i = \frac{\left[\left(y_i\dot{V}\right)_{exit} - \left(y_i\dot{V}\right)_{inlet}\right]_{measured}}{\left[\left(y_i\dot{V}\right)_{exit} - \left(y_i\dot{V}\right)_{inlet}\right]_{calculated}} 100 \text{, where} \tag{9}$$

$$\dot{V}_{exit\ measured} = \dot{V}_{exit\ GC} + \dot{V}_{exit\ KO\ drum} \tag{10}$$

Semi-Batch Devices and Test Stand

The semi-batch absorption methodology was developed because of the need to evaluate a wide range of ionic liquid alternatives and relative flow rates in continuous flow mode. Both batch and continuous flow stands support the process, which allows minimal liquid consumption but enhanced versatility.

The semi-batch experiments adopt the flow through multiphase contacting device shown in Figure 10 and a smaller version of the batch testing device, shown in Figure 11. The two devices are placed in series, as shown in the flow diagram of Figure 12.

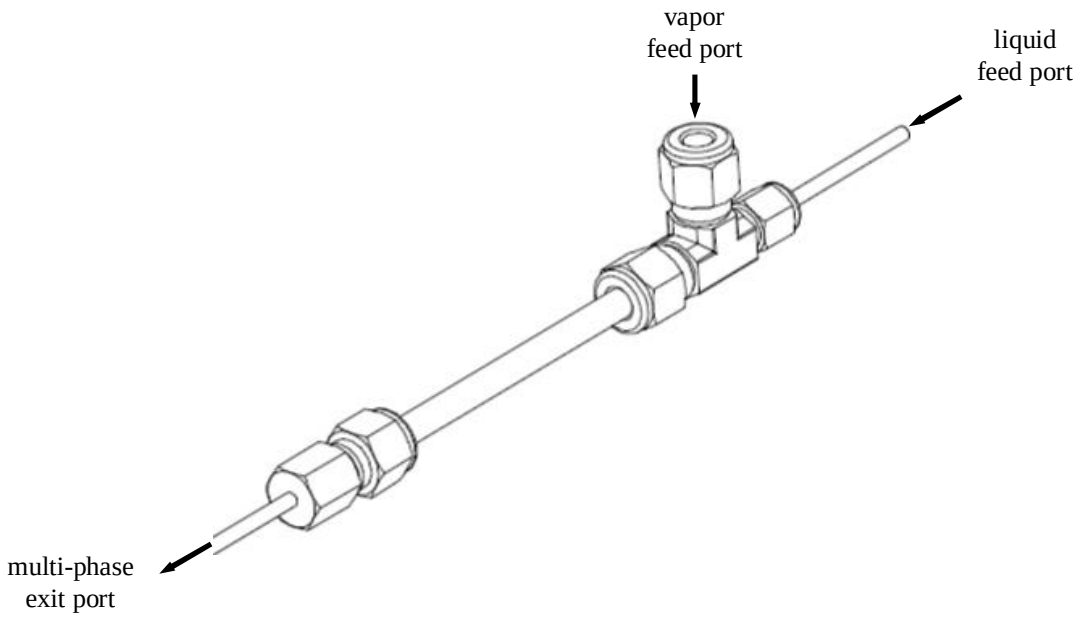

Figure 9. Diagram of the flow through multiphase contacting device.

The flow through device, shown in Figure 9, incorporates feeding of vapor and liquid streams through a stacked foam assembly. The high porosity and highly structured walls of the foam allow a high degree of contacting between the vapor and liquid streams, maximizing mass transfer at both high and low absolute and relative vapor and liquid flow rates.

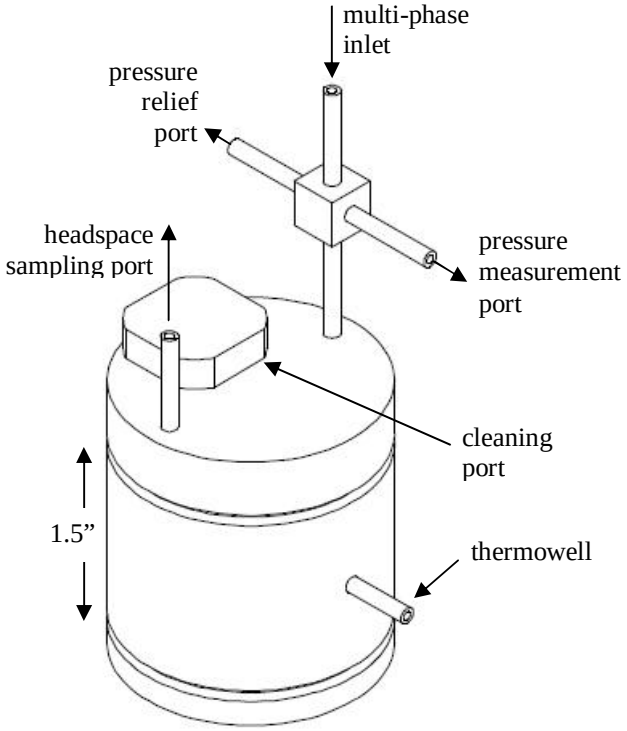

Figure 10. Diagram of the semi-batch collection pressure vessel.

The semi-batch pressure vessel, detailed in Figure 10, allows collection of the fluids following interfacial contacting through the flow through device. The pressure profile monitored during filling of the vessel and measurement of the headspace volume at the end of each run serve as direct indicators of the extent of absorption occurred during contacting. All vessel components shown in the figure match those of the larger batch vessel design (allowing the adoption of the same headspace sampling protocols used for batch experiments). However, the shorter vessel height minimizes liquid consumption and reduces experimental test times, allowing fast pressure response and quick reduction of vapor headspace, for concentration measurement.

As shown in the system schematic of Figure 11, an overflow drum allows collection of vapor and liquid at startup, as the system is primed with the test fluids. Both the flow-through and collection devices are placed in a temperature controlled water bath, to ensure isothermal operation. As configured, the assembly allows test startup at high downstream pressures, to maximize absorption and increase the sensitivity of the semi-batch test.

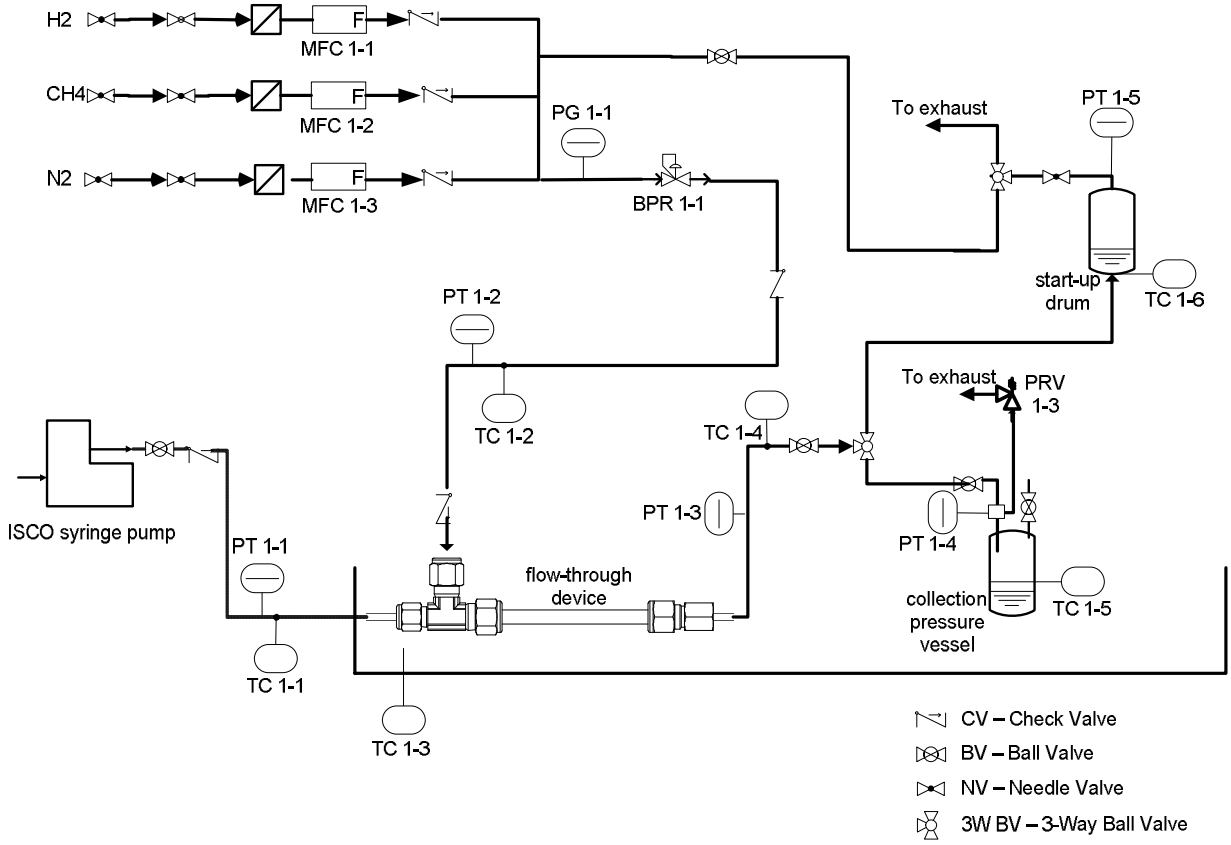

Figure 11. Simplified Piping and Instrumentation Diagram of the semi-batch test stand.

Calculation Methodology

Matlab programs were written to predict the time dependent pressure and headspace concentration profiles in the collection vessel in response to one of the following case conditions:

1. no interaction between the vapor and liquid phases;

2. ideal, instantaneous equilibration of all species and phases in the collection vessel once the fluids exit the contacting device (regardless of interactions in the contacting device);
3. ideal equilibration at the exit of the contacting device in response to the rising pressure in the collection vessel (with no interfacial interaction once the fluids enter the collection vessel).

For simplicity of both test and calculation, the current predictions are constrained to a two-species vapor stream and a pure liquid stream; volumetric vapor and liquid flow rates are held constant. Ideal gas and Henry's laws are assumed to hold for all species (given relatively low extent of dissolution). Liquid density is assumed constant, in spite of species absorption, and the ionic liquid is assumed to be nonvolatile. Given our batch test observations, which showed that liquid mixing is necessary to achieve interfacial interaction in the collection vessel, the experimental premise is that the pressure profile and final concentration in the headspace will reflect Case 3 predictions. In evaluating test results, the absorption parameters of each species (the Henry's constants) will be selected and experimental observations compared against expectations to gauge system and ionic liquid performance.

For Case 3, if/once all the vapor stream is absorbed by the flowing liquid (all gas is absorbed before entering the collection vessel), the headspace composition is assumed to stop changing and the vessel pressure is let rise only in response to compression of the gas already in the vessel headspace. In all cases, assuming *A* and *B* to indicate the vapor species and *C* the ionic liquid,

$\frac{dn_A}{dt}, \frac{dn_B}{dt}, \frac{dn_C}{dt}, \frac{dn_{tot}}{dt}, V_{tot}, \frac{dV_L}{dt}, H_A H_B$ are constant.

Also,

$\frac{dn_i}{dt}$	=	rate of change in moles of species *i* exiting the contacting device / entering the collection vessel
V_{tot}	=	total collection vessel internal volume
$\frac{dV_L}{dt}$	=	rate of change in liquid volume in the collection vessel
$\frac{dn_{liquid}}{dt}$	=	rate of change in molar liquid flow rate exiting the contacting device
$\frac{dn_{gas}}{dt}$	=	rate of change in molar vapor flow rate exiting the contacting device
$\frac{dn_L}{dt}$	=	rate of change in moles of liquid present in the collection vessel
$\frac{dn_G}{dt}$	=	rate of change in moles of vapor present in the collection vessel
y_i, x_i	=	molar fraction of species *i* in the vapor and liquid phases within the collection vessel
$y_{i\ stream}, x_{i\ stream}$	=	molar fraction of species *i* in the vapor and liquid phases of the stream exiting the contacting device/ entering the collection vessel

In the collection vessel:

$$V_{tot} = V_G + V_L \tag{11}$$

Calculations involve specifying initial pressure and vapor concentration in the pressure vessel. The total run time for both simulation and experiments is limited to the time required to fill the collection vessel 19 mm below its rim, to provide the minimum headspace volume required to vapor GC concentration measurement in the experimental system. The predicted pressure and headspace concentration in the collection vessel at the final simulation run time are dictated by the Henry's constant of the species present in the system. At this time, the two vapor species are taken as methane, species *A*, and nitrogen, species *B*.

Case 1:

$\frac{dn_G}{dt} = \frac{dn_{gas}}{dt}$ = constant standard vapor feed flow rate

$\frac{dn_L}{dt} = \frac{dn_{liquid}}{dt}$ = constant liquid feed flow rate

$PV_G = n_G RT$ is differentiated to obtain $\frac{d(PV_G)}{dt} = RT\frac{dn_G}{dt}$ (12)

- Equation 12 is integrated directly to obtain the pressure profile with time (all else being constant).

Case 2:

$\frac{dn_G}{dt} \neq \frac{dn_{gas}}{dt}$

$\frac{dn_L}{dt} \neq \frac{dn_{liquid}}{dt}$

Molar balances and vapor-liquid equilibrium in the collection vessel:

$n_{tot} = n_L + n_G$ (13)

$n_A = x_A n_L + y_A n_G$ (14)

$n_C = x_C n_L$ (15)

$y_A P = x_A H_A$ (16)

$y_B P = x_B H_B$ (17)

$y_A + y_B = 1$ (18)

$x_A + x_B + x_C = 1$ (19)

$PV_G = n_G RT$ (20)

- All equations are simultaneously solved for n_G, the expression is differentiated to obtain $\frac{dn_G}{dt}$, and this is numerically integrated to obtain the instantaneous vapor molar profiles in the collection vessel.

Case 3:

$$\frac{dn_G}{dt} = \frac{dn_{gas}}{dt}$$

$$\frac{dn_L}{dt} = \frac{dn_{liquid}}{dt}$$

Molar balances and vapor-liquid equilibrium in the collection vessel:

$$\frac{dn_{tot}}{dt} = \frac{dn_{liquid}}{dt} + \frac{dn_{gas}}{dt} \quad (21)$$

$$\frac{dn_A}{dt} = x_{A\,stream}\frac{dn_{liquid}}{dt} + y_{A\,stream}\frac{dn_{gas}}{dt} \quad (22)$$

$$\frac{dn_C}{dt} = x_{C\,stream}\frac{dn_{liquid}}{dt} \quad (23)$$

$$y_{A\,stream}P = x_{A\,stream}H_A \quad (24)$$

$$y_{B\,stream}P = x_{B\,stream}H_B \quad (25)$$

$$y_{A\,stream} + y_{B\,stream} = 1 \quad (26)$$

$$x_{A\,stream} + x_{B\,stream} + x_{C\,stream} = 1 \quad (27)$$

$PV_G = n_G RT$, differentiated to obtain $\frac{d(PV_G)}{dt} = RT\frac{dn_G}{dt}$ (28)

- All equations are simultaneously solved to obtain three expressions for the differentials terms $\frac{dn_G}{dt}$, $\frac{dn_L}{dt}$, $\frac{dP}{dt}$ and an expression for the instantaneous quantity of species A in the headspace of the collection vessel, $\frac{dn_G}{dt}y_{A\,stream}$.
- The four expressions are simultaneously integrated numerically with Matlab to obtain instantaneous molar, pressure, and headspace concentration profiles.

Results and Discussion

Our ongoing studies aim to address questions that relate both to current testing capabilities and eventual practical implementation needs. Most data published to date for ionic liquid absorption relate to pure gaseous streams. Many competitive absorption effects are calculated by comparing pure species solubilities in ionic liquids. Such calculations ignore potential complexities of processing real flue gas streams, which involve varying species mixtures. Our studies of species absorption from a mixed vapor headspace into ionic liquid systems are helping shed light on some of these behavioral complexities.

Stream Contaminants

Three candidate ionic liquids, identified as A, B, and C, were selected for absorption testing. All were tested in the batch device. Because of limited ionic liquid availability, only ionic liquid A was adopted for testing in the continuous microchannel flow trials. The most promising of the ionic liquids, ionic liquid B, was used in preliminary semi-batch test evaluations.

In the continuous flow trials, recognizing that moisture in the environment or in the flue gas can absorb readily into ionic liquids during processing and noting that viscosity if ionic liquids can be reduced with water contamination, as shown in Figure 12 for an exemplary ionic liquid, we opted to add 4 wt% water to our ionic liquid A system, an amount that leads to significant reduction in processing energy requirement without posing any safety problems. Preliminary measurements of this water-ionic liquid mixture have shown more than 80% reduction in viscosity relative to the pure ionic liquid.

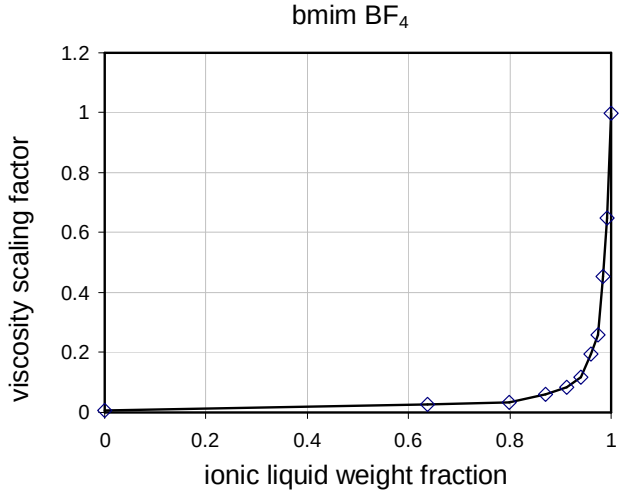

Figure 12. Plot of reported bmim BF_4 ionic liquid viscosity as a function of water content (Tomida et al., 2006).

Batch Test Results

A variety of tests have been performed to date, using both pure and mixed vapor and liquid feeds. Initial tests sequences showed a gradual decrease in gas absorption over time. Recent

tests have led to refinement of the regeneration protocol. Individual measures of methane solubility in the available ionic liquids are listed in Table 1.

The values of Henry's constants for methane absorption in pure A, shown in Table 1, align with available published data. The absorption measurement in the water-modified ionic liquid shows a slight solubility improvement relative to the pure counterpart. Reproducibility of the measurement is required for verification. The low Henry's constants for ionic liquid B show significant absorption and enhanced potential for implementation of processing for the industrial scale. The solubility of methane in ionic liquid C was found to lie between its solubility in ionic liquid A and B.

absorbing liquid code	*ionic liquid batch*	*test description*	H_{CH4} *(bar/mol fraction)*
A	1	fresh	1,124 ± 529
A	1	regenerated	1,232 ± 630
A	1	regenerated	1,741 ± 1,188
A	1	regenerated	922 ± 383
96wt% A : 4wt% water	1	fresh	766 ± 273
B	1	fresh	241 ± 58
B	1	regenerated	217 ± 1
B	2	regenerated	328 ± 15
B	2	regenerated	313 ± 9
C	1	regenerated	597 ± 16
C	1	regenerated	404 ± 5

Table 1. Methane solubility measurements. Ionic liquid batch relates to the time of purchase; this was noted to ensure potential manufacturing differences would not be overlooked.

Continuous Microchannel Flow Test Results

A single flow through test run was completed to preliminarily gauge absorption performance and allow test protocol refinement. Mixing features were incorporated in the channel sidewalls to provide enhancement in interfacial mass transfer. A 96wt% ionic liquid, 4wt% water liquid mixture (whose absorption capacity was previously tested in the batch trials; ionic liquid A) was adopted for methane absorption from a vapor stream containing nitrogen, methane and hydrogen gases. Addition of water to the ionic liquid reduces liquid viscosity, reducing the operating pressure drop. The vapor stream was fed at a constant flow rate; the liquid flow rate was varied to achieve different levels of absorption. Downstream pressure was varied to retain a relatively consistent feed pressure, not to exceed a predefined operational range. Testing was performed at room temperature. Pressure drop was measured for a variety of liquid flow rates. The extent of absorption was measured for two liquid flows. The assumed Henry's constants for each species and the absorption test results are summarized in Table 2. Pressure drop profiles are plotted in Figure 13.

As noted in Figure 13, at the flow rates considered, pressure drop increases linearly with increasing liquid flow rate. This dependence may be indicative of a relatively laminar flow profile, attributable to the very small vapor and liquid flows adopted in these preliminary trials. As tabulated in Table 2, increased liquid flow rates at these operating conditions led to decreased absorption efficiency but increased methane absorption.

bath temperature, °C		20		20	
vapor feed flow rate, sccm		100		100	
liquid feed flow rate, ccm		6		8	
feed pressure, psig		313		309	
knock out drum pressure, psig		246		221	
	assumed H, bar/mol fraction	***measured vapor concentration, mol fraction***			
		feed	***exit***	***feed***	***exit***
N2	20,000	0.030	0.048	0.030	0.034
H2	20,000	0.900	0.899	0.900	0.891
CH4	766	0.080	0.076	0.080	0.074
% of maximum CH4 absorption capacity		42		31	

Table 2. Continuous flow absorption test results.

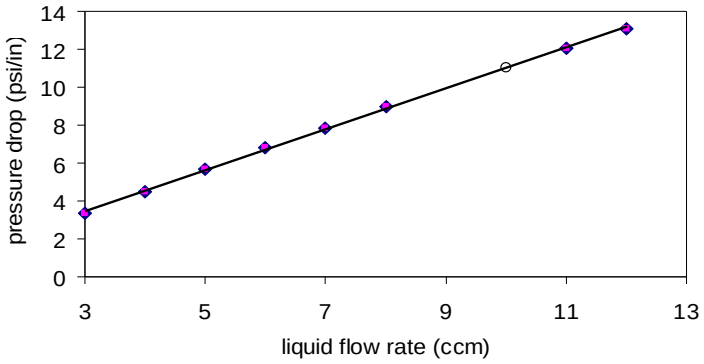

Figure 13. Pressure drop profiles for 100 sccm vapor and varying liquid flow rates.

Semi-Batch Test Results

Gauging Wetting Behavior

Since semi-batch tests involve the use of a stacked foam assembly to facilitate interfacial contacting, contact angle and immersion tests were performed to gauge the interaction of the ionic liquids and de-ionized water with sample stainless steel foams.

De-ionized water, used as a control fluid, demonstrated poor wetting of the stainless steel surface. The contact angle measured on a relatively smooth, flat surface was found to be 66°; the contact angle on the surface of the foam was estimated at 133°. Immersion tests seemed to indicate complete filling of the void spaces with water.

All ionic liquids demonstrated good wetting of the stainless steel surface. The contact angle measured on a relatively smooth, flat surface was found to be 56° for ionic liquid A, 33° for ionic liquid B, and 10° for ionic liquid C. The contact angle on the surface of the stainless steel foam was immeasurable, since all liquids penetrated the surface immediately upon contact. Immersion tests seemed to indicate complete filling of the void spaces with liquid, as well.

The good wetting behavior of the ionic liquids shows promise and potential for enhanced vapor-liquid mass transfer during absorption testing.

Predictive Performance Estimates

Simulated predictions of headspace pressure and compositions were made to gauge the sensitivity of the test to differences in extent of absorption and run conditions. Simulated conditions and results are summarized in Table 3 and Figures 14 and 15 show profiles for representative cases.

Figures 14 and 15 are intended to clarify the impact of the different equilibration scenarios, showing predicted pressure and concentration profiles for representative case conditions. The system was assumed to be pre-pressurized with nitrogen to 100 psig in all cases. As shown in Figure 14, a linear increase in pressure is predicted for vapor only flows. The slope of the profile reflects the vapor fill rate. These curves are serving as guides in ongoing stand functionality tests, in which the headspace pressure profile monitored during filling and the concentration measured at the end of the fill period allow validation of equipment and test stand assembly.

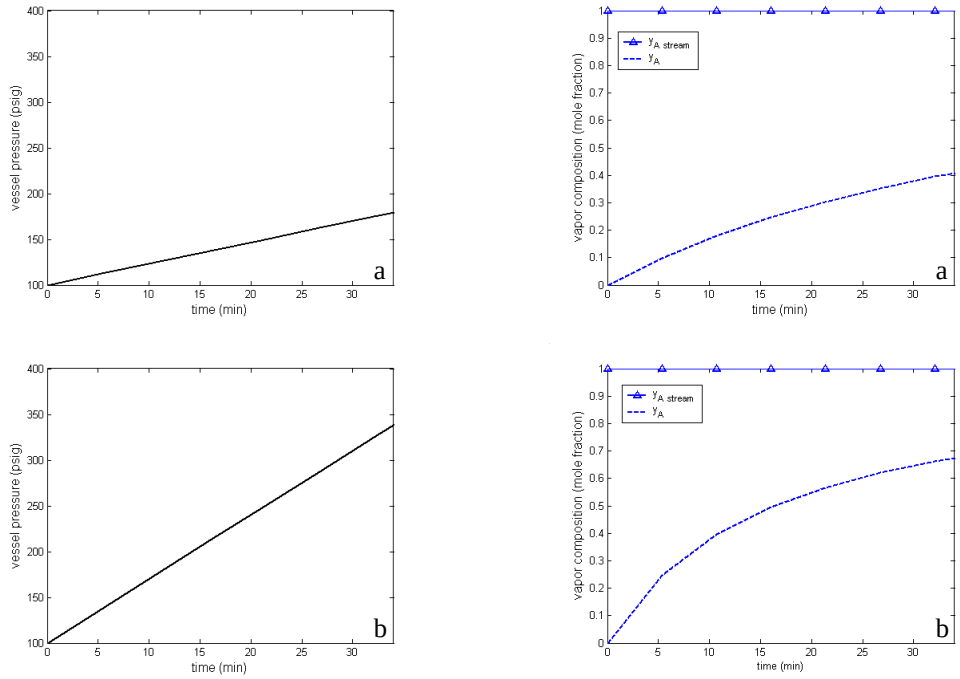

Figure 14. Pressure and concentration profiles for two comparative flow scenarios involving a collection vessel pre-pressurized to 100 psig with nitrogen and an inlet flow of pure methane. a) Profiles in response to a 10 sccm fill rate. b) Profiles in response to a 30 sccm fill rate. Liquid doe not flow in either scenario.

The curves in Figure 15 show the impact of varying equilibration scenarios, as predicted by Matlab simulations. Relatively high pressure is expected to result when no vapor liquid interaction occurs in either the contacting device or collection vessel, and the headspace concentration at a given fill time is expected to be the same as that obtained upon filling the collection vessel with vapor alone (as visible by comparing concentration profiles of Figure 14a and 15a). Figure 15b shows that a slight reduction in pressure and methane headspace concentration would result if instantaneous equilibration of the species in the collection vessel were to occur in the testing; Figures 15a and 15b include molar profiles in the vapor and liquid phases to help discern the distribution of the species in the two scenarios. The lowest pressure and methane headspace concentration is projected for the case in which the flowing streams equilibrate fully in the contacting device, as shown in Figure 15c. The molar fractions of the species at the exit of the contacting device are included in Figure 15c to clarify species distribution.

As shown in Table 3, differing run conditions and solubility values are expected to have a measurable impact on headspace pressure profiles and final methane concentration. Hence, this semi-batch test methodology is expected to provide valuable feedback on process effectiveness and ionic liquid performance with a liquid consumption of only 34 cc. In addition, by varying bath temperature and collection vessel size, the current test protocol might also be adopted for fast ionic liquid regeneration.

	(bar/mole fraction)						*vessel conditions after filling 34 min*	
run #	H_{N2}	H_{CH4}	*simulation case*	*liquid feed flow rate (ccm)*	*vapor feed methane concentration (mol fraction)*	*initial vessel pressure (psig)*	*pressure (psig)*	*headspace methane concentration (mole fraction)*
1			1				381	0.41
2	20,000	240	2	10	1.0	100	341	0.35
3			3				323	0.31
4		100					252	0.13
5	20,000	240	3	10	1.0	100	323	0.31
6		1,000					366	0.39
7		1,600					372	0.40
8		100					215	0.00
9	20,000	240	3	5	1.0	100	250	0.12
10		1,000					288	0.23
11		1,600					293	0.24
12		100					314	0.15
13	20,000	240	3	10	0.7	100	346	0.22
14		1,000					371	0.27
15		1,600					374	0.28
16		240					405	0.20
17	20,000	1,000	3	10	1.0	150	463	0.30
18		1,600					470	0.31

Table 3. Simulated run conditions for semi-batch absorption testing. All cases assume a 1 ccm ionic liquid flow rate and 20°C operation. Simulation case 1 assumes no absorption. Simulation case 2 assumes instantaneous vapor liquid equilibration in the collection vessel. Simulation case 3 assumes vapor liquid equilibrium at the exit of the contacting unit with no further equilibration in the collection vessel. Ionic liquid density and molecular weight are assumed constant and equal to 612.29 g/mol and 1.56 g/cc, respectively. Figure 16 summarizes results for Runs 1, 2, and 3.

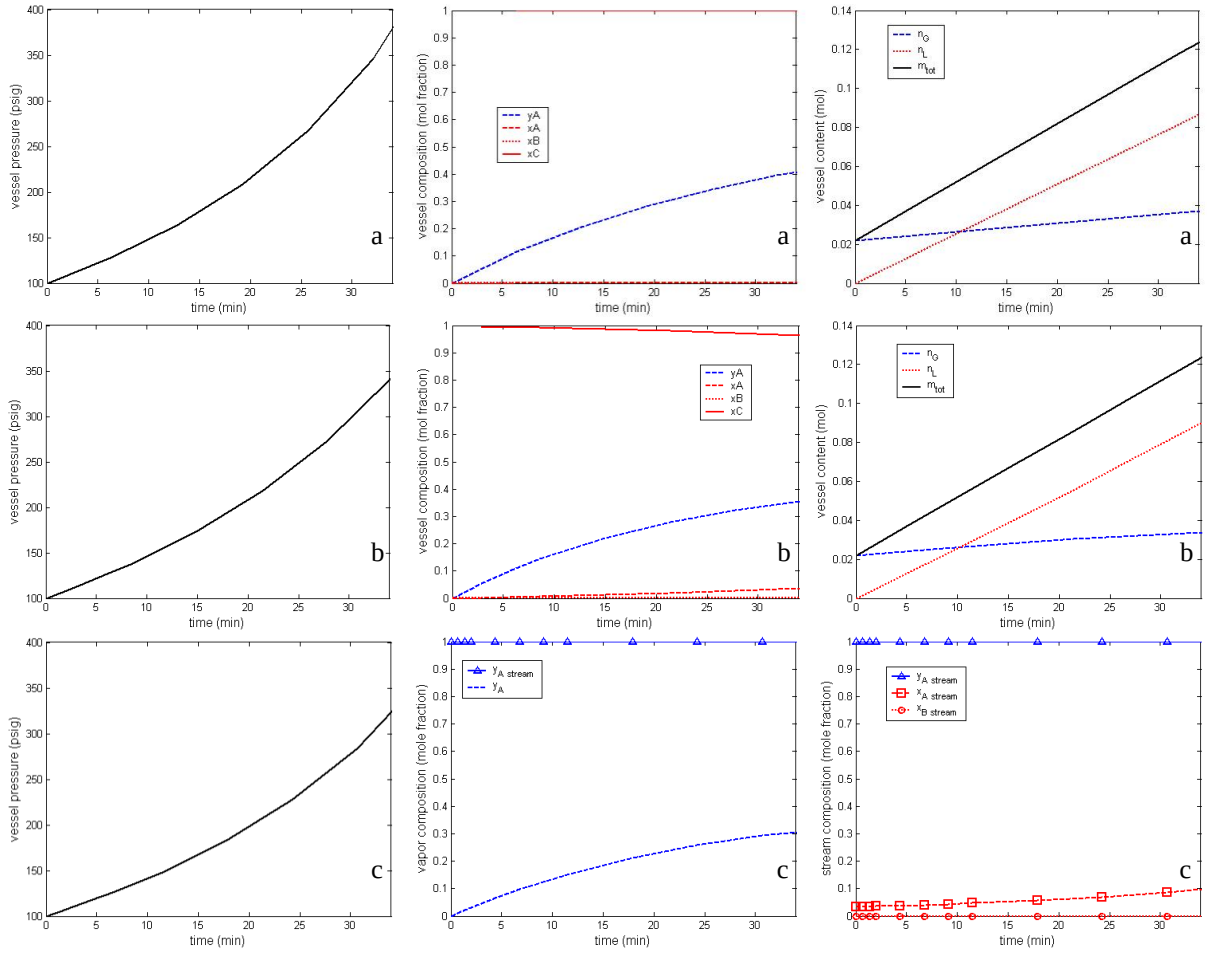

Figure 15. Pressure and concentration profiles for various equilibration scenarios involving a collection vessel pre-pressurized to 100 psig with nitrogen and inlet flows of 10 sccm of pure methane gas and 1 ccm of ionic liquid. Henry's constants are assumed to be 20000 and 240 bar/mol fraction for nitrogen and methane, respectively. a) Liquid and vapor flows with no absorption in the contacting device or collection vessel. b) Liquid and vapor flows with instantaneous ideal equilibration in the collection vessel. c) Liquid and vapor flows with ideal absorption in the contacting device and no re-equilibration in the collection vessel. Figures a, b, and c correspond to Runs 1, 2, and 3 in Table 3, respectively.

Preliminary Experimental Results

Preliminary semi-batch absorption tests adopting ionic liquid B were completed in the shakedown process. Pressure and concentration measurements and estimates are tabulated in Table 4 for the cases considered. Measured data indicate higher than projected absorption using Henry's constants internally determined adopting the batch test stand assembly, suggesting deviation from batch performance by continuous processing. The Henry's law constant for both methane and nitrogen were more than an order of magnitude smaller than suggested by the batch experiments, suggesting that there may be an unquantified experimental error in this system or an overprediction of Henry's law constants in the previous batch mode experiments.

If the simulation parameters were varied to match the experimental observations, complete agreement could result only by assuming extremely low Henry's constants for the vapor species and instantaneous equilibration in all phases upon entering the collection vessel. These parameter values are also noted in Table 4.

	Test 1					***Test 2***				
Liquid flow rate (ccm)	1					1				
Vapor flow rate (sccm)	5					10				
Temperature (°C)	19.6					19.4				
Initial collection vessel pressure (psig)	106.9					103.5				
	experiment	***simulation case***				***experiment***	***simulation case***			
		1	***2***	***3***	***2***		***1***	***2***	***3***	***2***
Assumed H_{N2} (bar/mol fraction)			240		52			240		47
Assumed H_{CH4} (bar/mol fraction)			20,000		70			20,000		75
Final pressure (psig)	186	308	295	260	186	219	380	348	329	219
Final CH_4 in headspace (mol fraction)	0.17	0.25	0.11	0.20	0.17	0.26	0.40	0.35	0.30	0.26

Table 4. Preliminary semi-batch test results and comparative estimates. Feeds were let flow into the collection vessel for 34 min. In all cases, the vapor feed was pure methane and the pre-pressurized collection vessel was filled with pure nitrogen.

Economic Analyses

CHEMCAD was used to simulate eventual absorption/desorption cycles to evaluate the cost benefits of implementing the ionic liquid process.

Executive Summary for System Cost Analysis

An initial system configuration was evaluated based on the reported literature affinity for methane and nitrogen in an ionic liquid. Specifically, by calculating the amount of methane absorbed into the ionic liquid [bmim][PF6] (as cited by Anthony et al., 2002), an advantaged system has been projected.

The Henry's law constant for methane at 10 C of 1480 bar is used along with the minimum Henry's law constant for nitrogen of 20,000 bar. Using an inlet system pressure of 10 bar and a feed gas mixture comprising 80% methane, the liquid mole fraction of methane is 0.016.

For a system with a total gaseous feed flow rate of 2,000,000 standard cubic feed per day and the 80% feed methane composition, then the required flow rate of the ionic liquid discussed is roughly 54,000 L/min at equilibrium to recover roughly 63% of the methane. The reported molecular weight of this ionic liquid is 284 gm/mole. The reported density is roughly 1.37 gm/cc. The volumetric ratio of liquid to gas is roughly 1.4 at the feed inlet. The ratio increases to roughly 7 as the bulk of the methane is absorbed into the ionic liquid. For alternative ionic liquids with more capacity for methane over that reported in this example, then the amount of ionic liquid required would reduce roughly proportionally with the reduction in Henry's law constant.

From the reported maximum Henry's law constant for nitrogen, the minimum purity possible in a single stage is 98.2%. If the actual Henry's law constant for nitrogen is higher than the maximum reported value, then the purity for methane in a single stage may be higher than 98.2%.

Purity is defined by (ymethane/Hmethane)/(ymethane/Hmethane + yN2/HN2) where y is the feed mole fraction and H is the Henry's law constant.

For a thermal swing process, energy must be added to the gas-fluid mixture to desorb the methane and removed from the fluid to absorb the methane. Using an average heat capacity as reported in the literature of 400 J/mol-K (Fredlake et al., 2004) and the reported liquid flow rates then the amount of energy added will be a function of the degree of thermal recuperation, as shown in Table 5.

The absorption process requires heat for methane in the [bmim][PF6] ionic liquid as cited, roughly 2kJ/mol of methane for the cited ionic liquid (Anthony et al., 2002). For this separation and the moles of methane absorbed roughly 47 kW of energy will be required during absorption. Using the heat capacity of the ionic liquid, this roughly equates to less than a 0.03 C temperature loss in the fluid, but this is advantageous as the bulk temperature of this fluid stream is decreasing in the absorption section of the process system. This small increase will result in a

slight increase in the log mean temperature difference for the heat exchanger and result in a slightly smaller requirement for surface area which is advantageous.

dT, approach at each end (°C)	Q-heat (MW)	Q-cool (MW)	Q total (MW)
10	17.3	17.3	34.6
5	8.7	8.7	17.4
2	3.7	3.7	7.4
1	1.7	1.7	3.4
0.5	0.87	0.87	1.74
0.1	0.17	0.17	0.35

Table 5. Energy required as a function of approach temperature to capture 63% of a mixture comprising 80% nitrogen and flowing at 2 million standard cubic feet per day using the [bmim][PF6] ionic liquid and based on highly effective microchannel recuperative heat exchangers.

Analysis considering operational costs

CHEMCAD was used to gauge the sensitivity of methane-nitrogen separation costs to several factors, including system pressure drop, ratio of moles of ionic liquid required to moles of vapor feed, ionic liquid cost, raw vapor feed cost, and hardware absorption cost. These parameters were independently varied in a designed experiment (DOE), holding all other parameters constant (including the high and low temperatures, total vapor feed rate, and product purity).

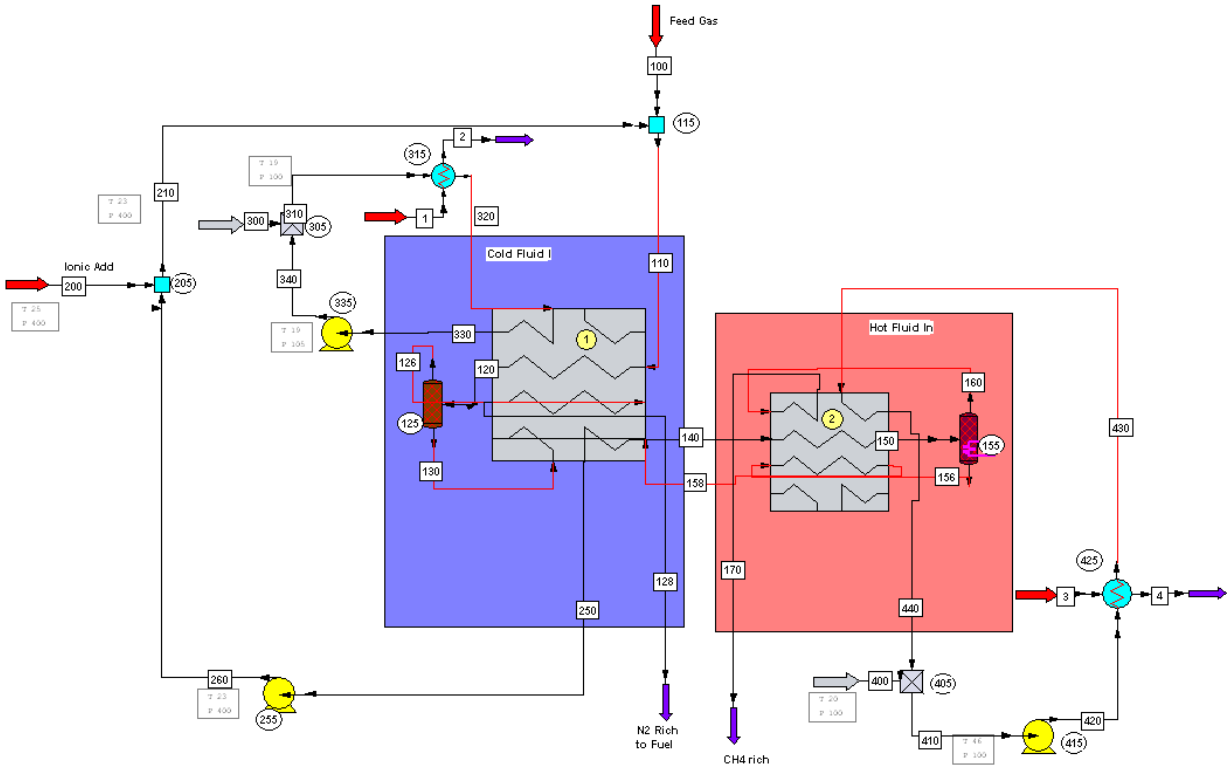

Figure 16. Schematic of the CHEMCAD process cycle used in a designed experiment to discern the impact of operating parameters on separation costs.

A simple curve-fit model was fit to the responses, showing excellent agreement with CHEMCAD/Excel model results. A schematic of the CHEMCAD model is shown in Figure 16. Table 6 summarizes the range of parameter settings considered in the DOE.

DOE Factor	Low Setting	High Setting
pump dP rise (psig)	50	250
mole ratio (IL/gas feed)	3.8	15.2
$/L of IL	10	50
$/1000 SCF gas feed	0	3.4
Hardware cost ($)	250,000	1,000,000

Table 6. CHEMCAD DOE parameter settings.

Figure 17 shows the cost dependence projected by the CHEMCAD model as a function of the parameter settings. In all cases, the dependence is fairly linear. Of the factors studied, the cost of the feed mol ratio has by far the most significant impact on the total cost. The amount of ionic liquid needed to affect the separation follows as the next most significant factor. The pumping power required to deal with the pressure drop is fairly insignificant and thus, the effect of pressure performance (on the moles of ionic liquid needed per mole of feed) becomes the main constraint on allowable pressure drop through the system.

The current analysis has shown that the cost of pipeline natural gas made with the Velocys nitrogen rejection process is most strongly dependent on feed material costs. The amount of ionic liquid required to perform the separation has the greatest impact. The capital cost of the hardware contributes to the total process cost, but to a lesser degree. Pumping costs (independent of separation performance) have a negligible impact over a pressure drop range of 50-250 psi.

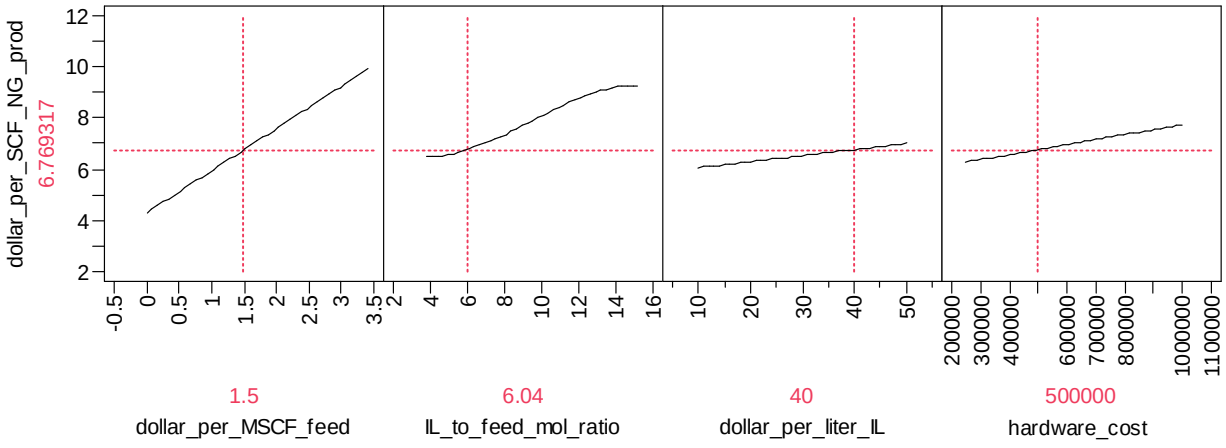

Figure 17. Cost projections made by the CHEMCAD model as a function of the operating parameter settings. The cost per thousand standard cubic feed of pipeline grade natural gas produced assumes $1.50 per thousand standard cubic feet of feed gas, a six to one mole ratio of ionic liquid required per mole of feed, $40 per liter of ionic liquid, and 0.5 million dollars capital cost for the microprocess technology component.

Analysis of required quantities and performance

As noted in CHEMCAD simulation detailed above, ionic liquid costs can be a significant component of process implementation. Hence, another study was performed to quantify the amount of ionic liquid required for a representative separation to gauge the absorption performance required for an economically feasible separation process. This feedback will be used to guide future selection of tailored ionic liquids for this and alternate adsorption processes.

Tailoring Ionic Liquid Absorption and Selectivity

A schematic of the CHEMCAD model used to evaluate the impact of methane solubility on separation performance is shown in Figure 18. A 2,000,000 SCFD low quality, 70 mol% CH_4 / 30 mol% N_2, natural gas stream ("Flue Gas") is upgraded by contacting with an ionic liquid absorbent in sequential cycling through absorption and desorption units, Units 1 and 4, respectively. The ionic liquid utilization (the volumetric flow rate of the "Recycle" stream) and the purity and recovery of methane in the "Product Gas" were calculated in response to varying methane loss to the "Waste Gas". These results are plotted in Figures 19 a and b for two cases. Case 1 assumed a ten fold increase in solubility at the low temperature absorption unit, Case 2 assumed a two fold increase in solubility at the absorption unit relative to solubility at the desorption point.

The ionic liquid properties assumed in these simulations are listed in Table 7. Because ionic liquid properties can be widely tailored, and the most appropriate ionic liquid for the current separation is still being sought, the nitrogen solubility and ionic liquid density and molecular weight were arbitrarily set to match reported values for [bmim][PF6]. Recognizing the need for a high absorption capacity, the adopted high temperature Henry's constant for methane was chosen to be in the range of the best value measured to date, that of the ionic liquid B. The assumption is that improvement can be obtained by ionic liquid tailoring. All simulation values can be changed to refine the study.

Simulated Ionic Liquid Properties		
density (kg/m3)	1.37	
molecular weight (g/mol)	284	
H_{N2} (bar/mol fraction)	20,000	
high temperature H_{CH4}, desorber value (bar/mol fraction)	240	
Simulated Case	**1**	**2**
low temperature H_{CH4}, absorber value (bar/mol fraction)	120	24

Table 7. Ionic liquid properties assumed in simulation Cases 1 and 2.

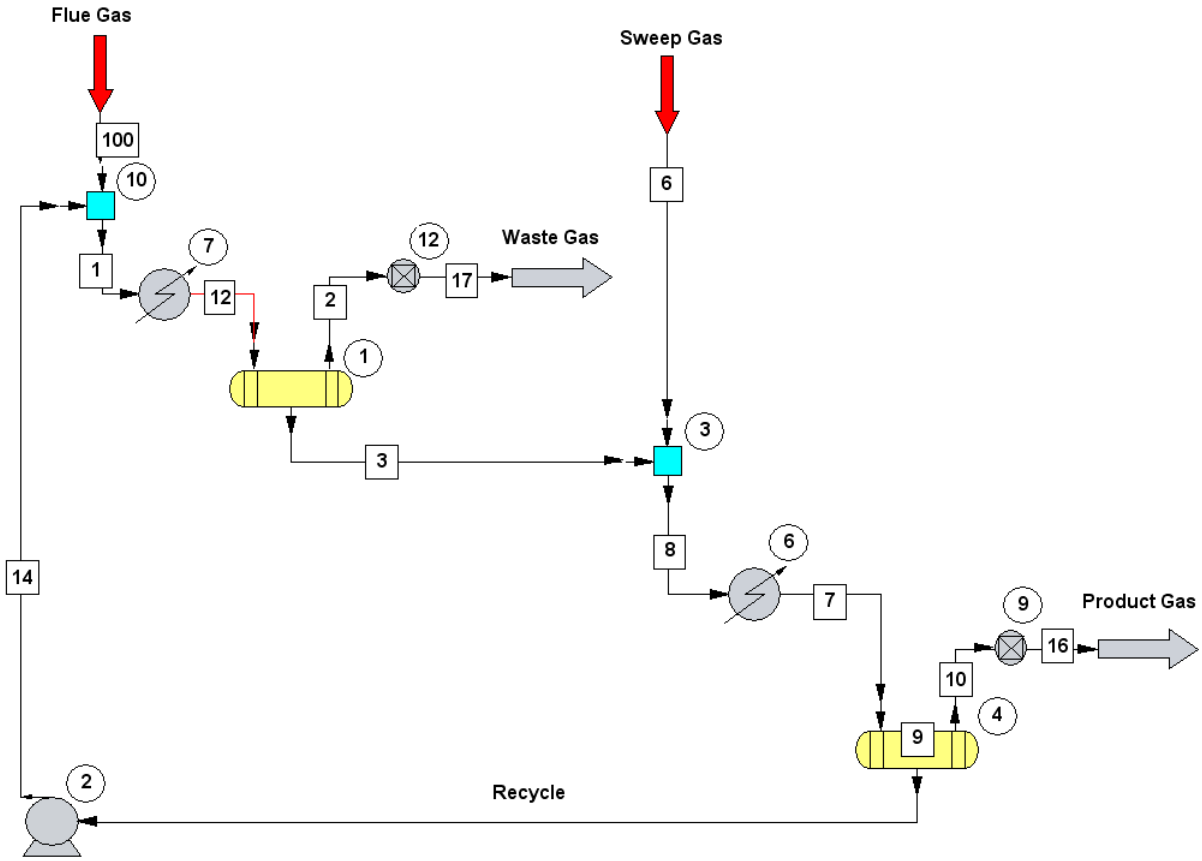

Figure 18. Schematic of the CHEMCAD process cycle used to discern the impact of methane solubility on ionic liquid utilization. Although included in the simulation, the sweep gas stream was assumed to be empty.

It should be noted that the relative magnitudes of the N_2 and CH_4 solubilities, expressed in terms of Henry's constants, have a large impact on the purity of the product gas; larger differences allow greater CH4 selectivity. Also, the absolute value of the CH_4 solubility scales the required ionic liquid volumes; the lower the Henry's constant of the CH_4, the lower the ionic liquid procurement cost. These effects can be inferred, although they were not explicitly studied in this analysis. The current study focused on discerning the impact of the difference between the high temperature and low temperature solubilities.

As can be seen in Figures 19 a and b, a ten-fold decrease in the absorption-side Henry's constant for CH_4 leads to an approximate 50-fold decrease in ionic liquid requirement for a 90mol% CH_4 recovery. CH_4 recovery is defined as a ratio of the moles of CH_4 in the Gaseous Product stream and the moles of CH_4 in the Flue Gas stream. Table 8 summarizes the information graphed in Figure 19 and provides additional details on molar flow ratios and estimated ionic liquid costs.

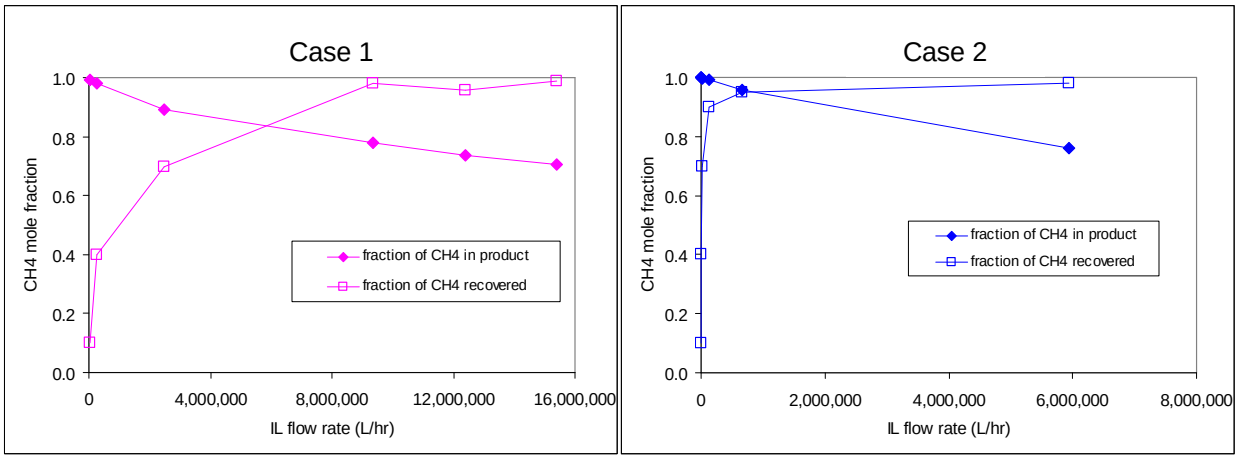

Figures 19 a and b. CH4 recovery and product stream purity as a function of ionic liquid utilization for two representative solubility cases. Both cases assumed a 240 bar/mol fraction H_{CH4} in the desorption unit. Case 1 assumed a 24 bar/mol fraction H_{CH4} at the absorption unit; Case 2 assumed a 120 bar/mol fraction value. Detailed results are presented in Table 6.

To obtain additional insight into the economics of the ionic liquid alternatives, the yearly income associated with the purified product stream was estimated, assuming a $10/MSCF of product stream (stream purity was completely disregarded for this rough calculation) and compared against the one-time cost of the ionic liquid (considering both a $10/L and a $50/L ionic liquid cost). Appreciation of the product price over time was disregarded. As is shown in Figure 20, for the more absorbent ionic liquid, Case 2, the income from the sale of the product stream would pay for the one time cost of a $50/L ionic liquid within 4 months. This corresponds to a of a 99.1 mol% pure CH_4 stream.

As these calculations show, for the right ionic liquid, the separation by the proposed absorption technique offers great promise. It should be noted that the price of the ionic liquid in small batch procurement well exceeds $1000 per liter and as such a goal of $10 or even $50 per liter may well be a stretch goal.

Absorption-Side H_{CH4} = 120 bar/mol fraction					
fraction of CH4 recovered in gaseous product stream (mol fraction)	**IL flow rate in recycle stream (L/hr)**	**IL/Flue Gas flow rate ratio (mol ratio)**	**CH4 concentration in gaseous product stream (mol fraction)**	**IL volume required for a 15 min residence time (L)**	**one-time IL procurement cost, assuming a $10/L price ($)**
0.987	15,400,918	755	0.706	3,850,230	38,502,296
0.959	12,379,395	609	0.736	3,094,849	30,948,487
0.979	9,339,245	461	0.781	2,334,811	23,348,113
0.696	2,494,997	125	0.893	623,749	6,237,493
0.400	274,102	14	0.979	68,526	685,256
0.100	36,586	1.91	0.991	9,147	91,465

Absorption-Side H_{CH4} =24 bar/mol fraction					
fraction of CH4 recovered in gaseous product stream (mol fraction)	**IL flow rate in recycle stream (L/hr)**	**IL/Flue Gas flow rate (mol ratio)**	**CH4 concentration in gaseous product stream (mol fraction)**	**IL volume required for a 15 min residence time (L)**	**one-time IL procurement cost, assuming a $10/L price ($)**
0.981	5,947,500	294	0.759	1,486,875	14,868,750
0.950	660,241	34	0.956	165,060	1,650,603
0.900	122,189	6.78	0.991	30,547	305,473
0.700	21,531	1.58	0.998	5,383	53,827
0.400	5,998	0.58	0.999	1,500	14,995
0.100	1,029	0.12	0.999	257	2,571

Table 8. Key flow rates, composition and results of CHEMCAD simulated Cases 1 and 2.

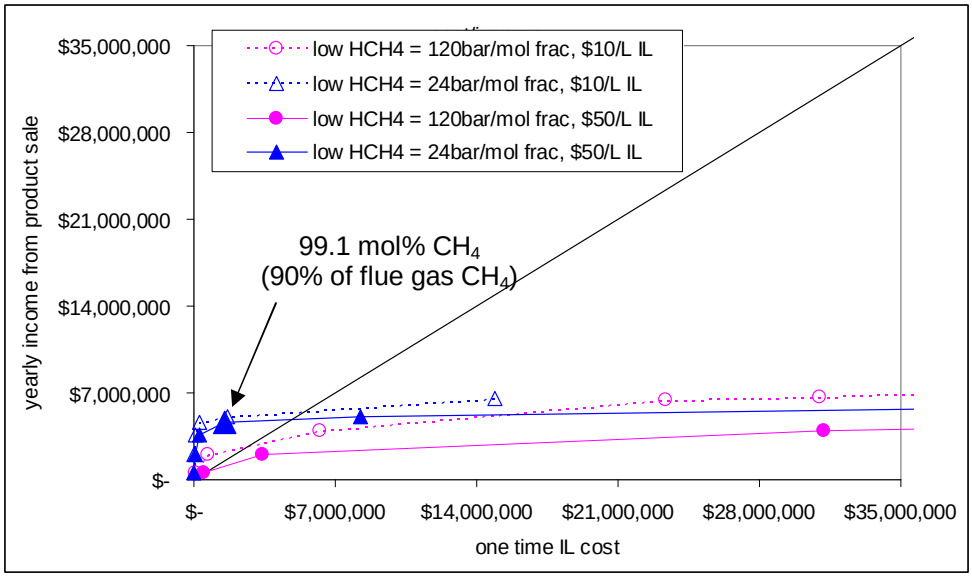

Figure 20. Estimates of yearly potential income from the sale of purified product stream compared against the one-time procurement costs of the ionic liquids considered in the current simulations.

Prospects for Industrial Implementation

As noted in the analyses above, process viability is contingent upon selection of an ionic liquid with appropriate temperature dependent methane solubility. Although current testing has involved only room temperature absorption, some published data can be referenced to discern the temperature dependence of methane solubility in a number of ionic liquids. Representative information is presented in Figure 21 and listed in Table 9.

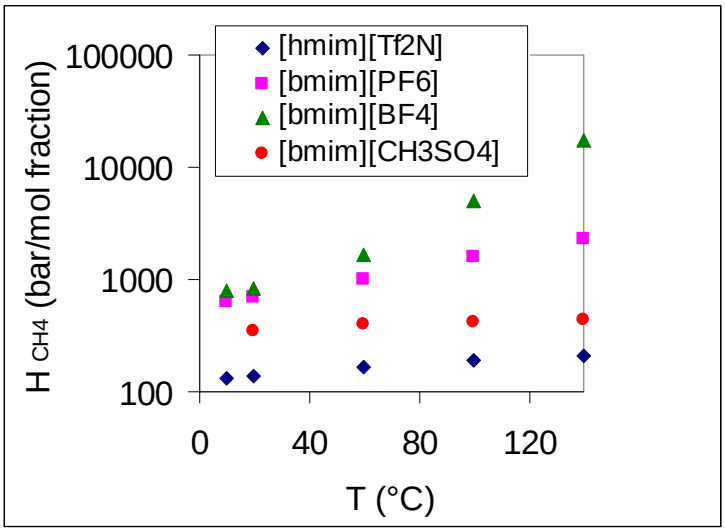

Figure 21. Published temperature dependent methane solubility values for some common ionic liquid alternatives. [hmim][Tf2N] data were taken from Kumelan et al. (2007a), [bmim][PF6] data from Jacquemin et al. (2006a), [bmim][BF4] data from Jacquemin et al. (2006b), [bmim][CH3SO4] data from Kumelan et al. (2007b). Values at 10°C were extrapolated from expressions included in the sources.

temperature	**Henry's constant for methane (bar/mol fraction)**			
(°C)	**[bmim][PF6]**	**[bmim][BF4]**	**[bmim][CH3SO4]**	**[hmim][Tf2N]**
10	640	803		129
20	694	845	344	138
60	1020	1672	391	169
100	1549	4968	423	193
140	2339	17031	442	208

Table 9. Published temperature dependent methane solubility values for some common ionic liquid alternatives. [hmim][Tf2N] data were taken from Kumelan et al. (2007a), [bmim][PF6] data from Jacquemin et al. (2006a), [bmim][BF4] data from Jacquemin et al. (2006b), [bmim][CH3SO4] data from Kumelan et al. (2007b). Values at 10°C were extrapolated from expressions included in the sources.

Although data pertaining specifically to ionic liquid B is not listed, reference to the reported solubility of the off-the-shelf [hmim][Tf2N] confirms confidence in future application of this separation methodology. To more clearly gauge the potential for implementation given current know-how, the model of Figure 19 was re-run adopting the reported solubility (assuming absorption at 10°C and desorption at 140°C, density and molecular weight of the [hmim][Tf2N]. These last two values were assumed to be 1.52 kg/m3 and 447 g/mol, respectively (referencing

the NIST ionic liquid database, http://ilthermo.boulder.nist.gov/ILThermo/pureprp.uix.do). Nitrogen solubility was assumed constant and set to 20,000 bar/mol fraction.

Figures 22 a and b show the methane recovery, product stream purity, and cost comparisons for the simulation. According to these rough estimates and using the same criteria considered in the previous analysis, at an ionic liquid purchase cost of $10/L, the ionic liquid procurement costs would be recovered in approximately 12.4 months of operation.

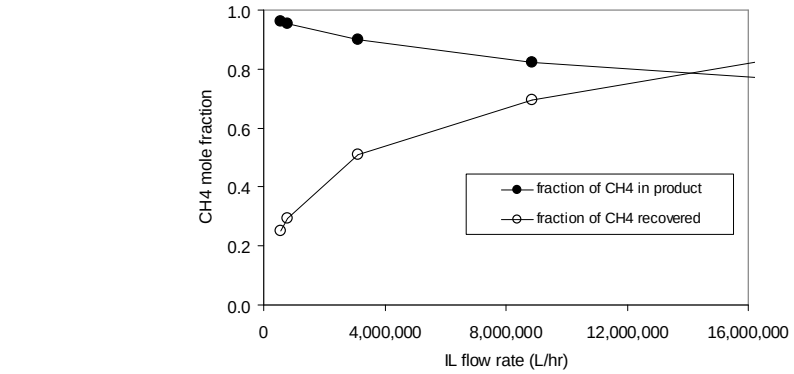

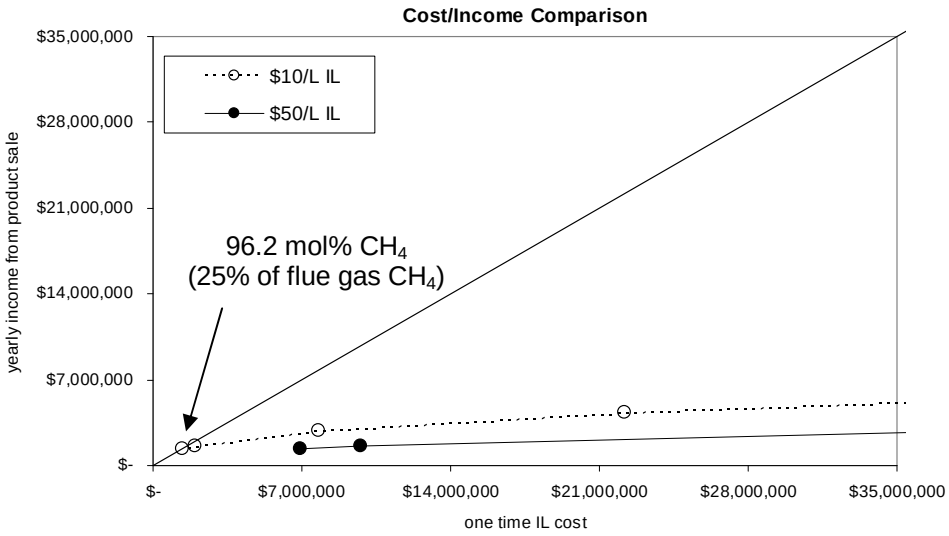

Figure 22 a. CH4 recovery and product stream purity as a function of ionic liquid utilization for a representative case assuming the reported methane Henry's constant of [hmim][Tf2N]: 208 bar/mol fraction in the desorption unit and 129 bar/mol fraction at the absorption unit.
b. Estimates of yearly potential income from the sale of purified product stream compared against the one-time procurement costs of the ionic liquids considered in the current simulation.

In addition, if all parameters were held constant and the absorption-side Henry's constant for methane were reduced by only 72%, to 36 bar/mol fraction, further analysis revealed that it would be possible to recover 90% of the methane in the same flue gas stream at a 96.6% purity level and recover the one-time ionic liquid procurement cost in 4.6 months of operation, assuming an ionic liquid cost of $10/L, or in 23 months of operation for an ionic liquid cost of $50/L.

Given the ability to tailor ionic liquid properties and modify absorption capacity and specificity of these materials, there is great promise for finding an ionic liquid suited to the current process, making this mode of separation an economically viable alternative for methane recovery from process flue streams.

Benefits

The current work has demonstrated the use of ionic liquids for capturing methane in an absorption rather than adsorption mode adopting the Velocys microchannel technology.

Developed microchannel systems have demonstrated significant reduction in the amount of energy required, as compared to the old thermal swing adsorption system (recuperating energy using the ionic liquid).

Economic analyses have shown that the use of an ionic liquid for absorption in a microchannel is dominated by the cost of the ionic liquid. Potential implementation for this application is contingent upon being able to find an ionic liquid with improved methane solubility and a price of less than $50/L. Current prices of ionic liquids at small production levels exceed $1000/L. Lower priced ionic liquids will open the door to this application area. Given the ability to tailor ionic liquid properties and modify absorption capacity and specificity of these materials, potential for eventual implementation exists.

Conclusions

Ongoing work since the beginning of 2007 has led to the adoption of a new class of materials, ionic liquids, for the preferential absorption and separation of methane from a flue gas stream. Samples of ionic liquids with reported affinity for methane were chosen for testing and their performance was evaluated adopting specifically designed batch and microchannel flow through experimental systems.

Economic analyses and experimental testing have shown promise for the implementation of tailored ionic liquids for industrial separations. Preliminary experimental flow tests have shown potential for approaching maximum absorption capacity adopting microchannel devices that allow enhanced interfacial contacting. Economic analyses have demonstrated that ionic liquid procurement is the most significant contributor to process cost and that, adopting a readily available, off-the-shelf ionic liquid and a single pass continuous flow process, it is possible to capture 25% of the methane from a 2,000,000 SCFD low quality, 70 mol% CH4 / 30 mol% N2, natural gas stream to obtain a 96% pure methane product stream and recover the one-time ionic liquid procurement cost in 12.4 months. In addition, for only a 72% reduction in the absorption-side Henry's constant for methane relative to this off-the shelf ionic liquid, further analysis revealed potential for a 90% methane recovery from the flue gas stream at a 96.6% purity level for a 4.6 month break even point, assuming an ionic liquid cost of $10/L, and a 23 month break even point for an ionic liquid cost of $50/L.

Given the ability to tailor ionic liquid properties and modify absorption capacity and specificity of these materials, there is great promise for finding an ionic liquid suited to the current process, making this mode of separation an economically viable alternative for methane recovery from process flue streams.

References

Anthony, J.L., Maginn, J.M., Brennecke, J.F., "Solubilities and Thermodynamic Properties of Gases in the Ionic Liquid 1-n-Butyl-3-methylimidazolium Hexafluorophosphate," J. Phys. Chem. B., **106**(29), 7315-7320, 2002.

Fredlake, C.P., Crosthwaite, J.M., Hert, D.G., Aki, S.V.K., Brennecke, J.F., "Thermophysical Properties of Imidazolium-Based Ionic Liquids," J. Chem. Eng. Data, **49**, 954-964, 2004.

Jacquemin, J., Gomes, M.F.C., Husson, P., Majer, V., "Solubility of carbon dioxide ethane methane oxygen nitrogen hydrogen argon and carbon monoxide in 1-butyl-3-methylimidazolium tetrafluoroborate between temperatures 283," J. Chem. Thermodynamics, **38**, 490–502, 2006.

Jacquemin, J., Husson, P., Majer, V., Gomes, M.F.C., "Low-pressure solubilities and thermodynamics of solvation of eight gases in 1-butyl-3-methylimidazolium hexafluorophosphate," Fluid Phase Equilibria, **240**, 87–95, 2006.

Kumelan, J., Kamps, A.P.S., Tuma, D., Maurer, G., "Solubility of the Single Gases Methane and Xenon in the Ionic Liquid [hmim][Tf2N]," Ind. Eng. Chem. Res., **46**, 8236-8240, 2007.

Kumelan, J., Kamps, A.P.S., Urukova, I., Tuma, D., Maurer, G., "Solubility of the Single Gases Methane and Xenon in the Ionic Liquid [bmim][CH3SO4]," Journal of Chemical and Engineering Data, A-F, 2007.

Tomida, D., Kumagai, A., Qiao, K., Yokoyama, C., "Viscosity of bmimPF6 and bmimBF4 at High Pressure," International Journal of Thermophysics, **27**(1), 39-47, 2006.

List of Acronyms and Abbreviations

Btu	British thermal unit
GC	gas chromatograph
GHG	greenhouse gas
gm	gram
GWP	global warming potential
H_i	Henry's constant for species *i*
HPBV	high-performance butterfly valve
kg	kilogram
$\dot{L}$	total liquid molar flow rate
$\dot{m}_i$	molar flow rate of species *i* through the continuous flow system
mg	milligram
MSCF	thousand standard cubic feet
MMSCFD	million standard cubic feet per day
MW	megawatts
NRU	nitrogen rejection unit
P	total pressure
psig	pound per square inch gauge
$\dot{Q}$	total molar flow rate through the continuous flow system
SLPM	standard liters per minute
TSA	thermal swing adsorption
$\dot{V}$	total vapor molar flow rate
x_i	liquid mole fraction of species *i*
y_i	vapor mole fraction of species *i*
ξ_i	effectiveness of the experimental absorption run for species *i*